Elucidating the Role of Cysteine-Rich Proteins in the Byssal Thread's Cuticle

Omar Gianni Jimenez Castaneda

Department of Chemical Engineering | McGill University, Montreal

July 2024

A thesis submitted to McGill University in partial fulfillment of the requirements of the degree of
Master of Science

Abstract

Biological materials take advantage of diverse chemistries in their biopolymeric building blocks to achieve marvellous properties like self-healing, complex hierarchical structures, and multifunctionality. Byssal threads built by marine mussels are coated by a cuticle, whose protein building blocks are stored in dense liquid-liquid phase separated vesicles. During the thread formation process, these vesicles coalesce and mature into a solid-state cross-linked network coordinated with iron ions that displays outstanding mechanical performance and chemically reducing properties. A new family of cuticle-derived cysteine-rich proteins was recently identified, but their function and role in the material is unknown. In this work, these cysteine-rich proteins were recombinantly expressed in *E. coli* and characterized. The isolated protein building blocks can evolve into a solid-state material at neutral pH from dense liquid storage in acidic conditions. The cysteine-rich proteinaceous material demonstrates strong chemically reducing properties, as well as evident signatures of bioinorganic iron ion coordination bond formation. These findings suggest that these cysteine-rich proteins are necessary for the cuticle's function, and possibly demonstrate a novel type of iron-binding protein with structural roles.

Sommaire

Les matériaux biologiques sont constitués d'éléments biopolymériques avec diverses compositions chimiques. Celles-ci leur permettent d'obtenir des propriétés merveilleuses telles que l'auto-guérison, des structures hiérarchiques complexes et la multifonctionnalité. Les fils du byssus construits par les moules marines sont recouverts d'une cuticule dont les éléments constitutifs protéiques sont stockés dans des vésicules séparées par une phase liquide-liquide dense. Au cours du processus de formation des fils, ces vésicules fusionnent et mûrissent en un réseau réticulé à l'état solide coordonné avec des ions de fer, affichant des performances mécaniques et des propriétés chimiques réductrices exceptionnelles. Une nouvelle famille de protéines riches en cystéine dérivées des cuticules a été récemment identifiée, mais leur fonction et leur rôle dans le matériau sont inconnus. Dans ce travail, ces protéines riches en cystéine ont été exprimées de manière recombinante dans *E. coli* et caractérisées. Les éléments constitutifs protéiques isolés sont capables d'évoluer vers un matériau solide à pH neutre à partir d'un stockage

liquide dense dans des conditions acides. Le matériau protéique riche en cystéine présente une forte capacité de réduction, ainsi que des motifs spectroscopiques clairs de formation de liaisons de coordination d'ions de fer bio-inorganique. Ces résultats suggèrent que ces protéines riches en cystéine sont nécessaires au fonctionnement des cuticules. Ils démontrent aussi peut-être un nouveau type de protéine liant le fer ayant des rôles structurels.

Acknowledgements

"A problem worthy of attack proves its worth by fighting back." - Piet Hein

First and foremost, I would like to thank marine mussels for being the extraordinary yet humble organisms who I, like others who have and others who will, toiled to reveal and understand fragments of their remarkable and mysterious secrets.

I am filled with gratitude to my supervisors Dr. Noémie-Manuelle Dorval Courchesne and Dr. Matthew J. Harrington who provided me the opportunity to contribute to such an exciting project in an exceptionally supportive and collaborative environment, and who always supported me with ideas and motivation to push further when I faced a challenge. I reflect fondly on the trust they placed on me to lead my scientific endeavours with creative freedom. I will never forget the technical lessons and scientific proficiency they bestowed upon me and feel honored to have had the opportunity to be their student.

I must also give thanks to the lab members of the Dorval and Harrington group over the past couple of years who always provided me indispensable feedback, taught me how to use instruments, and who made my laboratory work so enjoyable. I must give my gratitude to Samantha Jee and Dr. Hamideh Rezvani Alanagh in the Harrington group, who assisted me in measuring and analyzing XPS measurements, and exploring protein coacervates, respectively. I also must thank Nahid Hassanpour who helped me perform SFA measurements at UdeM.

Lastly, I am incredibly thankful to my soulmate, Anelya, who joined alongside me through this journey and motivates me every day to excel and be the best person I can be. I am also thankful to my parents and sister for their support, and to my brother Karanjit, who always has my back.

Contributions of Authors

Omar Jimenez performed the experimental work, data analysis, and writing of the work herein, with the exceptions mentioned above. Dr. Noémie-Manuelle Dorval Courchesne and Dr. Matthew J. Harrington provided guidance in all aspects of the project and reviewed the presented work.

Table of Contents

List of Figures

1. Introduction

As we continue to evolve as a technology-driven society, increasing focus is being placed on how we can continue to develop novel ways to achieve new technology, or further improve the functionality of our technology. Arguably, the fundamentals to our ability to carry this out lies in the materials that we have available, and more importantly, if and how much we understand them. This is evident even in the way we have organized our history, where access to novel materials goes on to revolutionize and define the age period, like the stone to metal age transition that was brought on by new metallic materials produced by smelting ore in new furnace technology that could reach higher temperatures than ever before [1]. Ancient civilizations who developed metallurgical techniques to alloy tin and copper were able to produce bronze, a metallic material that was stronger and more durable than other contemporary metals [2]. Buildings became sturdier, weapons more powerful, and jewelry more durable. In more recent times, the development of plastic polymers and semiconductor materials too has revolutionized modern technology and human lifestyle in an exceedingly quick manner that practically define the current era [3-5]. These materials delivered marvellous technological breakthroughs; however, they have also created massive environmental burdens that we must contend with. So, where do we continue from here?

Humans must push for a future that transitions towards materials that can at least replace current options, and more importantly be sustainable and renewable. Perhaps the most feasible way to accomplish this is by examining nature's materials where we will find perfect examples of highly functional materials that are integrated into the planet's balanced ecosystem. More so, we try to understand the living systems that over hundreds of millions of years have evolved clever ways to design and build biological materials with unmatched performance and sustainable production, while being fully integrated into nature's circular economy. A classic example is spider's silk, whose mechanical performance in terms of mechanical toughness remains to be beat by human synthetic fibers [6]. What is more, spiders build their silk on-demand under ambient conditions and is naturally recycled at the end of its lifecycle [7]. Another example, which will be the focus of this work, are the byssal threads that marine mussels build to attach to hard surfaces at the rocky seashore [8]. Byssus threads demonstrate material properties that remain quite difficult to replicate and produce in man-made materials [9]. If we reach an absolute understanding of byssal thread structure, function, and formation, we may gain the capability to sustainably engineer self-healing

fibers, hard and extensible coatings, and underwater adhesives. Eventually, we could rely on bioengineered cell factories to further mass-produce the analogous raw materials that marine mussels make for their threads via recombinant protein expression and replace resource-intensive synthetic chemical production [10].

Nature's material design and production principles are the inspiration that will be of the utmost importance in guiding the development of novel human-made materials that are compatible with a growing population and an increasingly unstable environment [11, 12]. The challenge remains that these materials involve complex biopolymer building blocks, and highly orchestrated manufacturing and assembly processing steps, that altogether are necessary for the material's performance. For this reason, investigation seeking to explore and elucidate nature's materials and schematics is of utmost importance.

2. Literature Review

2.1 Marine Mussels and Byssal Threads

Marine mussels *(Mytilus spp.)* are one of the model species at the forefront of bioinspired material processing and design. These animals are experts in constructing holdfast structures called byssal threads that function to securely anchor them onto solid surfaces while dissipating mechanical stress from crashing waves and predators [13]. Byssal threads have three components: a fibrous load-bearing core, a granular abrasion-resistant cuticle, and an underwater adhesive plaque that work cohesively to tether the mussel onto a surface [14]. These holdfasts are remarkable for being nearly entirely composed of protein building blocks [13] that work together to achieve highly sought-after material properties like rapid bottom-up self-assembly, self-healing, underwater adhesion, and coinciding high levels of hardness and extensibility [8, 13, 15, 16]. Indeed, the mussel byssus is a bioinspiration model that presents the opportunity to understand the concepts necessary to eventually achieve such performance in synthetic materials, and more ideally to perhaps one day biosynthesize the same building blocks via biotechnology [10]. In fact, much work has already been focused on engineering materials that take advantage of the chemical and physical design principles learned from the byssus [14, 17], but the materials remain limited by an incomplete understanding of the elusive fabrication and assembly process executed by the mussel [13].

2.2 Mussel Byssus Production and Assembly

The mussel foot is a specialized secretory organ that is responsible for synthesizing, stockpiling and secreting the protein precursors that will eventually be processed into a thread. The mussel foot evolved ingenious and effective methods to ensure that these raw materials can be easily stored and transported when called upon for thread assembly and is where segregated gland tissues produce and accumulate the protein stocks that eventually assemble into the three principle parts of the thread (i.e., the core, cuticle, and plaque) [18]. Electron microscopy and histological staining was effective in discerning mussel foot tissue that displayed different kinds of dense proteinaceous vesicles, leading to an early classification of a 'collagen' gland, a 'phenol' gland, and an 'enzyme gland' based on vesicle morphology and histological properties [19, 20]. We now know that these glands are responsible for producing the protein vesicles for each thread component. The collagen, phenol, and enzyme gland produce the building blocks that will build the thread's core, plaque, and cuticle, respectively[13]. More recently, these glands have been renamed the core, plaque and cuticle secretory glands to better represent their actual role ([13]). Descriptions of these glands explain how they store these vesicles en masse, and use dedicated channels to scurry them towards the mussel foot's ventral groove and distal depression, where thread assembly occurs [18, 21]. During the fabrication of a new thread, the glands secrete and transport the condensed fluid protein contents of the vesicles from each gland towards the groove (core and cuticle) or distal depression (plaque) via ciliated secretion channels that run along its length [18, 22]. Once emitted, the fluid contents of the vesicles coalesce into larger organized structures; core vesicles form a semi-crystalline fiber, plaque vesicles transition into a porous glue, and cuticle vesicles come together to coat the surface of the entire thread [13]. This process is visualized in Fig.1, with similarities to an injection moulding manufacturing process.

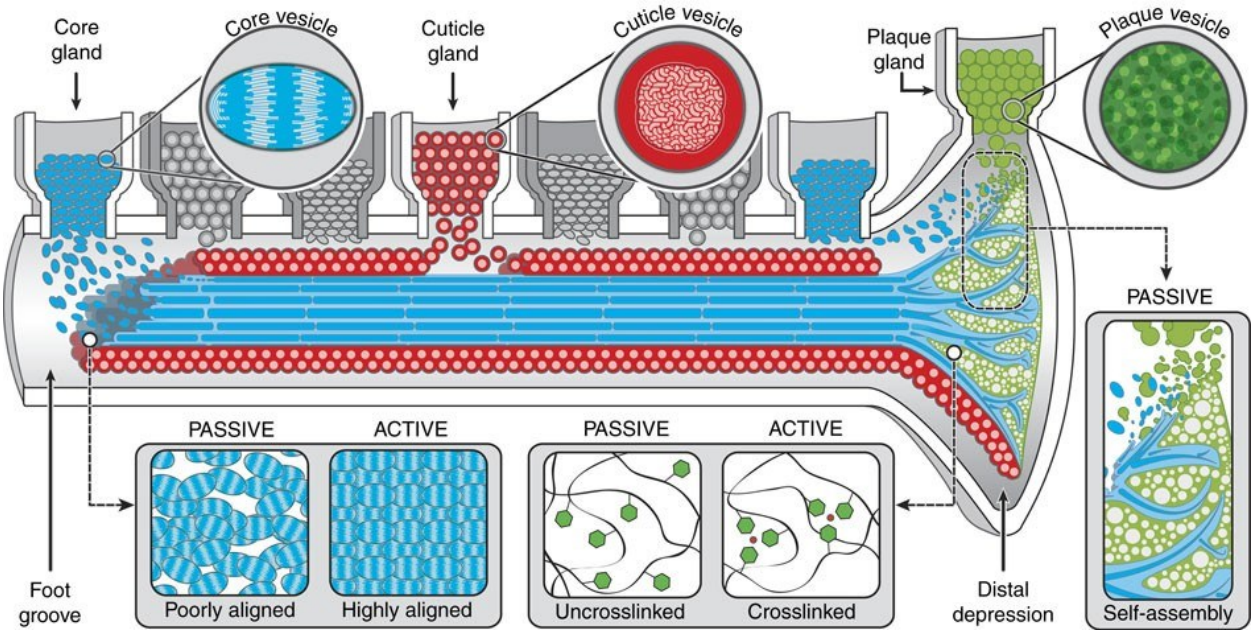

Figure 1. Schematic of byssus assembly in the mussel foot by mobilized protein vesicles secreted from respective mussel foot glands towards the ventral groove, where vesicles coalesce to form the byssal thread structures, resembling an injection mold process. Core vesicles form a highly aligned fiber that is coated by coalescing cuticle vesicles and anchored to a surface by the porous glue formed by plaque vesicles. From [13].

How these vesicles transition from a dense liquid state into a functional thread relies on intrinsic properties of the vesicle proteins, as well as processing factors outside of the vesicles ([13]). Vesicles begin forming structures found in mature threads while stored *in vivo*, demonstrating that the protein building blocks already possess the requirements to self-organize at this early stage. This is clearly observed in core vesicles that house the collagenous precursor proteins (preCols) as a pre-arrangement of the proteins in a smectic liquid crystal form *in vivo* [23]. It is thought that this method of organized storage facilitates the transition into a semi-crystalline fiber, as the preCols already would be aligned in a favourable position akin to a mature core [24]. In a similar manner, cuticle vesicles also exhibit a morphology that is nearly identical to the mature cuticle lining the thread's surface. Likely due to liquid-liquid phase separation (LLPS) of the different proteins within the cuticle vesicles, the vesicles appear to consist of two immiscible fluid phases in a way that looks like the cuticle granule is embedded within a matrix [25]. This morphology is conserved and clearly visible in a mature thread cuticle [16, 26]. Plaque vesicles too demonstrate an ability to behave in a manner that mimics a mature plaque. They demonstrate an innate ability to transition through LLPS into porous 'micro-plaques' *in vitro* that closely resemble the foam-

like structure of a mature plaque [27]. The protein building blocks within these vesicles possess the inherent ability to self-organize in a way that facilitates the transition from a dense concentrated fluid phase towards a functional solid thread material. Yet as mentioned earlier, mussels also must tightly control how they process the vesicles in terms of both the physical and chemical changes that the proteins experience. Indeed, there is evidence that the quality of a byssal thread built in a controlled manner cannot be achieved based on relying on the inherent properties of the vesicles alone without adequate processing [13, 24]. Both physical and chemical factors must be controlled. For example, physical shear forces stemming from mussel foot movement essentially rolls the vesicles into a thread core with enhanced fiber alignment [13, 24]. Control of pH is another crucial variable to the assembly of the byssus thread. Gland tissues store the protein vesicles under acidic conditions, which also remain meanwhile threads are assembling in the foot's groove as the vesicles merge [28, 29]. Indeed, the transition from acidic pH towards slightly basic pH in seawater conditions induces drastic changes that really deserves to be discussed in greater detail in its own section. In particular, we will explore key role of pH-induced formation of metal coordination cross-links that contribute to solidification and enhance mechanical performance. In parallel, managing redox conditions in thread assembly and maturation heavily influences how the byssal protein building blocks and their functional groups will bind and thus, how they would function, especially given the elevated content of redox sensitive amino acids (e.g., DOPA) [15, 30-32].

2.3 The Mussel Byssus Cuticle

Similar to how electric cables have layers of plastic coatings to protect the vulnerable metal cores from environmental degradation, the byssal thread's cuticle plays an important role in covering the entire thread's surface and protecting it from degradation ([26]). The hard polymer coating of an electric cable will succeed in protecting it from abrasion but will fail early if stretched. This is the price that must be paid in today's commercial polymer materials, trading off hardness for extensibility [33]. It does not have to be this way, however, as the byssal thread's cuticle displays hardness values close to hard plastics alongside the capability to endure impressive strains that easily surpass 50% and up to 120% [26, 33]. Such performance easily outcompetes synthetically made coating materials, and it is an impetus that guides investigation to precisely understand how this feat is possible.

The cuticle demonstrates an interesting biphasic morphology with what appears to be granule-like inclusions embedded into a cohesive matrix (Fig. 2) [26, 33]. Interestingly, not all mussel species evolved this intricacy, as subtidal species that do not have to endure the high-energy cyclical forces of crashing waves do not display cuticle granules, and undergo tensile failure at much lower strain levels than a granular cuticle from intertidal mussel species [26]. Studies indicate that the granule's function appears to be directing how failure cracks begin and dissipate. Through the granules, the cuticle directs tensile forces towards forming microtears in the matrix surrounding the granules, controlling and distributing failure across a larger volume within the matrix through formation of multiple failure sites and preventing their merger into larger macro cracks (Fig. 3) [26, 34]. Interestingly, mussel species with smaller, more uniform granule sizes can endure more strain before developing signs of cuticle tear due to a better ability to hinder crack propagation, possibly from a larger granule-matrix interfacial area [34]. As such, the granules in the cuticle act as a buffer against failure, endowing the cuticle a capability to endure more than double the strain than a cuticle without granules [26].

How could we engineer materials to mimic the cuticle's performance? The answer to this question begins by unraveling the structure-function-formation relationships and design principles that give rise to such high performance. Although the entire recipe of the proteins that constitute the cuticle is not complete, significant progress has been achieved in characterizing mussel foot protein-1 (Mfp-1), its major component by far.

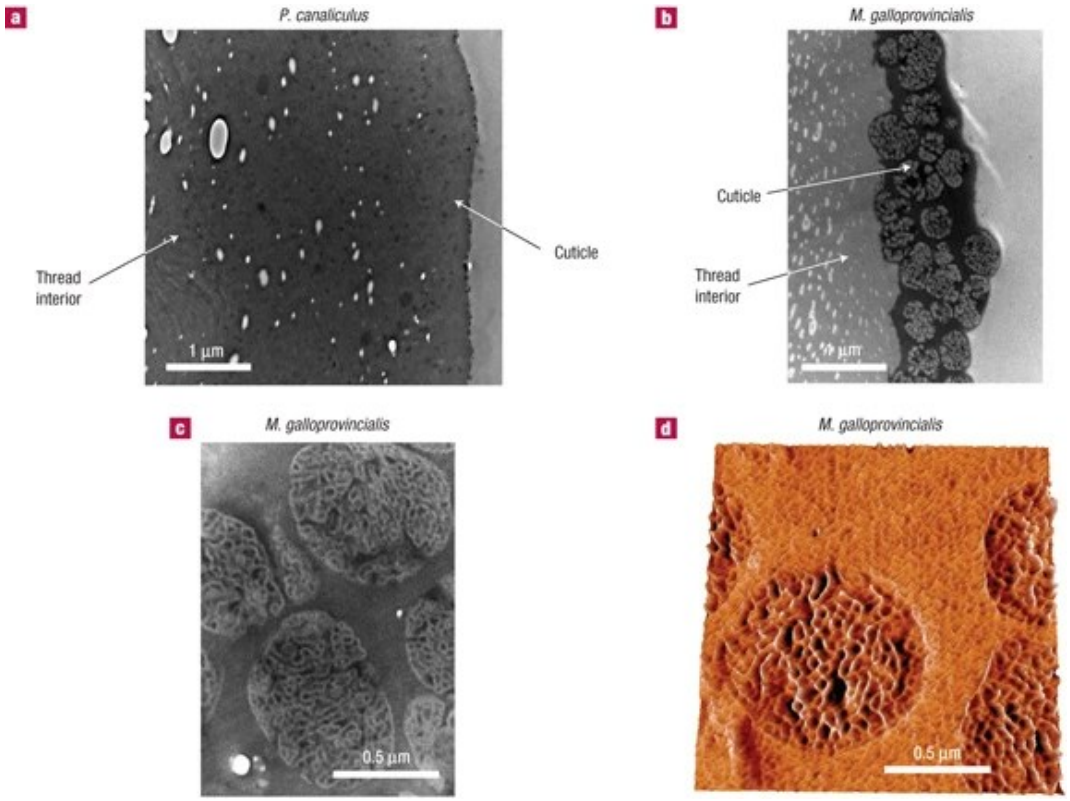

Figure 2. Transmission electron micrographs (a-c) and atomic force microscopy image (AFM) (d) of transverse cross-sections of cuticle derived from subtidal (P. canaliculus) and intertidal (M. galloprovincialis) mussel species shows the formation of cuticle granules in intertidal mussel species. From [26]. a,b) Scale bar: 1 µm. c,d) Scale bar: 0.5 µm.

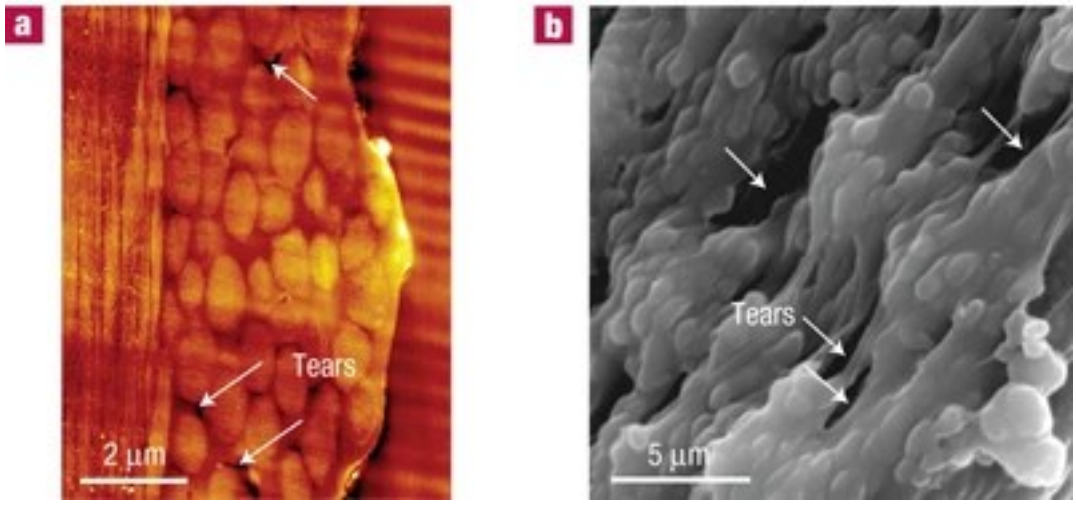

Figure 3. a) AFM image of M. galloprovincialis thread stretched by 50%, showing early stages of microtearing and deformation of granules. b) Corresponding scanning electron microscopy image of cuticle surface at 70% strain, showing extensive microtearing of matrix between granules immediately preceding cuticle rupture. From [26]

2.3.1 Mfp-1 – The Primary Cuticle Building Block

Mfp-1 (mussel foot protein-1) was the first protein to be identified in the byssus cuticle, first termed as the polyphenolic protein [35]. A prevalent pattern of post-translational modifications involving the hydroxylation of tyrosine into L-3,4-dihydroxyphenylalanine (DOPA) was discovered early on [35]. Mfp-1's sequence was found to be composed of tandem repeats of hexa- and decapeptides: AKPTYK, and AKPSYP*P*TY*K, where P* and Y* signify post-translational amino acid modifications into hydroxyproline/dihydroxyproline and DOPA, respectively [36]. Mfp-1 has a basic isoelectric point (pI) of ~10, as would be expected due to the dense concentration of positively charged lysine residues, and has a total mass of 108 kDa with 75 decapeptide repeats [14].The abundance of DOPA in the repeats produce a significant distribution of catechol moieties across Mfp-1, reaching levels of at least 10 to 15 mol% [37].

2.3.2 The Role of Catechol-Metal Coordination in Mfp-1

The prevalence of catechol functional groups endows Mfp-1 with a propensity to interact with transition metal ions. Through DOPA, Mfp-1 displays interesting relationships and reactivity with diverse metal ions such as Fe [16, 38], Ca [33], Al [39], and peculiarly, V [25, 40]. This activity leads to the formation of stable metal ion coordination complexes with DOPA's catechol functional group and the metal ion in different conformations with tris- coordination being predominant in Mfp-1 [40, 41]. The stability of these DOPA-metal complexes was shown to be reversible and diverse, as coordination complexes can reform after metal depletion, even with different metal ions such as vanadium or aluminum besides iron [39]. In terms of bond strength, DOPA-metal coordination is convenient - catechol-metal coordination binding strength is close to that of a covalent bond, yet the bonds are capable of reforming if broken [42]. Therefore, catechol-metal coordination can act in a reversible manner, which has important mechanical implications. Catechol polymer networks thus can control cross-linking upon exposure to metal ions, and once formed, can demonstrate robust mechanical performance due to the high bond strength while also being capable of self-healing behaviour as bonds reform after mechanical loading. Additionally, this mechanism of metal coordination is also responsive to certain physicochemical stimuli. Catechol-metal bond formation is sensitive to pH and redox conditions, which can determine the behaviour of bond formation and ultimately if metal coordination will occur [43, 44]. DOPA's catechol functional group is in fact susceptible to oxidation, a feature that can also be exploited to

generate an alternate cross-link strategy through a quinone-tanning process where catechol moieties in DOPA oxidize into quinones that can alternatively form covalent cross-link bonds with other amino acids [43, 45]. In summary, DOPA residues enable Mfp-1 to be highly proficient in a mechanical role by creating a catechol-metal coordinated network that can act in a reversible manner and be sensitive to the surrounding environment.

2.3.3 Identifying Mfp-1 in the Cuticle and Evidence of Cysteine-Rich Proteins in the Cuticle's Matrix

Catechol-metal coordination signatures can be measured by Raman spectroscopy as specific resonance peaks attributed to the metal coordination and catechol-ring bond vibrations [16]. Mapping of these spectroscopic signatures over the cuticle's surface was used to identify where catechol-metal coordination occurred and thereby understand where Mfp-1 localized in the cuticle. Examining the relative signal intensity of DOPA-metal complexes revealed the presence of catechol-based coordination cross-linking concentrated strongly within the granules compared to the surrounding matrix [16]. This identified that Mfp-1 was concentrated in the granules and further, that the granules were a hotspot for catechol-metal coordination giving them tougher mechanical attributes than the surrounding matrix [16, 26]. The question as to what exactly the matrix was comprised of remained.

The concentration of DOPA metal coordination in cuticle granules consequently translate to a concentration of Mfp-1 protein in these structures, and the factors involved in explaining how Mfp-1 can achieve phase separation from the matrix will be discussed later. Initially it was postulated that perhaps differential levels of post-translational modification of tyrosine to DOPA in Mfp-1 may produce alternate forms of the protein which can produce diverging phases downstream [14]. Indeed, gradients of DOPA have been characterised in byssal threads, where DOPA levels decrease in content from the distal to the proximal end of the fiber [37]. Nonetheless, newer findings reveal critical details that better explain what the matrix is made of.

Examinations into elemental differences between the cuticle's matrix and granules gave clues of what the matrix may consist of. A significant difference in metal coordination was noticeable between the granule and matrix, with vanadium deposition dominating in the granule and surprisingly, iron dramatically shifting towards the matrix (Fig. 6) [25]. Concurrently, a major difference in sulfur content was clear as well. The matrix demonstrated much higher sulfur

concentration than the granule in a similar pattern to the deposition of iron (Fig. 5 & 6) [25]. The DOPA rich Mfp-1 granules may preferentially colocalize with vanadium due to its greater coordination bond stability with DOPA compared to iron [40, 46]. This explains why over time, metal coordination species in Mfp-1 would shift towards its most stable conformation with vanadium. However, this also indicated that another coordinating component capable of interacting with iron was present, and most likely was related to the deposition of sulfur since they followed very similar deposition patterns.

Because the matrix is composed of protein like the granule, the major components of the cuticle's matrix would have to be protein that is rich in sulfur, suggesting an elevated content of cysteine due to its sulfur thiol functional group [25, 30, 47]. In such case, the Mfp-1 rich granules would act as a hard cross-linked inclusion surrounded by a cysteine-rich protein matrix. The discovery of putative Cys-rich proteins through transcriptomic studies of the cuticle glands (discussed below) provided potential candidates. Researchers hypothesized that these proteins might coordinate with iron through cysteine-based Fe-S cross-links [25], but there is currently no experimental evidence for this hypothesis. The cysteine-rich proteins also can have additional roles in covalent cross-linking through 5-cysteinyl-DOPA bonds between the granule and matrix, as well as providing a reducing redox environment that can interact with Mfp-1's DOPA [25]

2.3.4 Cysteine-Rich Mussel Foot Proteins

Insights into possible candidates for the sulfur-rich proteins in the byssal thread's cuticle matrix were finally realized when novel putative amino acid sequences from the cuticle gland were identified through a comprehensive transcriptomic analysis [47]. These sequences all were significantly expressed *in vivo* and all demonstrated an elevated content of cysteine that could explain where the sulfur signals in the matrix are originating from [25, 47]. DeMartini et al. performed a transcriptomic analysis of the mussel foot's gland tissues and identified multiple of these Mfp amino acid sequences that may play significant, yet unknown roles in the mature byssus [47]. This study produced new sets of highly expressed genes with similar patterns to the previously known Mfps. Most of the proteins were confirmed to be present in the byssus, leading to the classification of 4 new putative Mfps from the cuticle gland identified as Mfp-16 to Mfp-19 (Fig. 8). In this work, this class of proteins will be referred to as cysteine-rich Mfps. These novel

proteins warrant significant attention as their role in the byssus remains unknown, and it is suspected they explain the characterized concentration of sulfur in the cuticle's matrix and granule (to a lesser extent) [25]. So far, only Mfp-17 has been positively identified through proteomics to be present in the cuticle's vesicles [48].

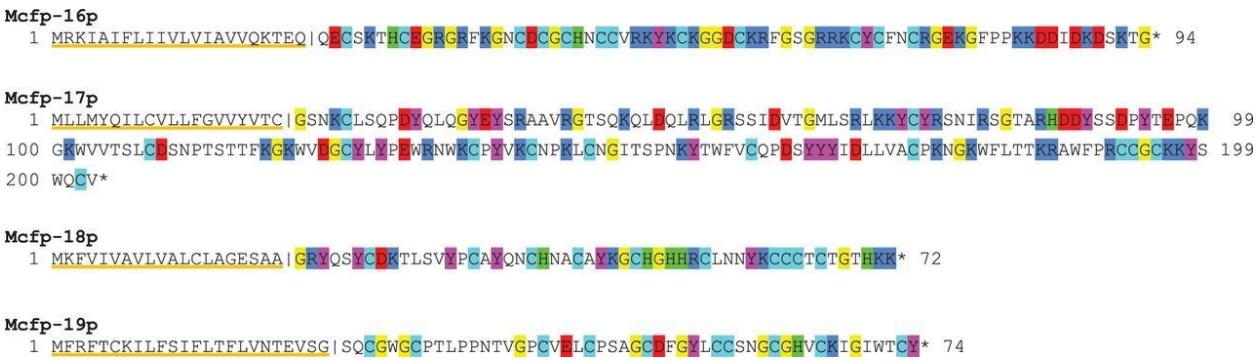

Figure 4. Amino acid sequences for putative cuticle gland Mfps. Signal peptides are underlined orange with cleavage site marked by a vertical line. Amino acids of interest: Positively charged (dark blue), negatively charged (red), tyrosine (magenta), glycine (yellow), histidine (green), and cysteine (light blue). From [47].

All of the novel cuticle proteins are relatively small with a size of 5 to 20 kDa but demonstrate a very high cysteine richness between 7 to 20 mol% [11]. The prevalent richness in cysteine and sourcing of these proteins from the cuticle gland corroborate that they are components of the cuticle matrix [25, 47]. This becomes clear when the properties of these proteins are cross-examined with recent findings by Jehle et al. that clarify the differential elemental composition of the cuticle's granules and matrix in both, secretory protein vesicles (Fig. 5) and in the mature byssus (Fig. 6) [25]. The homogenous distribution of nitrogen ascertains the protein content across the matrix and cuticle, but the difference in sulfur distribution cannot be attributed to Mfp-1 as this protein does not contain cysteine residues, while Mfp-16 to Mfp-19 do. As such, a model of the cuticle matrix being composed primarily by cysteine-rich Mfps explains why sulfur would be differentially distributed away from an Mfp-1-rich granule but not entirely extinct, explaining the empirical observations. Moreover, the phase separation of Mfp-1 displays a gyroid morphology that makes it possible for matrix components to not be completely isolated from the granule and increasing surface area between the granule and matrix [25, 49, 50].

Despite the compelling evidence that these cysteine-rich Mfps may indeed be present in the cuticle with important functional implications, the proteins remain unstudied without any characterization of their properties and behaviour known in literature. Even after all this time, extracting them from the natural source has not been successful even though hints of their cysteine-rich content have been known for considerable time [20, 25, 35]. However, via recombinant protein expression the same amino acid sequences identified can be translated to a heterologous organism by genetic engineering to create microorganisms capable of producing homologous cysteine-rich Mfps to their *in vivo* counterparts, and begin to unravel the role that these proteins could play in the cuticle [10, 51]. That is one of the primary goals of the work in this thesis.

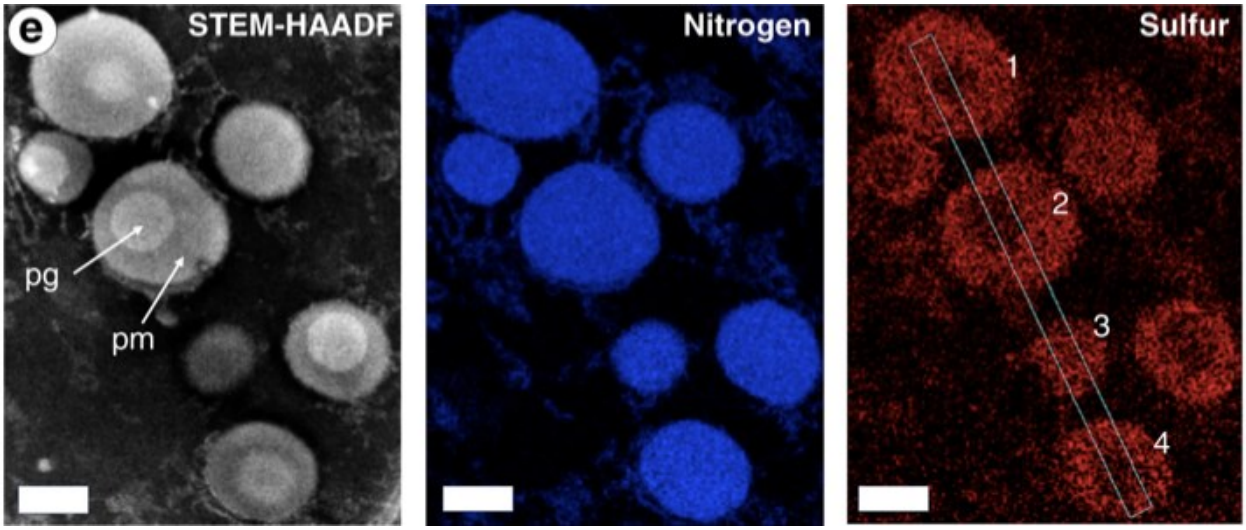

Figure 5. Elemental composition distribution of native cuticle matrix and granule regions in gland vesicles by scanning transmission electron microscopy with energy dispersive X-ray spectroscopy (STEM-EDS). Scale bar = 500 nm. Pm and pg indicate the nascent formation of a protomatrix and protogranule respectively. From [25].

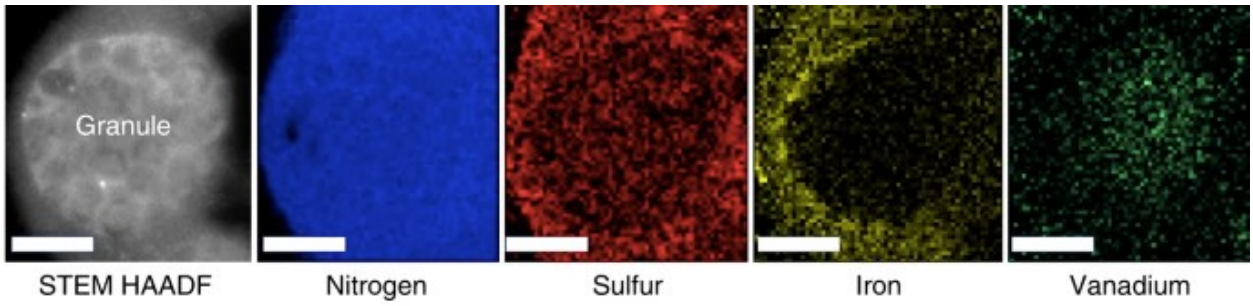

Figure 6. Elemental composition distribution of native cuticle matrix and granule regions in mature byssus by scanning transmission electron microscopy with energy dispersive X-ray spectroscopy (STEM-EDS). Scale bar = 100 nm. From [25].

2.4 Liquid-Liquid Phase Separation in the Cuticle

With the composition of the cuticle introduced, it is worthwhile to delve into the physicochemical parameters by which the phase separation between matrix and granule might be produced in the byssal thread's cuticle. The compositional difference between the cuticle's granule and matrix is thought to arise due to liquid-liquid phase separation (LLPS) between Mfp-1 and the cysteine-rich Mfps within the cuticle secretory vesicles, however, how this occurs is not entirely clear. What is understood is that at least the intrinsic physical properties of the protein building blocks are in place to lend the physical attributes necessary to self-segregate from each other within a liquid environment (Fig. 5). Jehle et al. proposed that the phase separation in the cuticle's granule is derived from a block copolymer structure of Mfp-1, as its N-terminus (non-repeated region) is more hydrophobic compared to the rest of the protein with $[AKPSYPPTYK]_n$ repeats [25]. Thus, this amphiphilic nature of Mfp-1 allows it to remain largely immiscible with the cysteine-rich Mfps, as a result forming a Mfp-1 rich granule within a cysteine-rich matrix. However, what are the factors that play a role in coacervation phenomena?

2.4.1 Principles of Coacervation

In simple terms, coacervation is a liquid-liquid phase separation (LLPS) driven by the mutual attraction of coulombic forces within a charged polymer structure that can be simple or complex; simple coacervation involves the coacervation of a single molecular species while complex involves at least two. Most commonly, complex coacervates form from dissolved polyelectrolytes with opposing charges such that the electrostatic force between them attracts them sufficiently to separate into their own fluid phase [52]. This separated phase is often called the "dense" phase due to the heavy concentration of the polymer chains that increase the phase density, which leaves behind a "dilute" bulk phase. The interesting dynamic of a coacervate system is such that the dense phase retains enough of the solvent to remain liquid as opposed to forming solid aggregates. This is visible at nano-sized scales in the dense phase, where mesh-like formations of the coacervated polymers can be observed with the solvent in-between (Fig. 7e) [53]. While coacervates will initially form small droplets, over time they will coalesce and ripen forming a bulk fluid condensate phase. Notably, it is possible for two immiscible coacervate phases to co-exist with one phase existing as isolated droplets within the other coacervates phase, determined by the relative interfacial energies of the two coacervate phases with the bulk dilute phase [54].

To achieve coacervation, multiple physicochemical factors contribute, including the internal structural features of the polymer species, stoichiometry, macromolecular concentration and the external solvent environment (concentration, pH, temperature, etc). Internal structural features like the polymer's functional groups and size will control how the polymers will attract and can influence the stability or folding of the backbone chain [52, 53, 55]. Stoichiometry and concentration of the coacervating elements are essential to maintain a balanced environment between repulsion and attraction between the polymer species, while having a high enough concentration for the system to form in the first place is crucial [52]. Lastly, the external environment via variables like ionic strength and pH could entirely dictate the progression of the coacervation process. Salt concentration will screen electrostatic interactions and modulate the attraction/repulsion between like- and oppositely-charged functional groups in the polymer [53, 55]. Acidity of the solvent will dictate the protonation level of the functional groups, thereby controlling the charge of the polymer as a function of the solvent's pH. The stability and solubility of the polymer too will be affected by pH by the same effect.

2.4.2 Coacervation Phenomena in Cuticle Mussel Foot Proteins

Given that the success of coacervation will depend primarily on the polymer in question, it is intriguing that the cuticle's protein building blocks can form coacervates [55]. Hybrid proteins designed with partial sequences between Mfp-1 repeats and plaque-derived adhesive proteins achieved complex coacervation with hyaluronic acid (HA) [56]. Interestingly, both components of the hybrid proteins can achieve coacervation on their own. The plaque proteins could coacervate with HA [57], as could Mfp-1on its own [58, 59]. HA is an anionic polyelectrolyte that can evidently interact with the positive charges of Mfps to form complex coacervates. This process is driven by the high basicity of the proteins, giving them a high net positive charge and a high isoelectric point (pH where net charge is zero). Moreover, the coacervation process was managed by managing additional factors as mentioned earlier like ionic strength, pH, and stoichiometry.

More unexpectedly, Mfp-1 and its recombinant versions are capable of forming coacervates with itself as a form of simple coacervation [30, 53]. This process is driven by a transition towards a higher ionic strength like in seawater conditions that supports the aggregation of Mfp-1 to itself. Unlike complex coacervates which would be hindered by an increasing ionic strength, the simple

coacervation of Mfp-1 is enhanced due to the electrostatic screening effect. A greater ionic strength in solution increases the screening of long-range charge interactions, resulting in decreasing like-charge repulsion and opposite-charge attraction [53]. With increasing ionic strength, the repulsion of the positively charged residues in Mfp-1 decreases which 1) enhances the impact of other intra/intermolecular forces and 2) supports protein proximity. Close to the lysine residues in Mfp-1 are tyrosine and DOPA aromatic residues which can interact with positive charges via cation-π interactions. Cation-π interactions are non-covalent attractive forces between a nearby cation and the negative dipole in an aromatic functional group due a disproportionate electron density on the center of an aromatic ring [60]. These interactions are common between positively charged and aromatic amino acids in proteins and can play pivotal roles in function [60]. Given the abundance of both ingredients needed for cation-π interactions in Mfp-1, it makes rational sense that upon decreasing protein repulsion, these forces can begin to stabilize protein coacervation. In fact, Mfp-1 too can coacervate with similar same-charge polymers which confirms the role of cation-π interactions as the driving force of coacervation in the protein [61].

2.4.3 Advantages of Coacervation and Rationale for its Application in Mfps

Coacervates provide multiple advantages that aid in the construction of the byssus thread's cuticle. The most obvious is that it presents an effective mechanism to reduce the space needed to stockpile the proteins that will build the cuticle while at the same time protecting the proteins from diffusion, facilitating a dense protein phase. If the building blocks have a natural tendency to aggregate on their own accord and remain stable under very high concentrations, it facilitates the stockpiling process. The phase separation would also protect against the loss of proteins from diffusion when it comes time to build a thread due to their cohesion as a separate phase. Surface tension is also very low in a coacervate phase [62-64], endowing the liquid coacervate a strong ability to spread and wet surfaces. In the context of cuticle assembly, this is crucial as the coacervate phase would propel the vesicles to spread over the nascent thread core and easily coat its surface. Moreover, the interfacial tension of a coacervate is bound to be heavily influenced by the salt species and their concentration in its vicinity [65]. The ability to automatically segregate biopolymers and its functional groups is another advantage of coacervates. The coacervate phase can possess different viscoelastic properties because it can compartmentalize functional groups that can behave different than the surrounding phase [25]. In the context of Mfp-1, its coacervation allows the segregation

of catechol-metal coordination and thereby endows the granules significantly different properties than the surrounding matrix that are crucial to the mechanical performance of the cuticle. Therefore, the application of coacervation in the cuticle is exceptionally clever due to its facilitation of building block segregation, surface coating, and functional compartmentalization; all of which are crucial to facilitate a rapid, functional assembly of the byssal thread's cuticle.

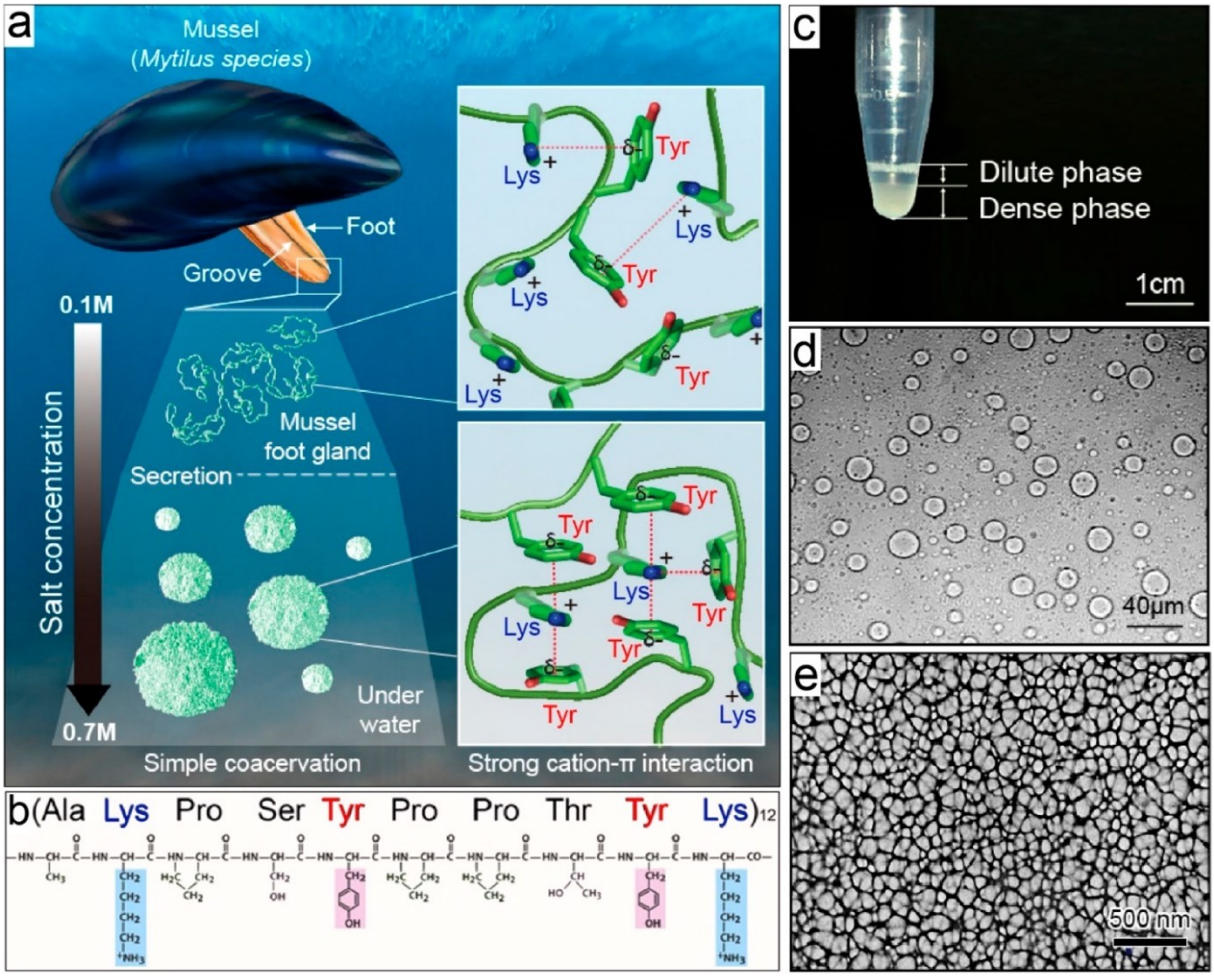

Figure 7. Schematic of the self-coacervation process of recombinant mussel foot protein-1 (rMfp-1) derived π-cation interaction while under a seawater aqueous environment. a) Ionic strength driven simple coacervation of rMfp-1 due to proximity of tyrosine and lysine residues. b) Amino acid sequence of rMfp-1 decapeptide. c) Macroscopic phase separation of rMfp-1 coacervate. d,e) Microscopic morphology of dense rMfp-1 coacervate phase. From [53].

2.5 Evidence of Thiols and Redox Properties in the Cuticle

The high sensitivity of DOPA-metal coordination to oxidation is managed effectively within the cuticle due to the strong redox management abilities of the material, being able to create a reservoir of electron-donating reducing agents that create an antioxidant environment [31]. Similar to the plaque, this is due to the fact that the cuticle building blocks coacervate and generate isolated environments that enhance the proximity of the reducing agents to the oxidizing components, and limit exposure to oxidizing seawater [66]. Further evidence points towards the cuticle cysteine-rich Mfps being the agents responsible for creating such a reducing environment in the cuticle, as an entire thiol-rich layer (TRL) has been identified at the interface between the byssus thread and cuticle [48]. Cysteine-specific maleimide fluorescent staining in the cuticle reveals the presence of cysteine-rich proteins in the TRL, meaning that the cysteine-rich proteins in the cuticle do possess reactive thiol groups that are capable of reducing properties [48]. Such is the reducing strength that even whole byssus threads are able to maintain themselves reduced and also create a reducing environment around them through exposure of its surface. The thread's performance demonstrates strong reducing abilities in the same antioxidant assays used to prove the reducing abilities of cysteine-rich Mfp-6 in the plaque [48, 67, 68]. Critically, this reducing ability in the thread was lost when reacted with iodoacetamide, a thiol-capping agent that reacts with the functional groups and renders them unable to participate in redox reactions, confirming that nearly all of the redox control properties of the cuticle is attributed to reactive thiols from cysteine-rich Mfps [48]. Furthermore, peptide fragments isolated from cuticle vesicles have been indeed found to match to the putative cuticle cysteine-rich Mfps [47, 48]. This is physical evidence pointing that the cuticle cysteine-rich Mfps are in the cuticle vesicles that go on to assemble the cuticle and are likely the agents that build the cuticle matrix and TRL.

2.6 Cysteine-rich Proteins and Iron Binding

2.6.1 Fe-S Cluster Proteins

To understand the possible mechanisms in which cysteine-rich Mfps could interact with iron ions, it was necessary to explore the already-known protein systems that incorporate cysteine as a ligand in the coordination of iron ions. The foremost proteins in this realm are iron-sulfur (Fe-S) cluster-containing proteins, which are fundamental to life in general as they play essential roles in

important biological reactions [69]. These clusters coordinate iron ions with ligating terminal cysteine residues alongside bridging inorganic sulfide anions, assembling into structures ranging from relatively simple planar [2Fe-2S] to complex cubic [4Fe-4S] geometries in different proteins [70]. The notion that a cysteine-rich Mfps could form Fe-S clusters falls apart due to the sensitivity that these co-factors have towards oxygen which can damage or destroy them [70]. In seawater conditions, dissolved oxygen is abundant and would make the formation of these clusters in the exposed cuticle not feasible. Additionally, the formation of these clusters is a complex process that relies on an orchestrated assembly system composed of multiple enzymes within a controlled cellular environment [71]. Since iron ions are incorporated during the byssal thread formation process [22], it is very unlikely that such an orchestrated system is present in the cuticle's vesicles matrix and be capable of achieving cluster formations in the minutes-wide timescale from which the threads form and iron is introduced. As such, it was necessary to find another alternative that may better explain the possible mechanisms of cysteine-iron binding in the context of the cuticle.

2.6.2 Metallothioneins (MTs)

In the search of other candidate protein systems that could resemble similarities to the cuticle cysteine-rich Mfps, metallothioneins stood out as potential candidates due to similar attributes in the amino acid sequences of the proteins, their function, and most importantly, in the way they coordinate metal ions. Metallothioneins (MTs) are a broad class of metal binding proteins that generally have small molecular weight (<10-15 kDa) with significant deposition of cysteine (15 to 30 mol%) [72]. MTs coordinate diverse metal ions through metal-thiolate bonds by cysteine coordination, but whose amino acid sequence can be diverse [72]. Metal ions range from toxic heavy metals to physiological transition metals. These proteins are particularly interesting because they demonstrate redox activity related to managing oxidative stress [73] while at the same time they can bind metal ions with sulfur, both of which are purported to be relevant functions of cuticle cysteine-rich Mfps. In fact, both of these functions appears to be connected in terms of the roles that metallothioneins play *in vivo*, as metal-loaded MTs can be oxidized by cellular oxidants to release metals or inversely metal-free MTs (apoMT) can act as a reducing agents due to available free thiol groups from cysteine that can be oxidized or alternatively can proceed to sequester free metal ions [72]. As such, MTs will proceed towards shifting equilibrium with the metal availability and redox conditions of the cellular environment surrounding the MT. Given an increase in cellular

oxidants, MTs could reduce them and thereby release bound metal ions. Inversely, an abundance of cellular antioxidants will reduce oxidized MTs and thus allow them to uptake metal ions [74]. Moreover, MTs too are thought to act as metal ion storage buffers that can maintain stocks of metal ions and transfer them to other MTs or biomolecules, heavily influencing metal ion homeostasis [74].

2.6.3 Iron Binding in Metallothioneins.

In terms of metal ion species, MTs have a reputation for being highly capable of binding particular metals like Zn(II), Cu(I), and Cd(II) [75]. The challenge becomes in finding evidence that a similar mechanism of metal ion binding is also functional in sequestering iron ions like it would be expected by cysteine-rich Mfps. If MTs are indeed capable of iron binding via cysteine coordination, then it is feasible that a similar mechanism would be responsible for Fe-Cys crosslinks in the cuticle matrix. Early work that attempted to identify potential signatures of iron binding to MT was successful [76] despite earlier attempts that failed in achieving this reaction [77]. To achieve this, high MT and iron concentrations were employed under strict anaerobic conditions as oxygen exposure led to protein precipitation and a breakdown of the reaction. The reaction confirmed that MT from a mammalian source that would normally bind Cd(II), could be processed to remove all bound Cd(II) and exchanged with Fe(II) at a stoichiometric ratio of 20 cysteine residues to 7 iron ions, the same as for Cd-MT [76, 78, 79]. This demonstrates that the coordination of iron by cysteine residues alone occurs in cluster formations that follow a stoichiometric attribute as observed for other metal ions. Moreover, the same Fe(II)-MT cluster formation has also been confirmed to be capable of behaving as a reductant, capable of reducing other proteins within the same environment [80].

Another interesting detail is the fact that formation of Fe-MT clusters appears to be driven at least partially by the pH of the solution, as earlier reaction attempts that proved unsuccessful were all under a pH < 7.5 [77], while it was then found to be possible to form Fe-MT clusters at a pH of 8.3-8.5 [76, 78]. In the context of byssal threads, they operate under seawater whose pH is variable, but always greater than pH 8 and often between 8.2-8.4 [81, 82]. This could be considered a benefit in terms of Fe-cysteine bond formation, as the exposure of byssal threads to seawater would nurture an environment at a pH which could be conducive to Fe-cysteine coordination in the matrix by

cysteine-rich proteins. Seawater does pose a challenge as well, however, since Fe-MT clusters were not able to form under aerobic environments and given the high levels of dissolved oxygen in seawater, it suggests that MT-based iron-cysteine coordination is not very feasible under seawater exposure.

2.6 Principles of Iron Binding Cysteine-Rich Mussel Foot Proteins

While MTs may struggle to form Fe-cysteine clusters in seawater conditions, cysteine-rich Mfps could do it in principle if the differences between them and MTs are considered. Protein amino acid sequence differences directly influence the mechanisms that drive protein functionality. While cysteine-rich Mfps do have similarities in size and cysteine composition with MTs, they too have significant sequence difference that can drive different behaviour. The most obvious difference between MTs and cysteine-rich Mfps is the incorporation of aromatic residues. Unlike MTs which have little to no aromatic residues [72], byssus cysteine-rich proteins have a significant incorporation of aromatic amino acids in their protein sequence (Fig. 4) [47], which could have dramatic modulation in their metal binding properties. The formation of hydrophobic pockets in protein structure from aromatic residues is impacts protein folding, solubility, and even self-assembly processes [83]. Aromatic residues can also stabilize cysteine's reactive thiol groups within hydrophobic protein cores in a way that prevents oxidative disulfide-bridge formations and maintains cysteine reactive as a sulfhydryl [84]. The aromatic rings can modulate cysteine conformation in a protein by pushing the electronegative sulfhydryl group away from the π-electron rich cloud of aromatic amino acids and instead towards the positive hydrogens at the edge of the ring [85].

Moreover, the process of how aromatic amino acids interact amongst themselves has been shown to be influenced by the size and charge of metal ions, including transition metals [86]. In fact, iron ions do demonstrate an interesting effect where they could guide interactions between aromatic residues that impact the folding stability of a protein [87]. During the byssus thread formation process, metal ions are incorporated into the byssal thread's cuticle before exposure to seawater conditions [22]. The idea that iron ions are playing a synergistic role in the cuticle's matrix is plausible. Putting concepts together, it begins to suggest that the cysteine-rich Mfps evolved as proteins that can bind iron via cysteine coordination in a similar fashion to MTs, but through an

evolved incorporation of aromatic residues they gained the capability to stabilize the iron coordination even while under exposure to the normally detrimental conditions of seawater. This capability then opens additional protein functionalities that have never been described before, like the ability to leverage Fe-cysteine coordination from sensitive enzymatic or redox functions towards robust and stable structural crosslinks capable of mechanical work, as it would be expected in the role as a major component of the cuticle's matrix.

3. Thesis Objectives

As laid out in the literature review, the cuticle's cysteine-rich proteins are hypothesized to play three important roles in the formation and function of the cuticle: 1) a strong reducing agent capable of maintaining Mfp-1's DOPA catechol groups in a metal coordinating state, 2) interact with Mfp-1 to undergo coacervation and form distinct cuticle and matrix phases, and 3) crosslink with iron ions via cysteine sulfur coordination to create the cohesive and sacrificial bonds that may be active in the cuticle's matrix.

To provide evidence of these purported roles, it was necessary to first produce the proteins *in vitro* to characterize them. To this extent, recombinant protein expression was the most convenient mechanism to create significant quantities of the proteins and enable *in vitro* experimentation. As such, the investigation process first relied upon the bioengineering of *Escherichia coli* (*E. coli)* with the genes that express Mfp-16 and Mfp-17, the foremost cysteine-rich Mfps in the cuticle due to their longer sequence length than Mfp-18 and Mfp-19 [47]. This distinction is important because the behaviour of each protein is likely different due to having different amino acid composition and length. This also means that Mfp-16 and Mfp-17 are likely to display different functions. Therefore, the **initial project objective** was to genetically engineer *E. coli* with rationally designed gene sequences for the cysteine-rich Mfps, confirm protein expression, and purify them from the rest of the host's proteins.

The next research objectives were to test the hypothesized roles of the cysteine-rich Mfps. We hypothesized that recombinantly expressed Mfp-16 and/or Mfp-17 would 1) display strong reducing properties, 2) demonstrate signatures of iron-cysteine metal coordination via Fe-S bond formation, and 3) would interact with recombinantly produced Mfp-1 in coacervate formation.

To summarize, the following objectives were formulated:

Objective 1: Identify cysteine-rich Mfps as strong reducing agents through biochemical assays that probe for the reducing capabilities of the protein's cysteine functional groups.

Objective 2: Find evidence of cysteine-iron metal coordination bonds between cysteine-rich Mfps and iron ions via spectroscopic techniques and determine how cysteine's functional groups are involved.

Objective 3: Determine if coacervation by rMfp-1 can be achieved with cysteine-rich Mfps and if so, identify whether the cysteine-rich proteins integrate or separate from the rMfp-1 coacervate.

4. Methods

4.1 Genetic Engineering of *E. Coli* Bacteria for Recombinant Expression of Mfp-16 and Mfp-17

4.1.1 Plasmid Design

Plasmid DNA was the vector used to deliver the genetic sequence necessary to express Mfp-16 and Mfp-17 in bacteria. Two plasmids were designed, one corresponding to each protein. The gene sequences were optimized to the codon usage of *E. coli* and inserted at the open reading frame (ORF) of the vector which is after the ribosome binding site (RBS) and before the stop codon of the plasmid. The design is demonstrated in Fig. 8 for Mfp-16. The same design was used for Mfp-17 (not shown). The plasmid was synthesized commercially and designed by a previous student in the lab. Benchling software was used to design the new plasmid construct.

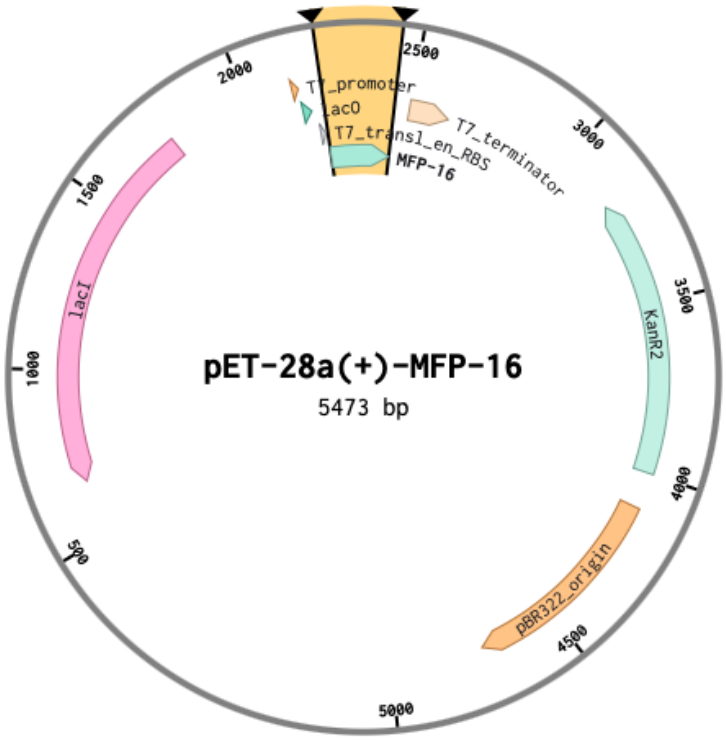

Figure 8. Plasmid map of pET28a(+) with the gene sequence of Mfp-16 integrated between T7 promoter and terminator regions. Sequence regions of interest like the origin of replication, kanamycin resistance gene, and lac operon are annotated.

For this design to be useful, modifications were made to include a 6xHis-tag (his-tag) and a tobacco etch virus (TEV) cleavage site to the protein sequences of Mfp-16 and Mfp-17 (Fig. 9). The his-tag was necessary to facilitate the downstream purification of the protein via chromatography, and the cleavage site for tag removal if desired. The plasmids were genetically engineered to include the additional sequences.

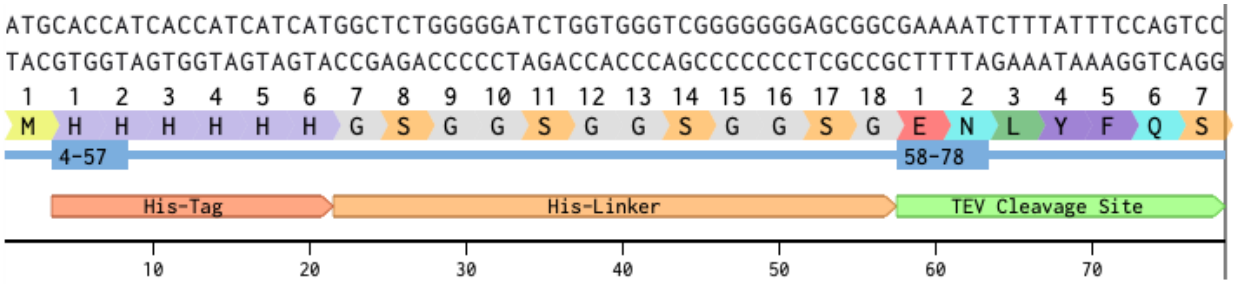

Figure 9. His-tag and TEV cleavage site sequence to be inserted into the pET28a(+) vector at the upstream position of the protein sequence.

4.1.2 Genetic Engineering of the pET28 Vectors

4.1.2.1 Gblock Design

Gibson assembly was used to construct the new plasmids that contained the his-tag and cleavage site. Two Gblocks were designed, one for Mfp-16 and another for Mfp-17. The designs included the his-tag and TEV cleavage sites and were flanked by 20 base pair (bp) overlap regions at both ends, matching to the pET28 vector and the protein sequence (Fig. 10). The 3' overlap began at the lac operon (lacO) region while the 5' overlap began at the beginning of the Mfp sequence. The Gblock DNA was synthesized commercially (Integrated DNA Technologies). The 3' overlap was the same for both designs.

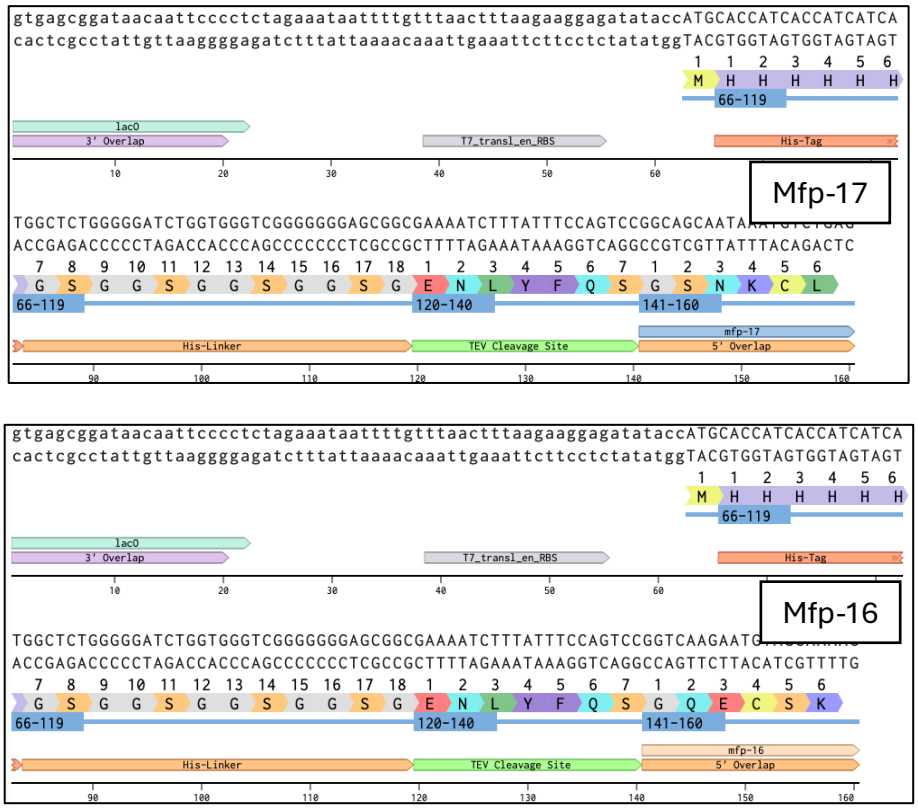

Figure 10. Gblock designs for his-tag and TEV cleavage site introduction into pET28a(+)-Mfp vector with 3'overlap at the lac operon and the 5' overlap at the start of the Mfp sequence.

4.1.2.2 Plasmid Vector Linearization

To prepare for Gibson assembly with the Gblocks, the pET28 vector was linearized via polymerase chain reaction (PCR) with primer pairs that correspond to the overlap regions of the Gblock (Fig. 11). The start of the primers was identical to the start of the overlaps such that the ends of the

linearized vector would overlap exactly with the ends of the Gblock. Since the 3' overlap was identical for both Mfp-16 and-17, only one reverse primer was necessary. The primer design was optimized to have a GC content close to 50%, a length of ~22 bp, and a melting temperature of ~ 65ºC. The primers were synthesized commercially (Integrated DNA Technologies).

The PCR reaction was set up based on a commercial protocol for Phusion® High-Fidelity DNA Polymerase (M0530) (New England Biolabs). A 50 µL reaction was set up in a 200 µL PCR tube on ice: 10 uL of Phusion HF 5x buffer, 1 µL of 10 mM dNTPs, 2.5 µL of forward primer at 10 µM, 2.5 µL of reverse primer at 10 µM, 0.5 µL of Phusion DNA Polymerase, 0.5 µL of 100-150 ng/µL pET28 vector template, and 33 µL of ddH_2O. The reaction was loaded onto a preheated thermocycler at 98ºC and loaded into a vector linearization thermocycling program: 30s initial denaturation, 10s denaturation at 98ºC, 20s annealing at 58ºC, extension at 72ºC for 120s, for 28 cycles and a final extension for 5 min. After vector linearization PCR, the reaction mix was digested with 1 µL of DpnI restriction enzyme for 60 min at 37ºC to degrade the original template pET28 plasmid DNA, then at 80ºC for 20 min to degrade the DpnI enzyme.

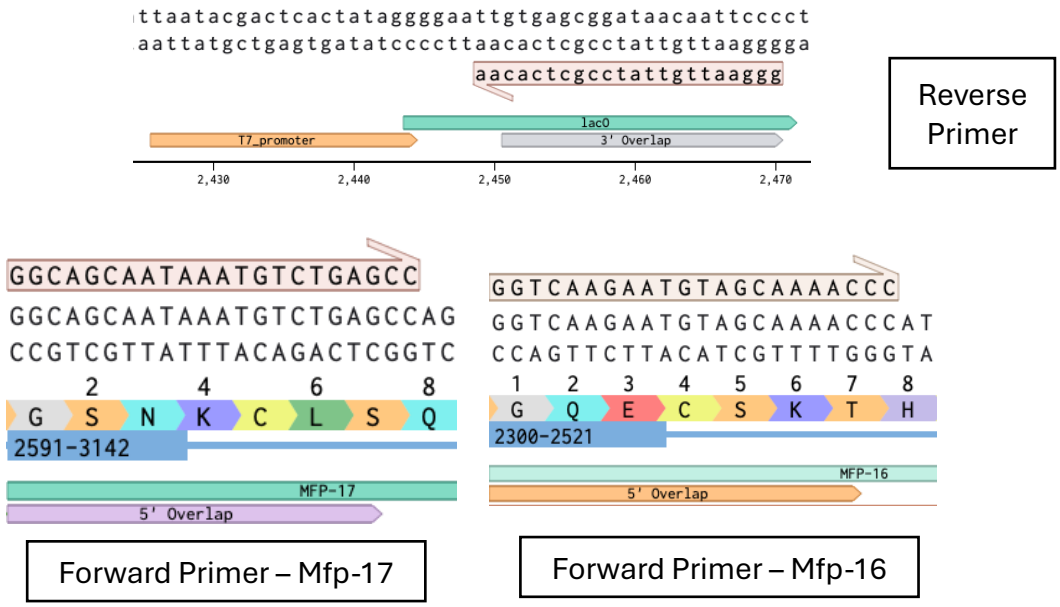

Figure 11. Vector linearization primers used to amplify pET28-Mfp vector into a linear DNA strand for Gibson assembly with the Gblocks.

4.1.2.3 Gibson Assembly and Bacterial Transformation

The Gibson assembly reaction was assembled on ice. A 15 µL aliquot of Gibson assembly master mix, the linearized vector solution, and the Gblock solution were thawed on nice. The Mfp-17 Gibson assembly reaction was assembled as follows: to the master mix aliquot, 1 µL of linear pET28 vector, 1.4 µL of 40 ng/µL Gblock, and 2.6 µL of ddH_2O were added to a final volume of 20 µL. For Mfp-16, 3.3 µL of vector and 1.7 µL of Gblock were added to 15 µL of Gibson master mix. The reaction was mixed and centrifuged briefly, then incubated at 50ºC for 1 hr.

The Gibson reaction was used to perform bacterial transformation on MACH.1strain of *E. coli* cells by electroporation. To transform the cells, the Gibson reaction, electroporation cuvette, and electrocompetent cells were thawed on ice. To the 50 µL of electrocompetent cell aliquot, 1 µL of Gibson reaction was added, then transferred altogether to a chilled cuvette. The cuvette was then transferred to a Bio-Rad Micropulser Electroporator instrument and pulsed at the bacterial setting to transform the cells. Right away, 0.5 mL of SOC media (20 µL of sterile 20% glucose per 1 mL of Luria broth (LB) media) was added to the cuvette and mixed. The transformed cells were then transferred to a sterile glass tube and incubated for 1 hr at 37ºC while shaken at 250 rpm. After incubation, 0.25 mL of the transformed cells were plated in LB agar media with 50 µg/mL kanamycin for antibiotic selection of the genetically engineered transformed cells. The agar plates were labelled and incubated at 37ºC overnight.

Single colonies were selected from the transformation agar plates after incubation and sub-cultured into LB media for plasmid DNA extraction by miniprep. The colony was selected with a micropipette and ejected into a sterile glass tube containing 5 mL of sterile LB media with 50 µg/mL kanamycin. The culture was incubated overnight at 37ºC while shaken at 250 rpm. The plasmid was extracted using a QIAprep Spin Miniprep Kit (QIAGEN) and its specific protocol. After extraction, the DNA concentration of the harvested plasmid was measured using a NanoDrop One^C instrument (ThermoFisher Scientific) using the pedestal mode. The plasmid DNA was sent for Sanger sequencing using service provided by Genome Quebec based on T7 promoter primers to confirm a successful Gibson assembly reaction.

4.2 Recombinant Protein Expression of Mfp-16 and Mfp-17 In *E. Coli*

4.2.1 Recombinant Protein Expression Examination by SDS-PAGE and Western Blot

4.2.1.1 SDS-PAGE

The newly assembled pET28 vector was transformed into the protein expression PQN4 *E. coli* strain following the same protocol as above. A single colony was selected with a micropipette tip and sub-cultured into 5 mL of LB media with 50 µg/mL of kanamycin and incubated overnight at 37ºC while shaken at 250 rpm. Then, 50 µL of the inoculated media was transferred into another 5 mL of fresh LB media and incubated at 37ºC while shaken at 250 rpm until the optical density (OD) at 600 nm of the culture reached 0.6. The optical density was measured using a NanoDrop One^{C} instrument (ThermoFisher Scientific) blanked with LB media. Recombinant protein expression was induced by adding 2 M IPTG (Isopropyl ß-D-1-thiogalactopyranoside) to the cell culture at 0.6 OD600 to reach a concentration of 1 mM IPTG and was incubated overnight at 37ºC while shaken at 250 rpm.

The cell cultures with and without IPTG-induced protein expression were compared via SDS-PAGE (Sodium dodecyl sulfate – polyacrylamide gel electrophoresis). Laemmli sample buffer was prepared at a 5% beta-mercaptoethanol concentration by mixing 10 µL of the reducing agent into 190 µL of 2x Laemmli sample buffer (Bio-Rad), then vortexing the solution to mix evenly. In 200µL PCR tubes, 20 µL of the cell cultures were added into 20 µL of the 2x Laemmli sample buffer for culture samples with and without IPTG. A thermocycler instrument was preheated to 90ºC, and the prepared samples were loaded and incubated at 90ºC for 5 min. A Mini-PROTEAN Tetra cell (Bio-Rad) was assembled and connected to its power supply. An Any kD Mini-PROTEAN TGX 10-well precast protein gel was prepared and loaded into the cell. The cell was loaded with 1x tris-glycine running buffer (25 mM tris, 192.4 mM glycine, 3.4 mM SDS, pH 8.3) to the indicated mark, then 35 µL of each sample and 5 µL of Precision Plus Protein Dual Colour Standard (Bio-Rad) was loaded into individual gel wells. The gel electrophoresis was run at 200 V for 30 min. The protein gels were stained with Coomassie Blue R-250 solution for 25 min (1 g/L Coomassie Blue R-250, 50% methanol, 10% glacial acetic acid, 40% ddH_2O) then destained for ~ 2 hrs with destaining solution (50%v/v methanol, 10% glacial acetic acid, 40% ddH_2O) until the protein bands became discernable in the gel.

4.2.1.2 Western Blot

To do western blot, the same steps as SDS-PAGE were followed until the step of adding Coomassie Blue staining solution. To prepare the transfer buffer, 10 mL of 5x Trans-Blot Transfer Buffer (Bio-Rad) was combined with 30 mL of ddH_2O and 10 mL of ethanol to make 50 mL of 1x transfer buffer. A Trans-Blot Turbo RTA Transfer kit with PVDF membrane (Bio-Rad) was used. To prepare the transfer stack components, 4 transfer sheets were submerged in 1x transfer buffer for at least 3 min, while the PVDF membrane was submerged in methanol for 3 min then in 1x transfer buffer for 3 min. The transfer stack was prepared by laying 2 transfer sheets on a Trans-Blot Turbo (Bio-Rad) instrument tray with tweezers and rolling them to remove air bubbles. Then, the PVDF membrane was placed on top of the bottom transfer sheets, and consequently, the SDS-PAGE gel was positioned directly on top of the PVDF membrane. Lastly, the remaining 2 transfer sheets were placed on top of the gel and rolled to remove air bubbles and adjust the gel positioning to the membrane. The tray was closed and loaded into the Trans-Blot Turbo instrument. The transfer program for 1 mini TGX was loaded and ran for 3 min. The blot stack was taken apart, and the PVDF membrane incubated in 50 mL of blocking buffer (2.5g bovine serum albumin in 50 mL 1x TBST (Tris-buffered Saline, Tween) at 20 mM tris, 150 mM NaCl, 0.1% v/v Tween) for 1 hr under gentle shaking. The antibody solution was prepared by diluting 10 µL of anti-His horseradish peroxidase (HRP) antibody into 10 mL of 1x TBST. The 10 mL antibody solution was added to the membrane and incubated overnight at 4ºC under gentle shaking. To clean the membrane, the membrane was rinsed 3 times with TBST for 10 min each. To image the western blot membrane, a Clarity Western ECL Substrate (Bio-Rad) was used by mixing 5 mL of the peroxide reagent with 5 mL of the luminol/enhancer reagent exactly before imaging, then incubated with the membrane for 5 min under darkness. After incubation, the western blot membrane was imaged with a ChemiDoc imaging system (Bio-Rad) under a chemiluminescence filter.

4.2.2 Large Scale Recombinant Protein Expression

4.2.2.1 Glycerol Stock Preparation and Protein Expression Agar Plates

A glycerol stock of transformed PQN4 *E. coli* was prepared for long-term storage of Mfp-16 and Mfp-17 expressing strains and future protein expression. The same transformed bacterial culture used to prove recombinant protein expression by SDS-PAGE and western blot was used for the

glycerol stock. To make the stock, 500 µL of overnight culture grown in LB and 50 µg/mL kanamycin was added into 500 µL of sterile 50% glycerol solution in a screw-top vial and mixed gently. The tube was then immediately placed under -80ºC for long-term storage.

To make prepare an agar plate for expression, the frozen glycerol stock was lightly scraped at the top with a micropipette tip quickly without letting the frozen stock thaw. The cells were then spread across the surface of a LB agar plate with kanamycin, and the plate was incubated overnight at 37ºC.

4.2.2.2 Large Scale IPTG-Induced Protein Expression

A single colony was selected from sub-cultured PQN4 *E. coli* transformed with pET28-Mfp-16 or -17 vector (from glycerol stock) and plated on an LB agar plate with kanamycin (protein expression plate). The colony was picked with a micropipette into 5 mL of LB media with 50 µg/mL kanamycin and grown overnight at 37ºC shaken at 250 rpm. The 5mL small-scale culture was transferred to 500 mL of fresh LB (1:100) with 50 µg/mL kanamycin in a 1L Erlenmeyer flask and grown at 37ºC and 250 rpm until it reached an OD600 of 0.6 (~2-2.5 hours) to effectively begin the large-scale culture. At this point, 125 µL of 2M IPTG was added to the 0.5L large-scale culture to reach a final concentration of 0.5 mM IPTG in the culture. The culture was incubated for 4-5 hours at 37ºC and 250 rpm to express the recombinant Mfps. The culture was split into two large centrifuge bottles with 250 mL in each and centrifuged at ~4000xg at 4ºC for 20 min to create a wet cell pellet. The supernatant was slowly poured off, and each cell pellet dissolved in 10 mL of cell lysis buffer (6 M guanidine hydrochloride, 500 mM NaCl, 100 mM Na_2PO_4, 10 mM imidazole, pH 8). The 20 mL of dissolved cell pellet was transferred to a 50 mL falcon tube and frozen overnight at -80ºC.

4.3 Immobilized Metal Affinity Chromatography (IMAC) Purification of His-tagged Mfp-16 and -17

4.3.1 Cell Pellet Homogenization by Microtip Sonication

The cell pellet falcon tube was thawed in cold water then placed on ice. A microtip sonicator was assembled and its tip cleaned with ethanol. The cell pellet falcon tube was anchored in the ice to cover its entire outside surface and prevent its movement. The sonicator's tip was carefully lowered and placed in contact with the dissolved cell pellet inside the middle of the falcon tube,

preventing the tip from touching the bottom or sides of the falcon tube. The sonicator was used for 6 cycles, 30s on and 30s off for a total of 6 min. The solution becomes less viscous. The sonicator tip was lifted off the falcon tube, cleaned with ethanol, and the instrument disassembled. The sonicated cell pellet tube was centrifuged at ~4000xg for 2 hrs at 4ºC to pelletize the cellular components. The supernatant was kept and transferred to a new falcon tube and labelled as a cleared cell lysate corresponding to Mfp-16 or Mfp-17 depending on the cell type that was processed.

4.3.2 IMAC Protein Purification

A gravity-flow Econo-pac chromatography column (Bio-Rad) was assembled with a 5 mL bed volume of Ni-NTA agarose (QIAGEN) and equilibrated with 5 bed volumes (bv) of cell lysis buffer. To the column, 10 mL of the cleared lysate (Mfp-16 or Mfp-17) was added and shaken lightly to mix the agarose resin with the lysate. The column was labelled and incubated for 30 min at room temp while shaken lightly. A wash buffer (6 M guanidine hydrochloride, 500 mM NaCl, 100 mM Na_2PO_4, 10 mM imidazole, *pH 6.3*) and an elution buffer (6 M guanidine hydrochloride, 500 mM NaCl, 100 mM Na_2PO_4, 10 mM imidazole, *pH 4.5*) were prepared by carefully adding droplet amounts of 12M hydrochloric acid (HCl) to cell lysis buffer aliquots to reach the desired pH. After incubation, the column was placed in a vertical stand and opened to let the cell lysate flow out of the column. The top of the column was capped with a petri dish lid to prevent airborne particles from going inside while allowing air to escape. The column was washed with 10 bv of wash buffer (50 mL) in 2 cycles with 5 bv each (25 mL). To elute the recombinant protein of interest, 5 bv of elution buffer were added and collected into a falcon tube. The column was reequilibrated with 5 bv of cell lysis buffer and stored at 4ºC for reuse.

4.3.3 Recombinant Protein Concentration and Cleaning

IMAC elutions were combined and loaded into 3 kDa (Mfp-16) or 10 kDa (Mfp-17) Microsep (5 mL) Advance Centrifugal devices with Omega membrane (Pall Corporation) filtered tubes to a volume of 5 mL per tube and centrifuged at ~4000xg for 30 min at 4ºC. If necessary, more IMAC elutions were loaded into the centrifugal tubes and centrifuged accordingly between 10-30 min to reach a final volume ~0.2-0.5 mL of concentrated protein solution above the tube filter. These concentrated protein fractions were collected, combined, and loaded again into the filter tubes for

another round of centrifugation concentration at ~4000xg for 30 min at 4ºC until a final volume of 0.2-0.5 mL of concentrated protein solution remained above the filter. This cycle was repeated until a final volume of < 2mL of protein concentrate was achieved in total from the IMAC elutions.

The final concentrated protein fraction was reduced chemically using dithiothreitol (DTT) or alternatively by tris(2-carboxyethyl) phosphine (TCEP). With DTT, the protein fraction pH was raised by adding droplet amounts of 8M NaOH or lesser to reach a pH between 7.5-8.5 and adding solid DTT to reach a 5-10 mM concentration. With TCEP, pH adjustment was not necessary and solid TCEP was added to the protein fraction to reach a 10 mM concentration. The reducing agents were incubated in the protein fraction for 30 min. The buffer salts from the elution buffer alongside the reducing agents in the protein solution were removed via dialysis against 5-10 mM sodium acetate buffer pH 3.6. A 3.5 kDa, 3 mL Pur-A-Lyzer Maxi Dialysis kit (Millipore-Sigma) was loaded with the reduced concentrated protein fraction against 1 L of acetate buffer for 2 hours, then another 2 hours with 1 L of fresh acetate buffer, and overnight with another 1 L of fresh acetate buffer all while stirred at 300 rpm with a stir bar. The dialyzed protein fraction was collected and loaded into two 2 mL Eppendorf tubes and centrifuged for 1 min at 14,000xg to pelletize protein precipitates. The supernatant was collected into a new Eppendorf tube and the protein concentration was calculated. Protein concentration was calculated by using the measured light absorbance of the protein solution at 280 nm (measured with a Nanodrop OneC instrument) and the molar absorptivity of Mfp-16 or Mfp-17 in the Beer-Lambert law equation. The concentrated and cleaned protein stock was stored at 4ºC with acidic acetate buffer at pH 3.6 for experiments.

4.4 Reducing Properties Biochemical Assays

4.4.1 Ellman's Assay

Ellman's reagent solution was prepared in 25 mL of buffer 7.0 (100 mM Na_2PO_4, 0.2 mM ethylenediaminetetraacetic (EDTA), pH 7.0) with 10 mM of 5,5'-dithiobis-(2-nitrobenzoic acid) (DTNB) and 10 mM of cystamine dihydrochloride [88]. The solution was aliquoted to 1 mL in Eppendorf tubes and frozen at -20ºC for future use. When used, it was thawed at room temperature and used within 2 hours of thawing. The Ellman's sample buffer was prepared using phosphate buffer at pH 8 (0.1 M dibasic sodium phosphate, 2% SDS, 0.5 mM EDTA, pH 8). The reaction was assembled in a 1 cm cuvette: reagent buffer was added, followed by 0-50 µL of the protein

sample, and 20 µL of the Ellman's reagent solution to a final 1 mL reaction volume. The reaction was mixed by aspirating 500 µL with a micropipette 3 times and left to incubate for 5 min at room temperature. The samples were centrifuged at 10,000xg for 1 min to separate protein solids. Light absorbance of the solution was measured at 412 nm in a Nanodrop OneC instrument. A negative control was prepared by combining 980 µL of reagent buffer with 20 µL of reagent solution, and light absorbance at 412 nm was measured as well.

4.4.2 DPPH Assay

DPPH (2,2-diphenyl-1-picrylhydrazyl) reagent solution was prepared in methanol (2mM DPPH), covered in aluminum foil to protect from light, and frozen at -20ºC [67]. The sample buffer was based on phosphate-citrate buffer and was prepared by combining 0.1 M citric acid and 0.2 M disodium phosphate at different ratios for different buffer pH levels [89], and supplemented with with Triton X-100 to stabilize DPPH solubility (0.1 M phosphate-citrate, 0.3% v/v Triton X-100) [67]. The protein sample was diluted in sample buffer to a final volume of 950 µL in a 1 cm cuvette according to the desired protein molar concentration. The reaction was started by adding 50 µL of DPPH reagent solution and immediately mixing 3-5x by aspirating 500 µL. The light absorbance at 515 nm was measured at 2, 5, 10, 15, 30, 45, and 60 min while the reaction was kept in the dark. Images of the cuvettes were taken at the beginning and the end. A negative control was prepared by combining 950 µL of sample buffer (without protein sample) and 50 µL of DPPH reagent solution and measuring its light absorbance at 515 nm at the beginning and the end of the reaction.

4.5 UV-Vis Spectroscopy

4.5.1 Mfp-17 Iron Binding in Acidic Conditions and Different Oxygen Exposure

Iron (II) acetate solutions (FeAc) (0.6-0.7 mM) were made in pH 3.6 buffer (100mM sodium acetate) with and without dissolved oxygen (buffer was sparged with compressed N_2 for 20 min before adding the iron salt to remove dissolved oxygen (DO)). Sample solutions were made in buffer with and without DO by diluting 50 µL of ~4 mg/mL (~160 µM) Mfp-17 protein stock in pH 3.6 buffer with 150 µL of FeAc solution (0.6 mM) for a final protein and iron concentration of ~40µM and 150 µM respectively (1:3.75). The blank solutions were made by instead diluting Mfp-17 stock solution in pH 3.6 buffer with and without DO instead (no iron). In total, 4 solutions were produced: 2 sample solutions with the same iron and Mfp-17 concentrations between them, but

one being in a buffer without DO (replaced with N_2); 2 blank solutions with the same protein concentration (no iron), but one is in a buffer without DO. UV-Vis light absorbance spectra was measured on the blank and sample solutions immediately after adding the iron solution and light mixing, after 15 min incubation, and overnight

4.5.2 Mfp-17 Binding with Increasing Iron Concentrations in an Acidic Environment and Different Oxygen Exposure

Two concentrated FeAc solutions were made in pH 3.6 buffer (100 mM iron (II) acetate) separately in buffers with and without DO. Like the previous experiment, a 200 µL sample was made by diluting 50 µL of Mfp-17 stock in 150 µL of pH 3.6 buffer with and without DO. Blank solutions were similarly made by aliquoting 200 µL of the buffer without any Mfp-17, also with and without DO separately. This formed 4 solutions: 2 sample solutions with Mfp-17 at ~40 µM in pH 3.6 buffer with and without DO, and 2 blank solutions of pH 3.6 buffer with and without DO. To the 200 µL sample and blank solutions with DO, concentrated FeAc solution in buffer without DO was dispensed in very small volumes to increase FeAc concentration (1 µL added → 0.5 mM FeAc increase in sample concentration). After dispensing, the samples were vortexed briefly to mix and centrifuged slightly to remove any particulates in the solution. The UV-Vis light absorbance spectra were measured for each increase in iron concentration by blanking with the solution without Mfp-17 at the same iron concentration. The same process was repeated in parallel with the solutions in buffer with DO. The same procedure above was repeated with concentrated solutions of different transition metal salts individually, including iron (II) chloride, iron (III) chloride, zinc acetate, and nickel chloride at 100 mM in buffers with and without DO.

4.5.3 Mfp-17 Iron Binding In Acidic And Reducing Environment

A pH 3.6 buffer (5 mM sodium acetate, 0.3 mM TCEP) with reducing agent was prepared. In this buffer, a 200 µL Mfp-17 sample (30 µM) was prepared by diluting from a concentrated stock stored with the same pH 3.6 buffer. A concentrated FeAc solution was prepared in pH 3.6 buffer (100 mM). This solution was aliquoted to the 200 µL Mfp-17 sample 1 µL at a time to increase FeAc concentration in the protein sample by 0.5 mM. After adding the iron solution, the sample was lightly vortexed to mix. A blank solution was prepared in-parallel with the sample by aliquoting the same volume of FeAc concentrate into 200 µL of pH 3.6 buffer. UV-Vis light

absorbance spectra were measured after each increase in iron concentration with the blank solution in a Nanodrop OneC instrument (ThermoFisher). Further, the same experimental procedure was repeated in pH 3.6 buffer without reducing agent (5mM sodium acetate, 0 mM TCEP). To test Fe^{3+} ions, the same procedure was repeated with 100 mM $FeCl_3$ in pH 3.6 buffer instead of FeAc.

4.6 X-ray Photoelectron Spectroscopy (XPS)

4.6.1 XPS Measurements of Mfp-17 and Iron in Aqueous Environment

Two Mfp-17 samples were prepared by diluting concentrated Mfp-17 stock in pH 3.6 buffer (100 mM sodium acetate) to 5 µM in 4 mL of pH 3.6 buffer. To each sample, a 10 mM concentration of $FeCl_2$ and $FeCl_3$ was added. The samples were incubated at room temperature for 1 hr. To filter out the iron salt, the samples were added to a 10 kDa Microsep Centrifugal device (Pall Corporation) and centrifuged for 4 cycles at ~4000xg, 4ºC for 20-35 min to a reduce the sample volume from 4 mL to 0.2 mL each cycle. After each cycle, the sample volume was increased back to 4 mL with pH 3.6 buffer before centrifuging again. The XPS sample was prepared by drop casting a protein film on a glass slide by micropipetting 20 µL of the filtered Mfp-17-iron samples on the glass surface and drying it overnight in a vacuum desiccator. The glass slide was loaded onto a Nexsa G2 Surface Analysis System (ThermoFisher Scientific) and XPS measured with an Al K-Alpha X-ray source on the surface of the protein films. Negative controls were also measured on solid $FeCl_2$ and $FeCl_3$.

4.7 Raman Spectroscopy

4.7.1 Raman spectroscopy of Solid-State Mfp-17 with Iron

The solid-state material was prepared in the same manner as samples for XPS (Refer to 4.6.2). Briefly, concentrated Mfp-17 was precipitated in neutral buffer and exchanged into acidic buffer. Iron was added and quickly removed by multiple washes with acidic buffer, carefully keeping the material intact. The buffer was exchanged into neutral pH, then removed by washing with water. The iron-coordinated solid Mfp-17 was placed on a glass slide by aspirating the material and depositing it carefully with a micropipette to effectively create thinly layered section of the material to minimize fluorescence. Raman spectra were measured on an Alpha 300R confocal Raman microscope (WITec) using a 532 nm laser at a power between 3-5 mW and focused on a 100x objective (Zeiss, numerical aperture: 0.9) and a thermoelectrically cooled CCD detector

behind a 600 g/mm grating. To improve signal resolution of the spectra, 30 acquisitions at an integration time of 20-30 sec were used. WITec ControlFIVE 5.1 software was used to operate the instrument as well to perform background correction.

4.7.2 Raman Spectroscopy of rMfp-1 And Mfp-16/17 Coacervates

After coacervate deposition on a glass slide, Raman spectra were measured on an Alpha 300R confocal Raman microscope (WITec) using a 532 nm laser at a power at 12 mW and focused on a 100x objective (Zeiss, numerical aperture: 0.9) and a thermoelectrically cooled CCD detector behind a 600 g/mm grating. Spectra were acquired using 10 acquisitions at an integration time of 5 sec were used. WITec ControlFIVE 5.1 software was used to operate the instrument as well as to perform background correction.

4.8 Coacervation of rMfp-1 and Mfp-16/17

Highly concentrated stock solution of rMfp-1 was made by dissolving 2 mg of rMfp-1 in 20 µL of buffer at different pH levels to reach a concentration of 100 mg/mL. Concentrated Mfp-16 and Mfp-17 solutions were prepared separately by centrifuging though a 0.5 mL 10 kDa centrifuge filter to reach concentration ~100 mg/mL based on light absorbance at 280 nm. The protein solutions were mixed at an equal 1:1 ratio to reach a volume ~15 µL in total. Concentrated NaCl solution (6M) was added to the reaction volume to increase ionic strength and induce coacervate formation. A small volume of the reaction ~4 µL was added onto a glass slide and imaged under a light microscope.

4.9 Surfaces Forces Apparatus Examination of Mfp-17 Mica Films

The mica surfaces were coated with Mfp-17 by placing 30 µL of 100 µg/mL Mfp-17 solution (5 mM acetate buffer, pH 3.6) on the surface and incubating for 30 min. The protein solution was rinsed with pH 3.6 buffer. Iron solutions were prepared at 10 and 100 µM $FeCl_2$ in pH 3.6 buffer and reacted on the surface by depositing 30 µL on top of the Mfp-17 coated mica surface, then incubated for 30 min. The reaction pH was changed by rinsing the iron solution from the surface with pH 7.0 buffer (10 mM HEPES). SFA force-distance profiles were measured at each stage: after protein deposition, pH 3.6 buffer exchange, iron solution exposures, pH increase, and at longer contact times.

5. Results and Discussion

5.1 Genetic Engineering of pET28-Mfp-17 and -Mfp-16 Plasmid Vectors

To meet the initial objective of this project it was necessary to construct plasmids that contained a his-tag so that the recombinantly produced cysteine-rich cuticle Mfps could be isolated. A Gblock was designed (Fig. 10) to include the his-tag alongside a flexible linker region and a cleavage site. The Gblock designs for Mfp-16 and Mfp-17 were similar, and both matched the native nucleic acid sequence overlaps of the pET28 vector to achieve a seamless assembly of the Gblock fragment and linearized pET28 vector via Gibson assembly. After performing Gibson assembly, *E. coli* competent cells were transformed with the assembly reaction product to propagate the newly assembled plasmids. Plasmid DNA was harvested from the transformed cell colonies by DNA miniprep and was genetically sequenced with T7 promoter PCR primers that probed for the successful insertion of the Gblocks into the pET28 vector. The sequencing results were used to create a multiple sequence alignment for both Mfp-17 (Fig. 12) and Mfp-16 (Fig. 13).

In the sequence alignments, the samples containing the desired plasmid sequence are visible by identically matching the DNA sequence of the plasmid vector containing the his-tag, linker, and cleavage site regions. Sample 2 and Sample 1 & 3 for Mfp-17 and Mfp-16 respectively, contained the genetically engineered pET28 vector that could be further used to recombinantly express and isolate the cysteine-rich cuticle Mfps. False positives do appear due to spectator linear pET28 vector uptaken by *E. coli* that would have the kanamycin resistance gene that permits them to survive after transformation, but not the desired additional fragments since it did not react in the Gibson assembly reaction.

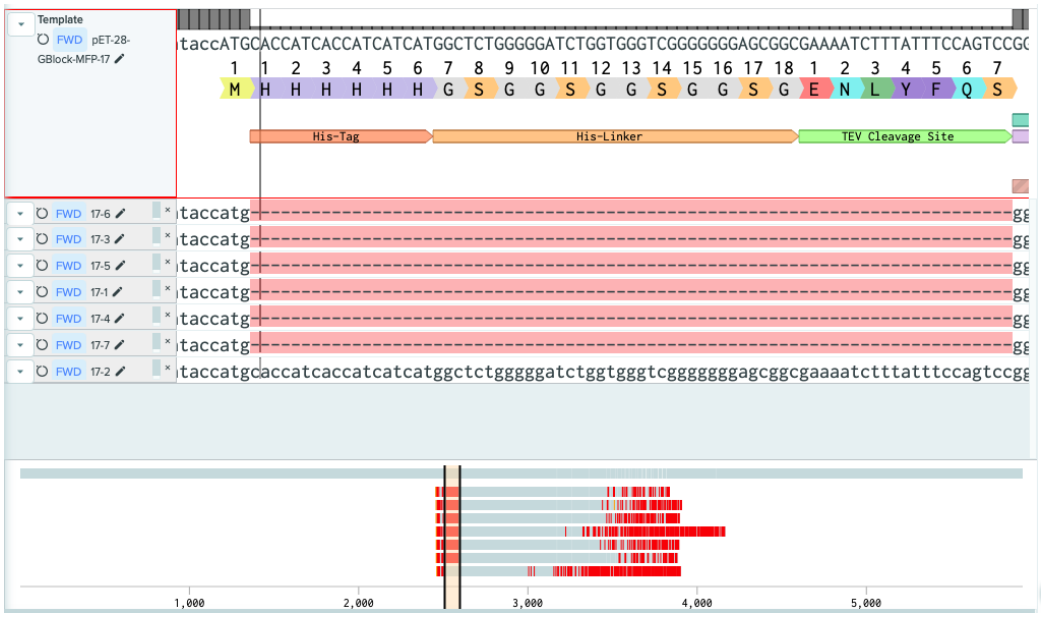

Figure 12. Multiple sequence alignments of sequenced plasmid DNA extracted from genetically-engineered *E. coli* colonies, demonstrating a successful Gblock assembly in Mfp-17 sample #2 (bottom).

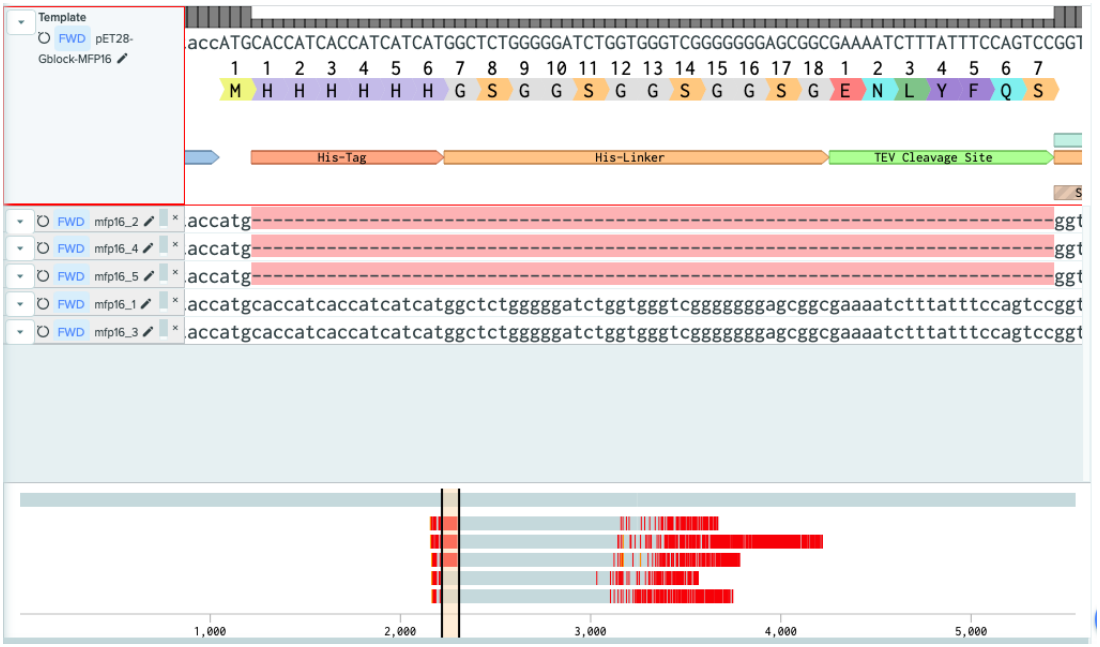

Figure 13. Multiple sequence alignments of sequenced plasmid DNA extracted from genetically-engineered *E. coli* colonies, demonstrating a successful Gblock assembly in Mfp-16 sample #1 and 3 (bottom).

5.2 Recombinant Protein Expression of Cysteine-Rich Cuticle Mfps

The controlled expression of Mfp-16 and Mfp-17 was examined by SDS-PAGE and western blot to determine if *E. coli* was successful in heterologous production of the proteins. Initial small-scale expression of the cysteine-rich Mfps with 1mM IPTG overnight is demonstrated in Fig. 14. The electrophoresis demonstrates the separation of cellular protein content by molecular weight, visible as bands that can be compared against a protein ladder with known molecular weight. Bands close to 15 kDa and 25 kDa form after IPTG-induced protein expression for *E. coli* strains transformed with Mfp-16 and Mfp-17 pET28 respectively. The theoretical molecular weights for the recombinant versions of Mfp-16 and -17 are 10.8 and 23.9 kDA respectively (including his-tag, linker, and cleavage site). The formation of these bands in *E. coli* culture with IPTG is evidence of IPTG-induced recombinant protein expression as the bands are very close to the expected molecular weight and only formed upon exposure to IPTG, a stable and effective artificial analog of lactose [90].

The controlled expression of Mfp-16 and Mfp-17 was examined by SDS-PAGE and western blot to determine if *E. coli* was successful in heterologous production of the proteins. Initial small-scale expression of the cysteine-rich Mfps with 1mM IPTG overnight is demonstrated in Fig. 14. The electrophoresis demonstrates the separation of cellular protein content by molecular weight, visible as bands that can be compared against a protein ladder with known molecular weight. Bands close to 15 kDa and 25 kDa form after IPTG-induced protein expression for *E. coli* strains transformed with Mfp-16 and Mfp-17 pET28 respectively. The theoretical molecular weights for the recombinant versions of Mfp-16 and -17 are 10.8 and 23.9 kDA respectively (including his-tag, linker, and cleavage site). The formation of these bands in *E. coli* culture with IPTG is evidence of IPTG-induced recombinant protein expression as the bands are very close to the expected molecular weight and only formed upon exposure to IPTG, a stable and effective artificial analog of lactose [90].

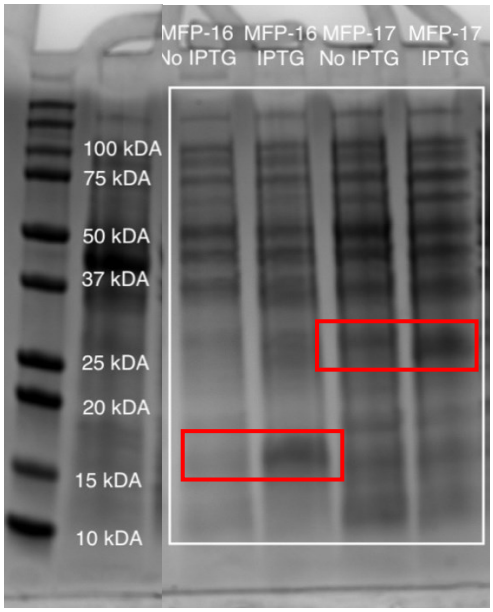

Figure 14. SDS-PAGE of small-scale overnight cell culture sample for transformed PQN4 *E.coli* with and without IPTG (1mM) protein expression induction for Mfp-16 and Mfp-17.

While proteins normally separate to their expected molecular weight, the heavy content of cysteine residues in Mfp-16 and Mfp-17 could explain why there is a drift in their progression through the SDS-PAGE. Cysteine residues are vulnerable to oxidation and adduct formation during the gel separation process due to the reactivity of sulfhydryl groups which can cause the protein to react with the gel matrix and directly affect band mobility [91, 92]. This directly affects the molecular weight estimates, and reduces band resolution and reproducibility [92]. Even though the samples were reduced with beta mercaptoethanol prior to electrophoresis, it remains likely that a level of oxidation occurred during their mobility through the gel as the proteins may themselves act as reducing agents. The interaction of acrylamide and sulfhydryl groups too likely played a role in affecting protein mobility [91]. Comparing Mfp-16 to Mfp-17, Mfp-16 drifted further than Mfp-17 from their expected molecular weight (~5 kDa vs ~1-2 kDa respectively) which could be explained by Mfp-16's greater cysteine content (16 mol%) than Mfp-17 (7 mol%).

The identity of recombinantly-expressed Mfp-16 and Mfp-17 was verified by performing western blot on the same samples as for Fig. 14, demonstrated in Fig. 15. The antibody used was HRP-tagged anti-His-tag, which specifically targeted the his-tag found in the recombinantly produced cysteine-rich Mfps with the genetically engineered pET28 plasmid. Protein containing an accessible his-tag would be located by the antibody and be displayed via induced

chemiluminescence by the HRP tag. Samples with protein expression induced with IPTG demonstrated antibody blot signal while samples without IPTG did not. This meant that genetically engineered *E. coli* was not successful in expressing cysteine-rich Mfp-16 and -17 without exposure to IPTG. Thus, the *lac* operon in the pET28 vectors was effective in controlling recombinant protein expression [90]. Moreover, the western blot results were definite proof that the protein expression of Mfp-16 and Mfp-17 in *E. coli* was successful.

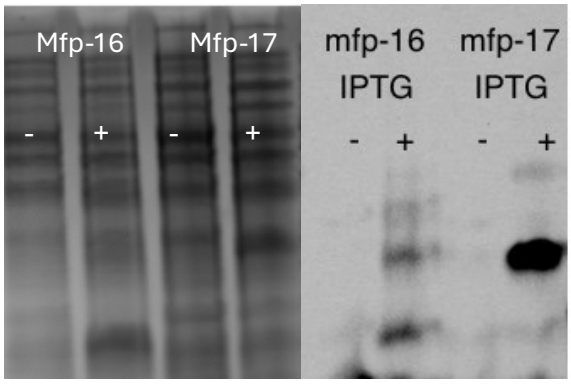

Figure 15. Identification of Mfp-16 and Mfp-17 with anti-his-tag antibodies by western blot. A) SDS-PAGE of small-scale overnight cell culture sample of transformed PQN4 *E. coli* with (+) and without (-) IPTG (1mM) protein expression induction for Mfp-16 and Mfp-17. B) Western blot of the same samples as in A) with anti-his-tag HRP-tagged antibodies.

5.3 Immobilized Metal Affinity Chromatography (IMAC) Purification of Cysteine-rich Cuticle Mfps

After the expression of recombinant Mfp-16 and -17 was verified, the proteins were individually purified via immobilized metal affinity chromatography (IMAC) with Ni^{2+}-loaded nitrilotriacetic acid (NTA) agarose resin. This is a robust system that is very effective for the isolation of his-tagged recombinant proteins [93]. The fractions collected by this process are examined by SDS-PAGE in Fig. 16 & 17 for Mfp-16 and Mfp-17 respectively. The separation of the recombinant cysteine-rich cuticle Mfps from the bulk of the *E. coli* protein lysate is evident by comparing the content of the elution fractions to the flowthrough and wash fractions. The formation of bands near 15 kDa and 25 kDa for Mfp-16 and -17 in the elution fractions was expected based on previous results (Fig. 14) since it is close to the theoretical molecular weight of the recombinant proteins. As such, it is evident that the addition of a his-tag and linker sequence to the protein sequences

worked as expected to isolate the proteins to a purity from which further characterization could be done.

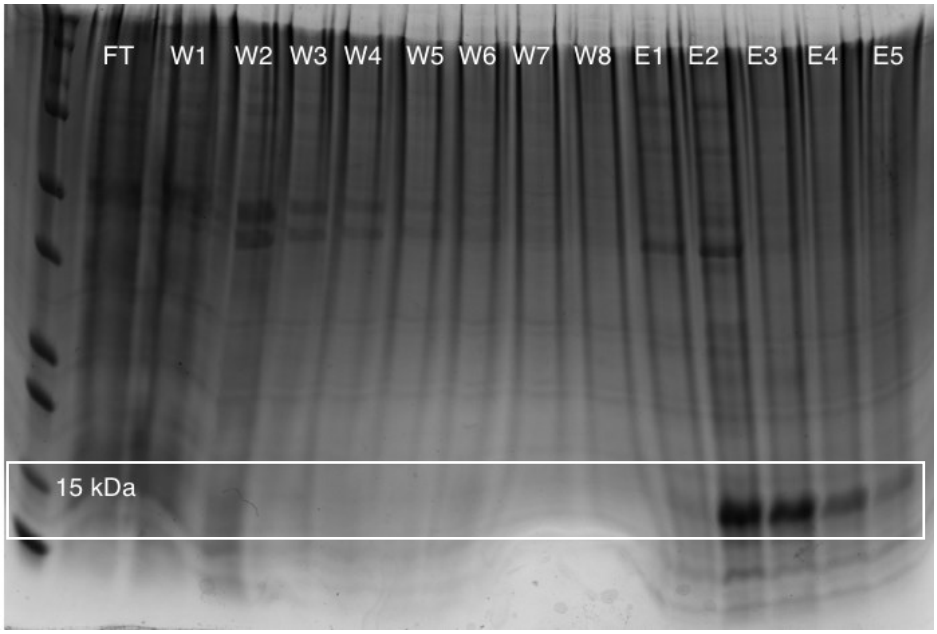

Figure 16. SDS-PAGE examination of fractions collected from IMAC with recombinant Mfp-16 cell lysate from beginning to end (FT: flowthrough, W: wash, and E: elution) demonstrates the isolation of the Mfp-16 from *E. coli* lysate proteins.

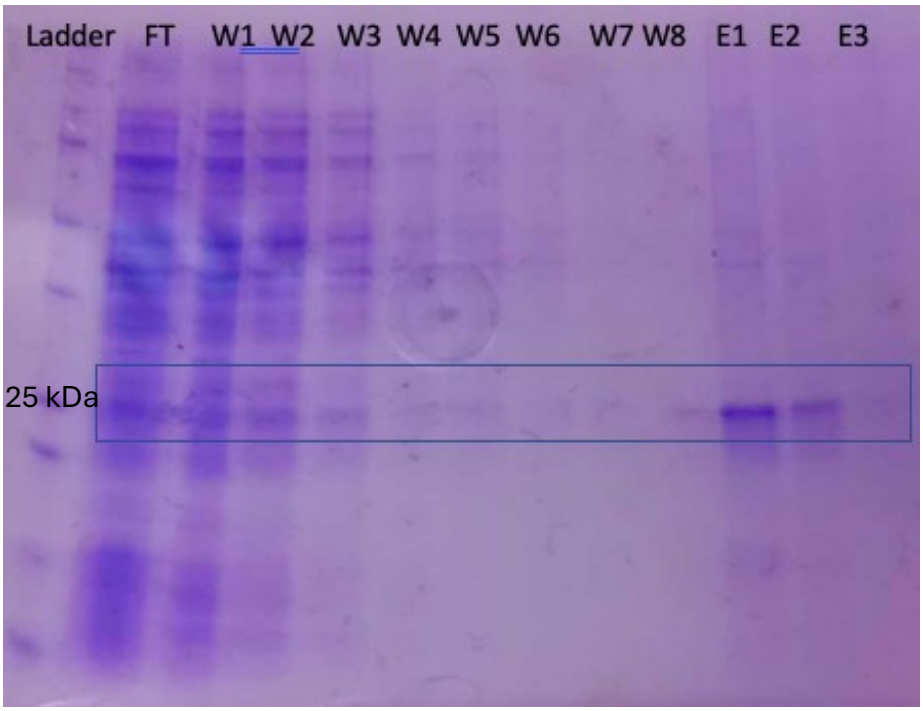

Figure 17. SDS-PAGE examination of fractions collected from IMAC with recombinant Mfp-17 cell lysate from beginning to end (FT: flowthrough, W: wash, and E: elution) demonstrates the isolation of the Mfp-17 from *E. coli* lysate proteins.

5.3 Cysteine-Rich Cuticle Mfps are Robust Reducing-Agents

Control of redox environment is purported to be an important function of the cuticle's cysteine-rich Mfps, as this function is necessary to maintain and rescue Mfp-1's metal binding catechol functional groups from exposure to the oxidative seawater environment [30]. However, no studies have reported the biochemical redox properties of these proteins so far despite indirect evidence that cysteine functional groups originating from the byssal thread's surface are reactive. If the byssal thread's cysteine thiol functional groups are covalently modified to render them unable to react, a near total elimination of the thread's reducing stance is the result, making it clear that cysteine residues are the primary agents responsible for managing redox conditions by a significant margin [48]. Furthermore, investigations on Mfp-6, a very closely related cysteine-rich Mfp from the byssal plaque, were successful in demonstrating that cysteine-rich Mfps are efficient antioxidants when naturally extracted or recombinantly expressed [32, 68, 94]. This work set a backdrop of evidence that points to cysteine-rich Mfps working as reducing agents that enable or enhance the function of nearby catechol-rich Mfps potentially across the byssal thread's

components. Moreover, the work on Mfp-6 also established methods to examine capacity for reducing activity for similar proteins in the future. In particular, the DPPH and Ellman's assay were effectively used to assess the protein's reducing capability and ascertain the degree of cysteine reactivity respectively [32, 67]. These assays were excellent as a starting point in the characterization of Mfp-16 and Mfp-17 because they probe the expected biochemical properties based on their enrichment in cysteine residues.

The Ellman's assay is an efficient technique to assess the reactivity of protein sulfhydryls (-SH) as it scrutinizes the tendency of a protein's cysteine residues to reduce and cleave DTNB's (5,5′-dithio-bis(2-nitrobenzoic acid)) disulfide bond (Fig. 18, A) [88]. The reactivity of Mfp-17's thiol groups were examined through this assay and the results displayed a robust performance (Fig. 18). With increasing protein concentration (0 to 40 μm) the solution's absorbance at 412 nm increased linearly as expected (Fig. 18, B,C) signalling the reduction of DTNB by Mfp-17's cysteine residues. The mass of -SH (nmolSH) participating in the reaction was calculated following the beer-lambert law formula using a molar absorptivity coefficient of 14,000 $M^{-1}cm^{-1}$ from the light absorbance at 412 nm produced by the TNB^{2-} anion generation. The selection of the molar absorptivity coefficient was based on the addition of 2% SDS to the reaction buffer which modulates the coefficient as do other buffer additives like detergents or denaturants [88, 95, 96]. The linear correlation between Mfp-17 concentration and absorbance corresponds to the assay's performance in measuring the protein's sulfhydryl reactivity across increasing concentration. It was expected that an equivalent increase in absorbance would match the increase in protein concentration at this concentration range based on the standardized assay performance of reacting -SH mass (nmolSH) [88]. In a related note, the increase of DTNB breakdown is macroscopically visible by the evolution of a strong yellow colour as Mfp-17 concentration increases in the sample solution (Fig. 18, E).

The precipitation of the protein was observed as it was introduced into the buffered reaction solution at pH 8 that is very close to that of seawater (~8.2). As the protein transitioned from acidic storage conditions (pH 3.5) into a slightly basic pH, the protein evolves from a liquid solution towards a solid-state material. This pH-triggered transition is especially interesting considering its expected role the byssal thread's cuticle, which calls upon its proteins transitioning from liquid

precursors in acidic storage vesicles into the solid thread when exposed to basic seawater [25]. Like Mfp-1 and Mfp-6, Mfp-17 also demonstrates this pH-triggered transition phenomena [94, 97]. The fluid to solid transition is so strong that even the inclusion of 2% SDS in the reaction buffer did not prevent protein precipitation despite the high concentration and strength of SDS in solubilizing proteins. Even so, the precipitate remained entirely capable of reducing DTNB in its aqueous vicinity while in a solid state (Fig. 18, F).

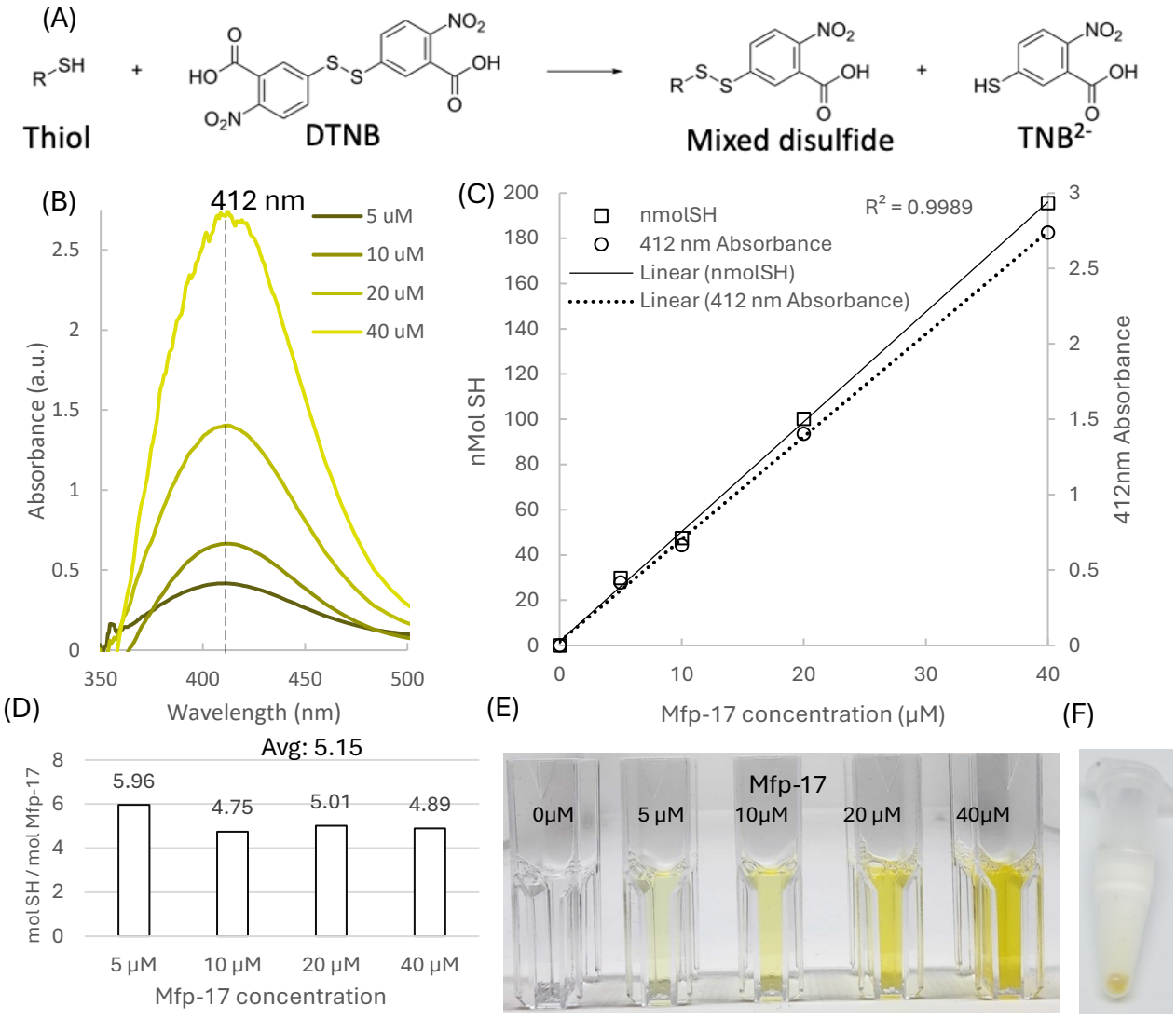

Figure 18. Mfp-17's cysteine residues demonstrate reactive thiolate properties by the evolution of an absorbance peak at 412 nm due to the breakdown of DTNB into yellow TNB^{2-} anions in Ellman's assay. **A)** Chemical reaction of a reducing thiol functional group and DTNB to form a mixed disulfide and TNB^{2-}. **B)** Light absorbance peak (412nm) formed by the reaction of Mfp-17 and DTNB in pH 8 buffer (0.1M Na_2PO_4, 2% SDS, 0.5 mM EDTA). **C)** Ellman's assay standard

curve of 412nm absorbance and Mfp-17 concentration with calculated values of nmol SH reacted **D)** Calculation of reacting sulfhydryl per protein molecule with increasing Mfp-17 concentration. **E)** Yellow colour evolution with increasing sample protein concentration due to increased TNB anion formation. **F)** Mfp-17 precipitate under neutral pH reacted with DTNB displays reducing properties evident from yellow colour produced by DTNB reduction

In further analysis, the mass of reacting -SH was cross-examined with the mass of Mfp-17 as the denominator (Fig.18, D) to calculate the empirical number of cysteine residues that participated in the reaction per protein molecule. The results demonstrate that out of the theoretical 13 cysteine residues that could be available for reaction in Mfp-17 [47], only about 5 appear to participate in the reduction of DTNB as the average ratio of -SH that participated per a single protein molecule is 5.15. It is noteworthy to mention that the reaction pH is a denominator of -SH reactivity due to the acidic nature of the thiol functional group, which allows it to thermodynamically disassociate into its negatively-charged thiolate $-S^-$ form depending on the pKa of the protein's cysteine residues and the solution pH [98, 99]. However, the pKa of cysteine residues in proteins is a complicated subject when compared to free cysteine amino acid, whose pKa is ~8.3-8.4 [98-100]. Cysteine pKa is widely modulated due to the solvent, steric and electrostatic environment of proteins which can range in magnitude of 3 to 11, becoming significantly more acidic or basic depending on the aforementioned factors [99, 101]. In fact, proximity of positively charged residues to cysteine residues is associated with decreasing the pKa of the thiol [100, 101], and inversely, negative charged residues can increase cysteine pKa [98]. This effect occurs due to effects from electrostatic interactions as positive charges can stabilize the ionization of the thiol into a thiolate, while negative charges would behave in an opposite manner and instead support the neutral thiol [98]. Integrating this information in the context of understanding Mfp-17's cysteine reactivity, it suggests that only ~40% of its cysteine undergoes reactive reducing behaviour based on the ratio of reacted -SH/protein unit (5.15) to the theoretical cysteine content (13). If the proximity of cysteine residues to arginine or lysine is examined in Mfp-17's primary sequence (Fig. 4), 8 of 13 cysteine residues are located within 2 amino acids to a positively charged amino acid in Mfp-17's primary sequence. This would suggest that perhaps more than 60% of Mfp-17's should be reactive at pH 8 (pH of Ellman's assay reaction), because it is probable that at least 8 cysteine residues in Mfp-17 could have a pKa lower than 8 derived from their proximity to positive charges and thus shift their tendency to be in a reactively charged thiolate stance at this pH.

Moreover, the argument that the reducing behaviour at this pH would be close to optimal makes sense from its proximity to that of seawater, where the strongest reducing power would be required from the protein. From this perspective, the measured thiol reactivity of Mfp-17 is less than it would be expected since less than half of the cysteine residues are apparently reactive in Ellman's assay. Yet perhaps the arrangement and function contribution of Mfp-17's cysteines are diverse and work beyond providing reducing properties alone. Cysteine residues can also function in crucial catalytic, structural, and metal-coordinating roles [99], with pivotal roles in protein function despite an abundance that is strikingly low, but with the highest evolutionary sequence conservation compared to all other amino acids [99, 102, 103]. Given the aforementioned propensity of the byssal cuticle to bind iron in the matrix [25, 48] and to transition into a solid-state material, the lower levels of cysteine reactivity in the Ellman's assay near the pH of seawater where the reducing behaviour should be optimal suggest that Mfp-17 does not solely work to provide a reducing environment alone but alternatively the cysteine residues may be functioning to coordinate with iron ions (as suggested in an earlier work [25]), and to control protein structure in order to facilitate the pH-triggered transition from liquid to a solid material as expected from a major protein component of the byssal thread's cuticle matrix.

Ellman's assay is only viable in a pH range close to neutral or slightly alkaline (7.4-8.0) [88, 95] due to the low pKa (~4.5) of the TNB anion after DTNB reduction [104]. This means that as the solution becomes more acidic, TNB will not entirely be deprotonated into its ionized form and as a result, the assay's light absorbance signal would become increasingly dependent on pH rather than reducing agent activity if the reaction acidity is closer to the pKa. In turn, this becomes a significant limitation of the assay when it is desired to understand a protein's cysteine reactivity at alternative pH levels. It is expected that the reducing capability of the cuticle's cysteine-rich Mfps would change depending on pH given that cysteine reactivity is dominated by its pKa. To overcome this limitation, an alternative assay capable of probing for antioxidant properties at difference pH was required.

Thus, the DPPH assay was applied to further explore the reducing capabilities of Mfp-17 and Mfp-16 across different pH levels based on the assay's known reactivity with reducing thiol functional groups [105], and previous applications in ascertaining the antioxidant properties of Mfp-6 [94].

An optimized method focused on keeping proteins and DPPH soluble at the same time despite methanol exposure was executed [67]. Consistent with the pattern observed in Mfp-6's DPPH assay performance, Mfp-16 and -17 also demonstrated precipitation at pH 5 and 7, but not at pH 3 where they also remained soluble [94]. As a result, their reducing properties were examined under soluble acidic conditions where they demonstrated a strong ability to reduce the DPPH radical even under considerably acidic conditions (Fig. 19). This was visible by the time-dependent bleaching of the solution's violet colour and decreasing absorbance of the peak centered around 515 nm, which is associated to the elimination of DPPH's stable radical by a reducing agent (Fig.19).

Moreover, the argument that the reducing behaviour at this pH would be close to optimal makes sense from its proximity to that of seawater, where the strongest reducing power would be required from the protein. From this perspective, the measured thiol reactivity of Mfp-17 is less than it would be expected since less than half of the cysteine residues are apparently reactive in Ellman's assay. Yet perhaps the arrangement and function contribution of Mfp-17's cysteines are diverse and work beyond providing reducing properties alone. Cysteine residues can also function in crucial catalytic, structural, and metal-coordinating roles [99], with pivotal roles in protein function despite an abundance that is strikingly low, but with the highest evolutionary sequence conservation compared to all other amino acids [99, 102, 103]. Given the aforementioned propensity of the byssal cuticle to bind iron in the matrix [25, 48] and to transition into a solid-state material, the lower levels of cysteine reactivity in the Ellman's assay near the pH of seawater where the reducing behaviour should be optimal suggest that Mfp-17 does not solely work to provide a reducing environment alone but alternatively the cysteine residues may be functioning to coordinate with iron ions (as suggested in an earlier work [25]), and to control protein structure in order to facilitate the pH-triggered transition from liquid to a solid material as expected from a major protein component of the byssal thread's cuticle matrix.

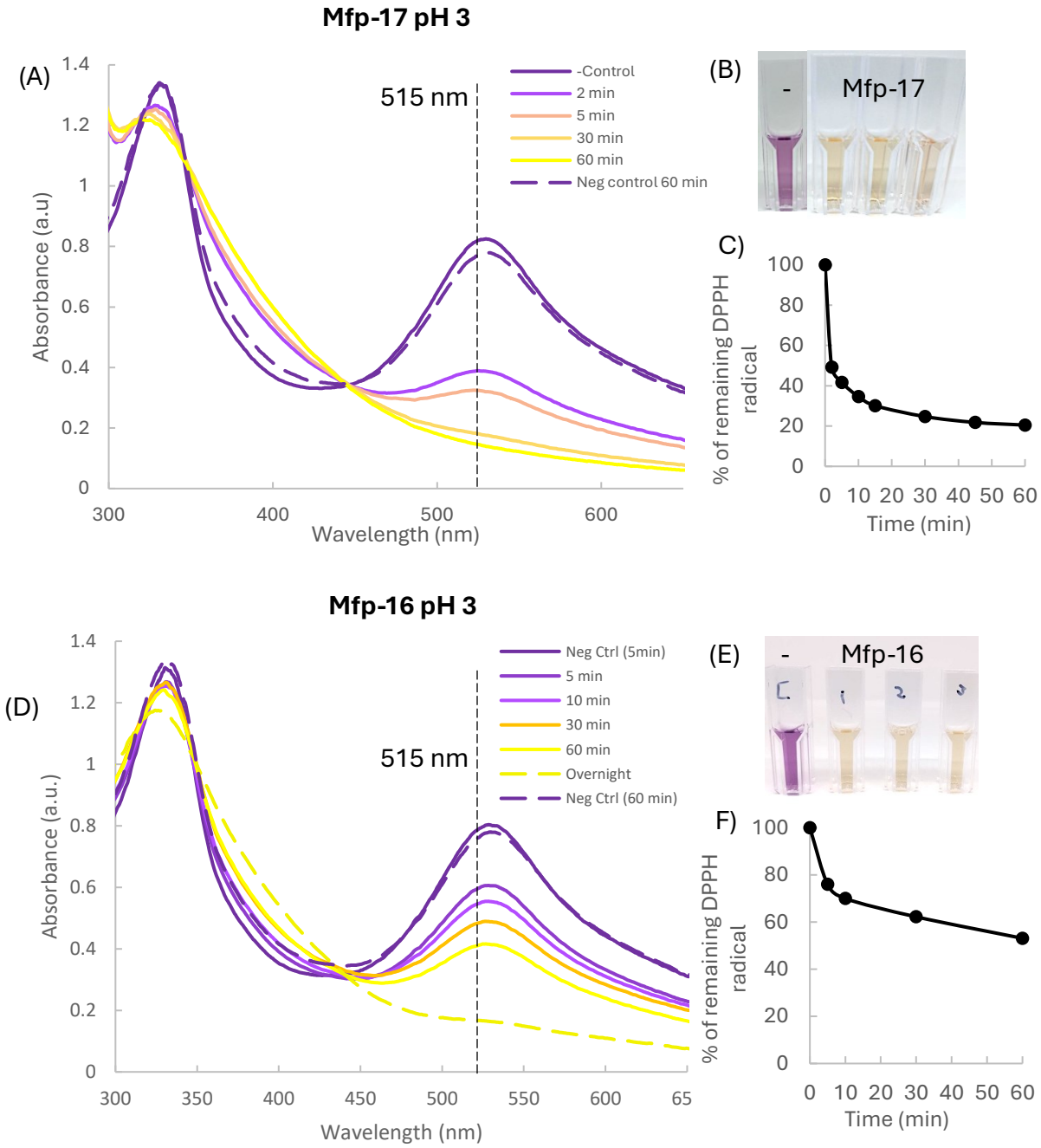

Figure 19. DPPH assay at pH 3 with ~0.4 mg/mL (17 µM) Mfp-16 and -17 in 0.1 M phosphate-citrate buffer + 0.3%v/v Triton X-100 and 100 µM DPPH with reduction of absorbance at 515 nm due to protein antioxidant properties. A) UV-Vis light absorbance spectral changes over 1 hr from breakdown of DPPH radical due to Mfp-17 reduction. B) DPPH + Mfp-17 triplicate samples become yellow colour after 5 min due to the reduction of DPPH radical. C) Mfp-17's elimination of DPPH radical over 60 min. D) UV-Vis light absorbance spectral changes over 1 hr from breakdown of DPPH radical due to Mfp-16 reduction. E) DPPH + Mfp-16 yellow sample colour due to reduction of radical in comparison to a purple negative control after 60 min reaction. F) Mfp-16's elimination of DPPH radical over 60 min.

Through comparison of DPPH reduction of Mfp-16 and Mfp-17, unexpected information was revealed that explains the reaction kinetic differences between the two proteins. Within the time frame of the experiment (60 min), Mfp-17 reduces DPPH at an extremely quick rate with nearly 50% elimination of the DPPH radical after only 2 minutes and proceeding to plateau at close to 20% after 60 min when the reaction is closer to a steady-state (Fig.19, C), demonstrating a reducing behaviour that is very close to that of mussel-extracted Mfp-6 at near equivalent concentrations (~15 uM) [94]. This performance has been fitted previously with a double exponential decay curve model. On the other hand, Mfp-16's performance was less extensive with only ~25% of DPPH radical elimination after 5 min and a seemingly linear elimination of DPPH with increasing time (Fig. 19, F), which if given sufficient time it can reduce DPPH to a degree comparable to Mfp-17 (Fig. 19, D). Mfp-16's performance more closely resembles that of recombinantly produced Mfp-6, which displays the lack of a fast initial decay and lower final levels of DPPH reduction after 60 min that are attributed to the additional presence of DOPA in mussel Mfp-6 [68, 94] . It is evident that reducing properties amongst the cuticle cysteine-rich Mfps is not equal despite a near equal number of cysteine residues between Mfp-16 (12) and Mfp-17 (13), which means that redox performance is not controlled solely by the number of cysteine residues in the proteins, and likely internal differences are producing two separate proteins with different performance. The acidic conditions do challenge the efficiency of cysteine thiolate redox, and close examination of Mfp-16's proximity of its cysteines to lysine or arginine does reveal less cysteine is nearby positive charges than Mfp-17 at least on a primary sequence-based perspective (Fig. 4). This can translate to increased cysteine pKa and thus lesser thiolate reactivity at more acidic pH, but perhaps increasing action at seawater levels.

Additionally, there can be influences coming from other potential electron-donating amino acids like tyrosine [68, 106]. Tyrosine (tyr) and tryptophan (trp) both can also be involved in managing redox reactions [107]. With 16 tyr and 8 trp residues, the reducing behaviour of Mfp-17's cysteine could be influenced towards an increasingly reductive poise. This concept is challenged by the decreased deprotonation of tyr and trp in acidic pH [108], but the interaction of tyrosine and cysteine can be assisted by protein structure [109]. While the mechanism behind Mfp-17's robust reducing ability at acidic pH may not be entirely understood at this point, nonetheless it is impressive that the recombinantly-produced protein achieved nearly the same DPPH assay

performance as that of mussel-extracted Mfp-6 which is considered to take advantage of both, cysteine and DOPA residues in its reducing activity [94]. Taken together, Mfp-16 and Mfp-17 are effective reducing agents that form a dynamic redox system that is active even under acidic conditions as it would be expected from their suspected role as matrix components working to maintain the catechol functional groups of Mfp-1 in a reduced state, sustaining DOPA-metal coordination in the cuticle.

5.4 Mfp-17 Binds Iron Ions in Acidic Aqueous Environments

5.4.1 UV-Vis Spectroscopy

Cysteine-rich cuticle Mfps are hypothesized to be capable iron binding agents evidenced by the colocalization of cysteine and iron in the byssal thread's cuticle matrix [25], and the lower levels of DOPA metal coordination in the matrix compared to the granules [16]. However, there is not yet any evidence of Fe-Cys bonds in the cuticle across literature despite previous suggestions [25] and so finding evidence of Fe-S bonds in the isolated cysteine-rich Mfps would be the first example reported. The lack of literature to examine in this regard made it a significant challenge to begin examining how Mfp-16 and Mfp-17 could be involved in this process and to develop an effective methodology for acquiring this information. To meet this challenge, finding examples of iron-binding cystine-rich proteins in literature was effective to gain a foothold in the methods and behaviour from relevant proteins that could potentially be similar to Mfp-16 and -17. The options were numerous due to the widespread applications that iron ions have in proteins with numerous imperative roles in enzymes, cellular respiration, and redox control to name a few [110]. By comparing protein sequence similarities, metallothionein's were the most similar and promising class of iron-binding proteins because of their sole use of cysteine as the coordinating ligand [76]. Like Mfp-16 and Mfp-17, metallothioneins (MTs) too have a relatively short amino acid sequence and significant cysteine composition, which are used to coordinate different transition and heavy metals like zinc, copper, and cadmium [111]. Given the parallels, there was a notion that Mfp-16 and -17 would demonstrate analogous activity to MTs and thus, the same techniques used to characterize MTs could be effective in characterizing iron-cysteine coordination in Mfp-16 and -17.

Electronic absorbance in the UV-vis region caused by ligand-to-metal charge-transfer (LMCT) bands formed by metal-cysteine thiolate coordination has been the foremost method to characterize MTs [72]. UV-Vis light absorbance spectroscopy of protein solutions with and without metals is effective in capturing this signal. Experimentation began with Mfp-16 because of its closer resemblance to MTs than Mfp-17, however, significant differences were noticeable from the start. MTs demonstrate a breakdown of their cysteine-metal coordination in acidic pH, which is taken advantage to generate metal-free apoMT [112]. In these experiments, apoMT was combined with a metal species and the pH of the solution increased to > pH 8.0 to support the generation of cysteine thiolate-metal coordination [113]. This attribute is examined by pH titrations to examine the coordination process of the metal depending on the decreasing acidity of a solution by MTs [114]. Mimicking this method using Mfp-16 and iron ions was not successful due to the observed propensity for both the protein and iron salts to precipitate upon transitioning from pH 3 to pH 8. Mfp-16's precipitation propensity was not unexpected because that is its natural behaviour in the cuticle. At this point it became clear that Mfp-16's behaviour was distinct from MTs, and it would be increasingly challenging to understand how it could interact- with iron due to their simultaneous precipitation. As a result, focus shifted towards Mfp-17 which was more promising because of its stronger reducing activity in acidic pH and potential to have free cysteines for metal-coordination (Fig. 18, 19). In the same way as Mfp-16, Mfp-17 also transitioned into a solid material by a pH-triggered transition from acidic to neutral conditions, but this time the interaction between the protein and iron ions was examined at acidic pH instead. Under this condition, both Mfp-17 and the iron ions could remain soluble and facilitated light absorbance examinations.

To assess the interactions between Mfp-17 and iron ions, the UV-vis light absorbance of the reaction between them were measured by blanking against the buffer solution with an equal level of iron ions such that only the contributions of Mfp-17 due to increasing iron concentration were measured. Protein solutions were titrated with increasing iron (II) acetate concentrations in sodium acetate buffer at pH 3.6 that was purged with nitrogen gas and without purging (normal air conditions) to find signatures of protein-iron binding and examine if dissolved oxygen from air played a role in binding (Fig. 20). Oxygen exposure can influence the formation of thiolate-iron bonds in MTs [76], therefore it was deemed necessary to understand if oxygen influenced Mfp-17's iron binding capabilities. Unlike MTs which lack aromatic residues [72], Mfp-17 posed the

challenge of already having high light absorbance due to its significant aromatic residue composition which broadly absorb light at 280 nm (tyr, trp), and could have interfered with weaker signatures from iron binding since due to overlaps at relevant UV light wavelengths.

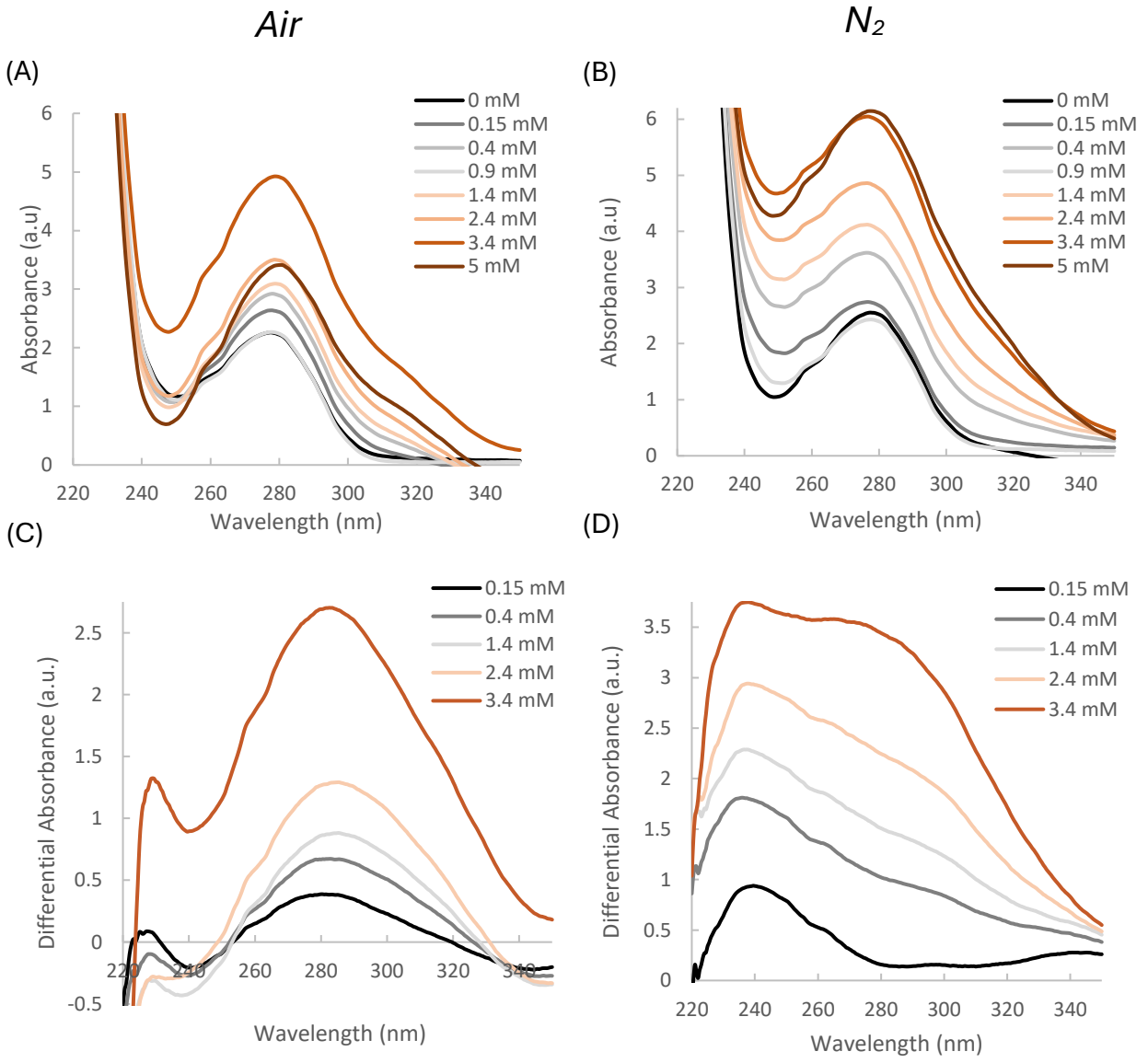

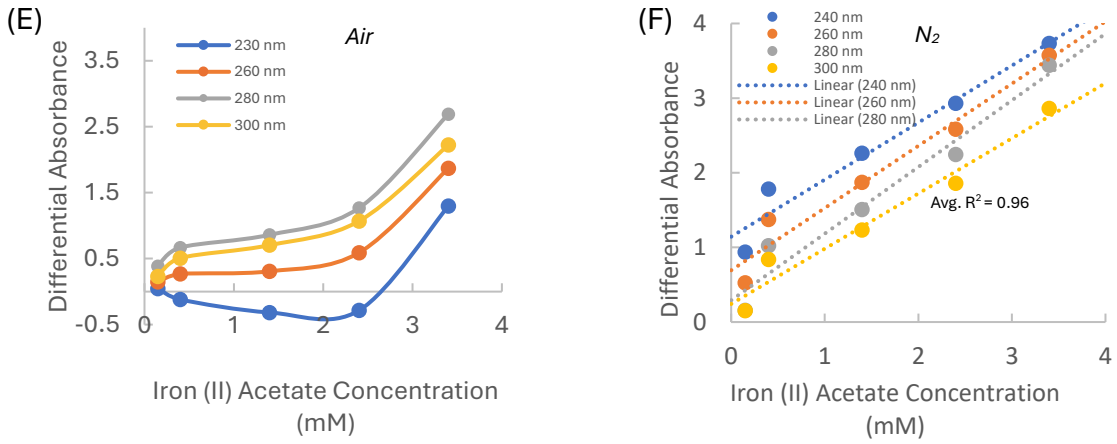

Figure 20. UV-Vis light absorbance spectra of Mfp-17 (30µM) titrated with increasing iron (II) acetate concentration in 100 mM sodium acetate pH 3.6 buffer. A, B) Mfp-17 absorbance comparison between in N_2 purged and non-purged conditions. C, D) Differential spectra between N_2 purged and non-purged conditions. E, F) Plots of light absorbance at different wavelengths as a function of iron (II) acetate concentration between N_2 purged and non-purged conditions.

The spectra of increasing iron (II) concentration in the presence of Mfp-17 displays an increase in absorbance across the mid-to-high UV light range spectrum from 220 nm to 350 nm (Fig. 20, A, B) with notable differences in absorbance when comparing between N_2 purged reaction and not. The differential spectra were calculated by subtracting the baseline protein absorbance without iron from the spectra with increasing iron concentrations for both conditions (Fig.20 C, D). These spectra are useful to provide information on the contribution of the last titrating agent added [72], in this case highlighting the interactions between Fe^{2+} with Mfp-17 because iron ions were the titrating agent whose interaction with the acetate buffer was eliminated by blanking against conditioned (air/N_2) buffer with an equal iron concentration. The nitrogen purged spectra demonstrates a broad increase in absorbance with a noticeable peak centered close to 240 and a broad shoulder centered around 300 nm (Fig. 20, C) compared to strong peaks at ~230 and ~285 nm and what appears to be broad shoulders at ~255 and ~315 nm for the spectra in normal air conditions (Fig. 20, D). The change in absorbance is further examined by the plotting iron concentration and corresponding differential absorbance at separate light wavelengths (Fig. 20, E, F) that demonstrate a strong linear relationship in the nitrogen purged reaction (F, avg R^2: 0.96) and what may be a more exponential relationship for the reaction in air (E).

Under these reaction conditions it was observed that the maximum absorbance level was reached at an iron ion concentration of 3.4 mM, which subsequently decreased when concentration

increased to 5 mM (Fig. 20, A, B). This loss in absorbance is attributed to the saturation of Mfp-17's binding to Fe^{2+} ions alongside the minor dilution of the reaction from the addition of the concentrated iron solution. MTs similarly demonstrate this behaviour in an aqueous environment when the ratio of protein to metal ions reaches a saturation point at which increasing metal concentration no longer contributes to increasing light absorbance because there are no more protein ligands available to sequester additional ions [76, 114]. Moreover, the Mfp-17:iron ratio may appear very high (30 µM:0.15-5mM), but the effect of the buffer must be considered as acetate anions coordinate iron ions [115], especially at acidic pH due to greater acetate levels which compete with Mfp-17 due to the relative high concentration of the buffer (100 mM). Therefore, it was not yet possible to determine how many iron ions interact per Mfp-17 molecule like it has been achieved for diverse MTs [75, 76, 112, 114, 116]. However, unlike MTs whose binding at pH 3.6 is severely diminished [114, 116], Mfp-17's binding had to be examined under acidic conditions because of its nature to precipitate at pH 7-8 where otherwise MTs binding-would be effective. This challenge was difficult to overcome since the reaction solution had to be buffered in an acidic pH, and acidic buffers like acetate and citrate will solubilize and coordinate iron ions [115, 117].

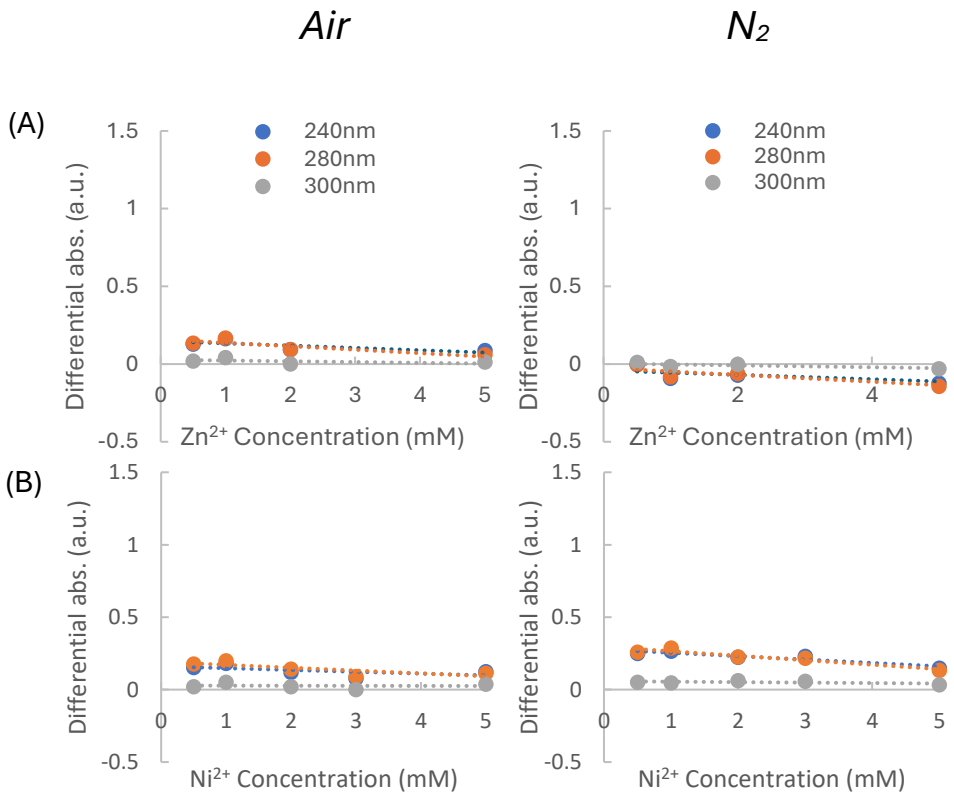

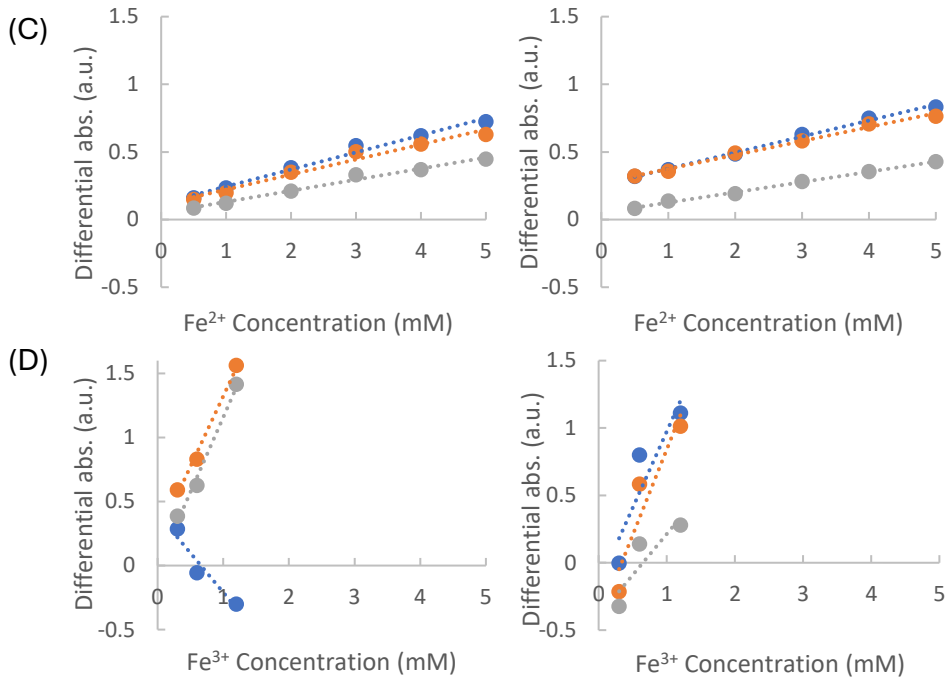

Figure 21. Plots of differential light absorbance at different wavelengths as a function of concentration for multiple transition metals and different iron salts between N_2 purged and non-purged air conditions. A) Zinc Acetate. B) $NiCl_2$. C) $FeCl_2$ D) $FeCl_3$

The promiscuity of Mfp-17's metal binding was analyzed by comparing the same reaction with different transition metal ions including Ni^{2+} and Zn^{2+} which were not expected to react at all or at very weakly at most, as well different Fe^{2+} and Fe^{3+} chloride salts (Fig. 21). Stark differences in light absorbance were noticeable between Mfp-17's reactivity to alternate transition metals and iron. Instead of increasing absorbance, Zn^{2+} and Ni^{2+} ions caused a decrease of absorbance across all light wavelengths (Fig. 21, A, B) with increasing metal ion concentration. In contrast, at the same concentrations, Fe^{2+} and Fe^{3+} ions demonstrated a linear increase in absorbance across most wavelengths (Fig. 21, C, D). Comparing between Fe^{2+} and Fe^{3+}, the difference in response was drastic with the ferric ions producing much higher increases in absorbance at lower concentrations. Moreover, the differences between N_2 purged and air conditions were only noticeable for ferric ions as well, as absorbance decreased at 240 nm in air while in nitrogen it increased like the rest of the wavelengths. Integrating these results, it is increasingly evident that Mfp-17's reactivity towards metal ions is narrow with specific preference towards iron ions, unlike MTs which are promiscuous and struggle to bind with iron [72, 76, 77]. Unexpectedly, the source of iron ions in

the vicinity may influence how capable Mfp-17 is able to sense and bind iron due to the notable difference in absorption between iron (II) acetate and $FeCl_2$, which in its acetate-coordinated form its interaction appears to be better suited to coordinate with Mfp-17 given the larger absorbance differentials at all light wavelength, and also seems to be influenced by oxygen exposure unlike $FeCl_2$ which did not display any difference between the purged and air conditions. Furthermore, the significant jump in absorbance at lower relative Fe^{3+} concentrations suggest a binding preference over Fe^{2+} ions which may be true between chloride salts but comparing $FeCl_3$ absorbance to iron (II) acetate in nitrogen-purged conditions it is nearly equal. This may mean that the source of iron ion coordination may be more relevant than its oxidation state for this sort of binding at acidic pH. It could also be that Mfp-17 may possess a flexible mechanism for managing iron oxidation state, a feature which is not uncommon in iron-binding proteins [118].

The increase in absorbance is evidence of iron binding that is most likely being produced from broad LMCT bands between Mfp-17's residues acting as ligands to iron ions. In the case of iron (II)-substituted MTs, they display broad absorbance peak signals in the range of 250-400 nm with peak at ~315 nm and a shoulder at ~340 nm attributed to Fe-thiolate centers [76, 78-80]. While not exactly as iron (II)-MT, Mfp-17's light absorbance signatures do overlap in the ranges that are characteristic of Fe-Cysteine thiolate coordination even at such acidic pH. To gain insight into the role of Mfp-17's cysteine residues in iron coordination, different reaction conditions were organized to probe if cysteine indeed was solely responsible or involved in the coordination of iron as suspected. The acetate buffer concentration was decreased drastically to 5 mM to diminish iron-acetate binding and TCEP, a protein disulfide-specific reducing agent was incorporated to examine if reduced cysteines improved iron coordination. It was expected that TCEP could improve iron binding by reducing Mfp-17's cysteines and maintain them in an open thiol conformation that would be better suited for iron-coordination. Dramatically, the opposite was observed with a complete loss of iron-binding under reducing conditions (Fig. 22 A, B) which is noticeable by the decrease in absorbance when iron (II) acetate is added opposed to the increase in absorbance in reaction conditions without TCEP. This finding suggests that structural disulfide-bond formations may be critical to facilitate Mfp-17's iron binding at acidic pH, which is evident by the complete loss of absorbance gain in reaction conditions under 10x excess of TCEP to Mfp-17. Comparing the differential spectra of the two conditions, absorbance is lost in the TCEP-positive reaction

likely from dilution stemming from adding the iron solution, while a peak at 260 nm with a broad shoulder at ~300 nm forms in the reaction without TCEP (Fig.22, insets). This is evidence that not all cysteine residues in Mfp-17 are involved in metal coordination, otherwise iron binding would have remained unchanged or improved. Instead, unlike MTs which are unstructured [72], there is significant potential that structural disulfide bonds support the folding of the protein into a conformation necessary to execute iron coordination. Circular dichroism data measured in the same conditions as the UV-Vis experiments shows that Mfp-17 does form secondary structures, being strongly alpha-helical at pH 3.6 (data not shown). This may not be surprising given the radical nature of binding iron at acidic pH due to the increasing extent of protonation of a protein's ligands like cysteine which would decrease ligand nucleophilicity [114]. It is understood that Mfp-17 does display the ability to deprotonate its cysteine residues at a low pH from its strong reducing performance at acidic pH (Fig. 19), which may also be critical for iron-binding as deprotonated thiols are indeed more nucleophilic [101]. These results present the idea that disulfide-linked protein folding may be a denominator in supporting Mfp-17's iron binding in otherwise unfavourable acidic pH.

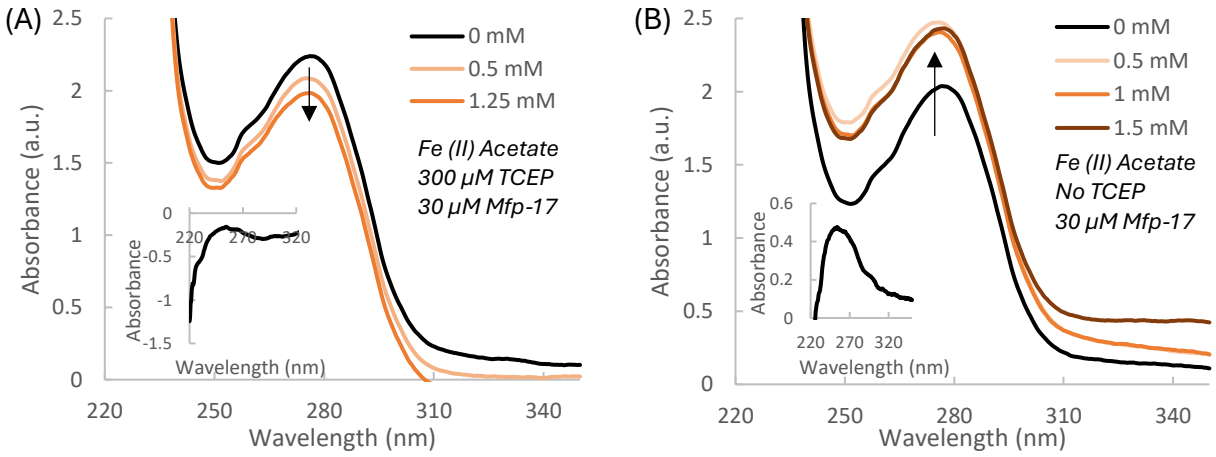

Figure 22. Mfp-17 displays a difference in iron-binding in disulfide-reducing conditions in new buffer (5 mM sodium acetate, pH 3.6) with and without a reducing agent (0.3 mM TCEP) and increasing iron (II) acetate concentrations. A) Absorbance of Mfp-17 (30µM) in pH 3.6 buffer with 0.3 mM TCEP, inset: differential spectra at 1.25 mM iron (II) acetate. B) Absorbance of Mfp-17 (30 µM) in pH 3.6 buffer without TCEP, inset: differential spectra at 1 mM iron (II) acetate

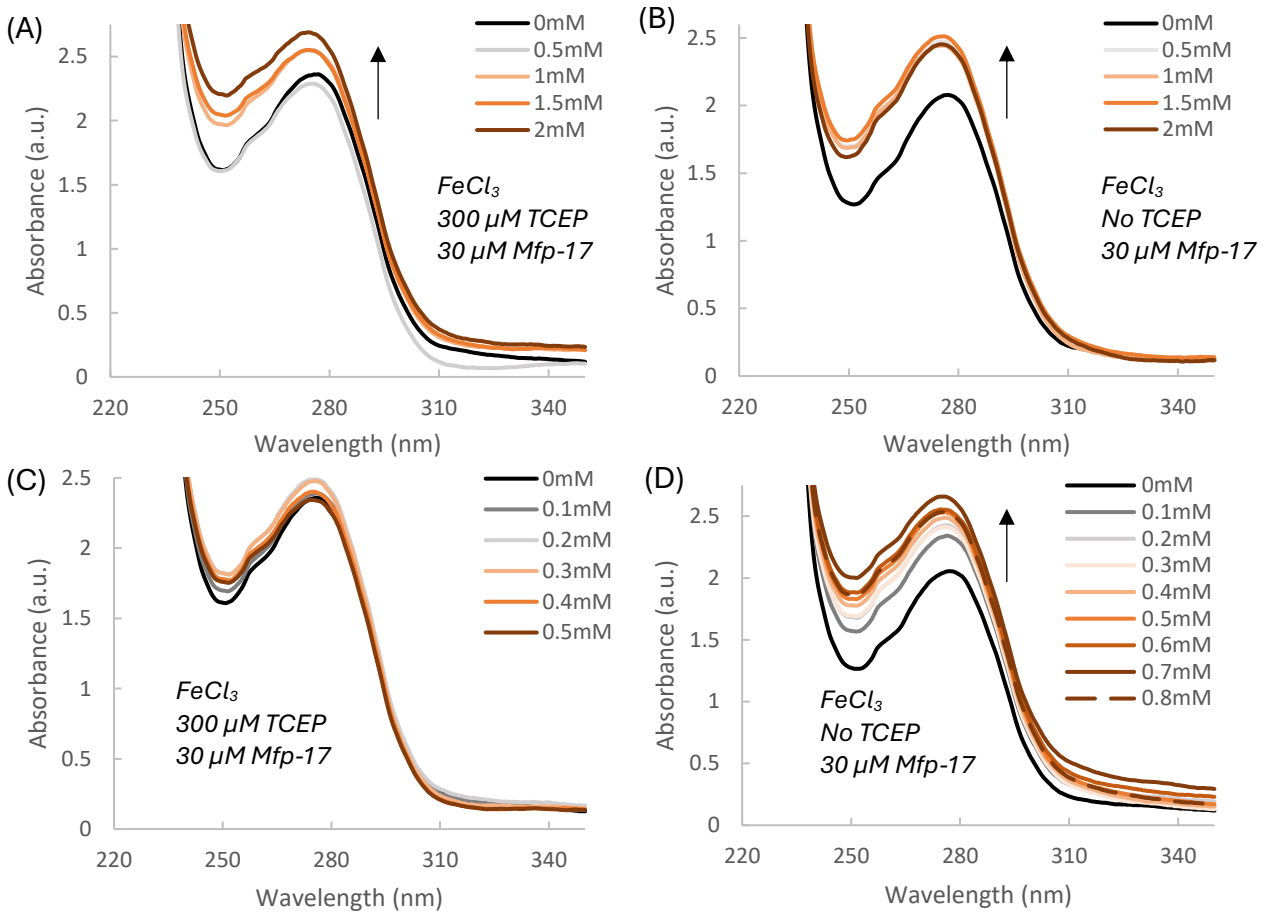

Figure 23. Mfp-17 absorbance difference in new buffer conditions (5 mM sodium acetate, pH 3.6) with and without a reducing agent (0.3 mM TCEP) and increasing $FeCl_3$ concentrations. A, B) Absorbance spectra of Mfp-17 (30µM) with increasing $FeCl_3$ concentration at a rate of 0.5 mM in buffer with TCEP (A) and without TCEP (B). C, D) Absorbance of Mfp-17 with increasing $FeCl_3$ at a rate of 0.1 mM in buffer with TCEP (C) and without TCEP (D).

The effect of reducing agents on Mfp-17's iron binding was examined with ferric ions as well, and the effect of TCEP was not the same as increasing concentrations of Fe^{3+} were able to produce increase in absorbance unlike Fe^{2+} (Fig. 23). Initial lower concentrations of ferric ions seemingly did not make any contributions to absorbance under 0.5 mM (Fig. 23, A, C), while at the same concentration without TCEP, absorbance was already nearly maximized (Fig. 23, B, D) in the same way as Fe^{2+} (Fig. 22, B). This is likely occurring since Fe^{3+} is a stronger oxidizing agent than Fe^{2+} due to its stronger oxidation which perhaps is more reactive towards Mfp-17 and capable of neglecting the reducing behaviour of TCEP at increasing levels of concentrations. This is evident

by the increasing absorbance with increasing levels of Fe^{3+} despite the presence of TCEP (Fig. 23, A). By the same thread, ferric ions may be responsible for inducing disulfide bridge formation in Mfp-17 by oxidizing cysteine in a controlled manner that enables its coordination more suitably. Therefore, this suggests that Mfp-17 may interact preferentially with ferric ions under acidic conditions.

5.4.2 X-ray Photoelectron Spectroscopy

To further confirm the binding of Mfp-17 and iron ions in acidic aqueous environments, X-ray photoelectron spectroscopy (XPS) was used to analyze iron signatures in drop-casted films of dialyzed solutions of Mfp-17 and iron ions. Dialysis was performed in the protein solution to ensure that spectator iron ions were entirely removed from the solution. XPS is a surface technique that examines the composition and chemical state of elements as incident X-ray beams interact and emit electrons according to the atomic orbitals of individual elements [119].

The presence of iron was confirmed in dried films of Mfp-17 reacted with iron (II) acetate whose XPS spectra displayed the formation of Fe2p orbital peaks between 705-735 eV, while the control without iron did not display the peaks as expected (Fig. 24). The Fe2p orbital peaks are a critical signature used to confirm the presence of iron in a sample and to analyze the chemical state of iron [120]. This formation of Fe2p peaks with Mfp-17 despite dialysis signifies the protein sequesters iron ions in acidic conditions, preventing them from being removed during the dialysis process. Dialysis employs large molecular weight pore membranes at ~10kDa which are sufficiently large to easily facilitate the flow of spectator iron ions out of Mfp-17's solution. The success of iron dialysis is demonstrated in Fig. 25A, where the dialysis of a $FeCl_3$ solution without Mfp-17 at equal concentration displays the removal of the salt from solution which is evident by the lack of iron and chlorine element peaks in the spectra. This confirms the dialysis process was successful in removing spectator iron salts from solution, and that any iron signal remaining would be from Mfp-17's iron binding capacity. Indeed, Mfp-17 demonstrates the retention of iron ions when reacted with $FeCl_3$ (Fig. 25B) in a similar manner to previous results with iron (II) acetate. The XPS spectra show the formation of Fe2p peaks without any significant chlorine signal. Therefore, spectating $FeCl_3$ was removed by dialysis while Mfp-17 was able to sequester Fe^{3+} ions from

solution in acidic conditions. Thus, XPS spectra further confirm Mfp-17 binds to both Fe^{2+} and Fe^{3+} in the same conditions examined by UV-Vis measurements.

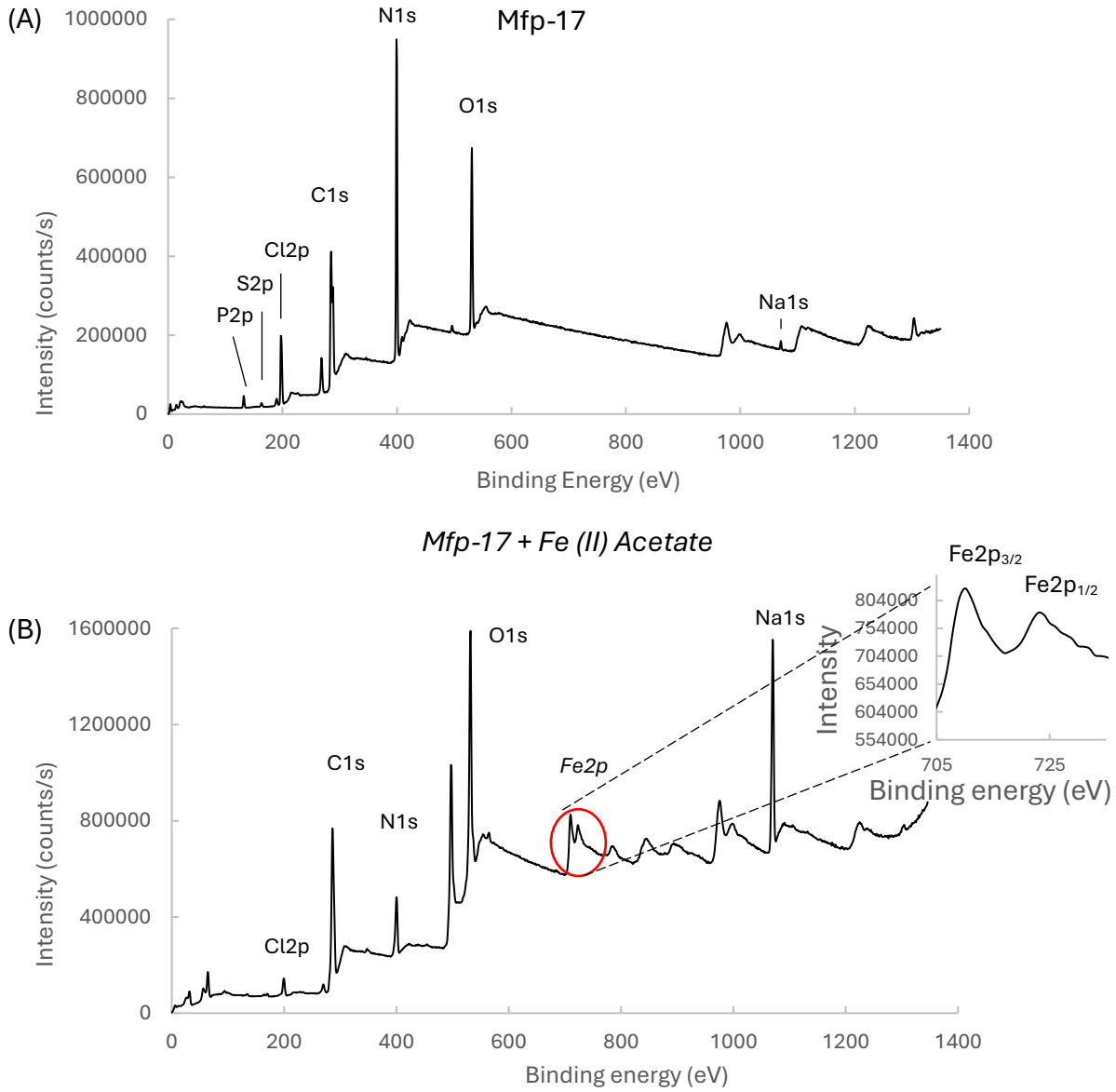

Figure 24. Dried protein films of dialyzed Mfp-17 demonstrate the ability to retain iron ions. A) XPS spectra of dried Mfp-17 negative control film without addition of iron (II) acetate shows no iron signal. B) XPS spectra of Mfp-17 dried film with iron (II) acetate shows clear presence of to Fe2p orbitals peaks, inset: Fe2p peak orbital splitting.

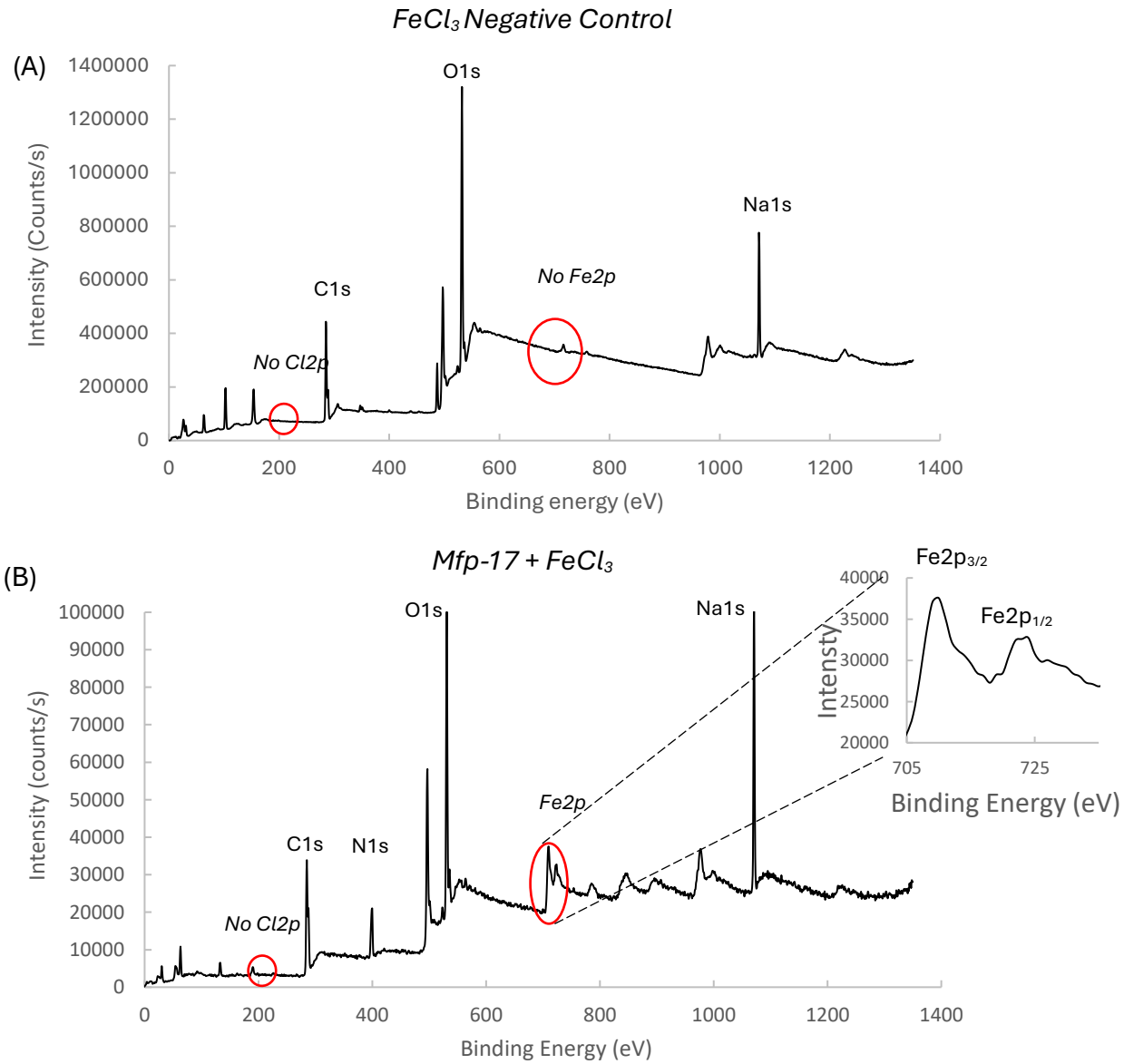

Figure 25. Mfp-17 further demonstrates binding with Fe^{3+} ions. A) XPS spectra of dialyzed $FeCl_3$ negative control solution demonstrating successful removal of iron ions. B) XPS spectra of dialyzed Mfp-17 dried film $FeCl_3$ shows presence of Fe2p orbitals peaks and loss of Cl2p signal, inset: Fe2p peak orbital splitting.

Mfp-17 – Fe(II) Acetate

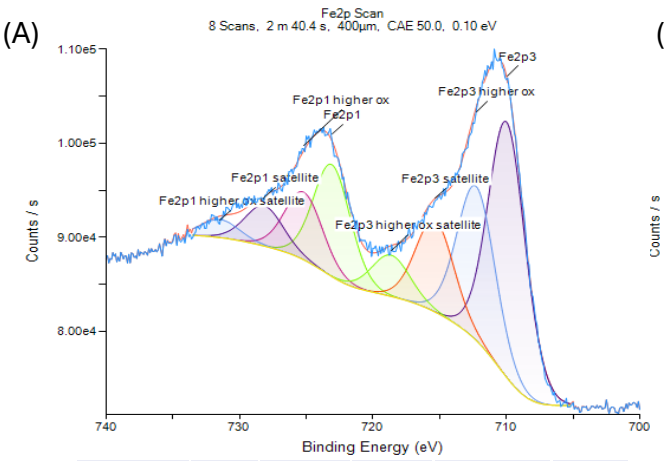

Name	Peak BE	Height CPS	FWHM eV	Area (N) TPP-2M	Atomic %
Fe(II) $2p_{3/2}$	709.97	27123.6	3.28	188.31	61.69
Fe(III) $2p_{3/2}$	712.26	16368.53	3.37	116.93	38.31

Mfp-17 – $FeCl_3$

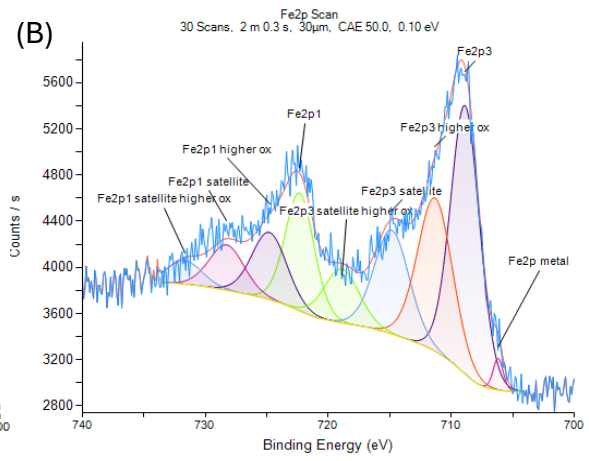

Name	Peak BE	Height CPS	FWHM eV	Area (N) TPP-2M	Atomic %
Fe(II) $2p_{3/2}$	708.87	2328.19	2.78	13.68	58.09
Fe(III) $2p_{3/2}$	711.31	1328.44	3.37	9.48	40.26

Figure 26. Mfp-17's iron binding demonstrates minimal differences between Fe^{2+} and Fe^{3+} salts. A) XPS spectra of Fe2p region at increased scanning resolution between Mfp-17 and iron (II) acetate. B) XPS spectra of Fe2p region at increased scanning resolution between Mfp-17 and $FeCl_3$. $Fe2p_{3/2}$ peak parameter table at the bottom of spectra.

The chemical state of iron was examined closer by comparing the XPS spectra of the Fe2p orbital region at greater scanning resolution for Fe^{2+} and Fe^{3+} salts (Fig. 26). The peak data were fit according to a combination of peak contributions of Fe^{2+} and Fe^{3} (higher oxidation) $Fe2p_{3/2}$, $Fe2p_{1/2}$, and their satellite peaks for a total of 8 peaks (Fig. 26) [120-122]. The $Fe2p_{3/2}$ peak was picked since it is the strongest peak which enables a more clear distinction of the contributions between Fe^{2+} and Fe^{3+} oxidation states in the Mfp-17-bound iron in the films, where ferric iron displays a $Fe2p_{3/2}$ peak at greater eV, typically greater than its Fe^{2+} counterpart [119, 121]. Despite sourcing iron ions of different oxidation states, the protein-iron XPS spectra shows the outcome iron signal is nearly identical by the very close atomic % of the fitted peaks; ~60% for Fe^{2+} and ~40% for Fe^{3+}. These results suggest that Mfp-17's iron binding presumably involves a control of iron oxidation, given that signals for both iron oxidation states appear at nearly equivalent levels regardless of the iron salt that is reacted with the protein. While it is not clear yet if Mfp-17 binds multiple iron ions per molecule, it is probable if compared to MTs which normally bind 7 metal ions per protein molecule despite even smaller molecular weight [72]. A single Mfp-17 unit

perhaps binds iron ions and interconverts them between different oxidation states, holding onto them at different oxidations states simultaneously. This mechanism has been demonstrated in uteroferrin, managing two iron ions between Fe^{2+} and Fe^{3+} oxidation states at the same time [123]. It could be argued that air oxidation could be a culprit responsible for the iron inter-change; however, the protein films are dried under vacuum, XPS spectra is measured under high-vacuum, and the outermost surface of the films were etched to remove surface contamination and oxidized protein. Nonetheless, while precise understanding of how many iron ions and in what oxidation state they are in after they interact with Mfp-17 is still unresolved, it is increasingly evident that Mfp-17 is indeed acting to sequester and bind iron ions regardless of their oxidation state under acidic conditions at which both Mfp-17 and iron ions are optimally soluble in aqueous environments. It is worth noting as well that byssus formation occurs under acidic conditions before being exposed to the more basic pH of seawater.

5.5 Mfp-17 pH-Triggered Transition into a Solid-State Iron-Coordinating Material

The pH-triggered transition of Mfp-17 into a solid precipitate upon exposure to increasing pH levels from acidic conditions as introduced earlier was taken advantage of to probe if Mfp-17 was capable of binding iron in a solid state. If indeed Mfp-17 was a major component of the byssal thread's cuticle matrix, then in theory its ability to bind iron should be maintained and perhaps even improved at neutral pH since that is what observed in the thread's natural context [25]. Mfp-17 was precipitated through pH-triggered solidification at neutral pH and combined with iron ions at different oxidation states in acidic pH, where a clear colour change from white to orange was observed (Fig. 27).

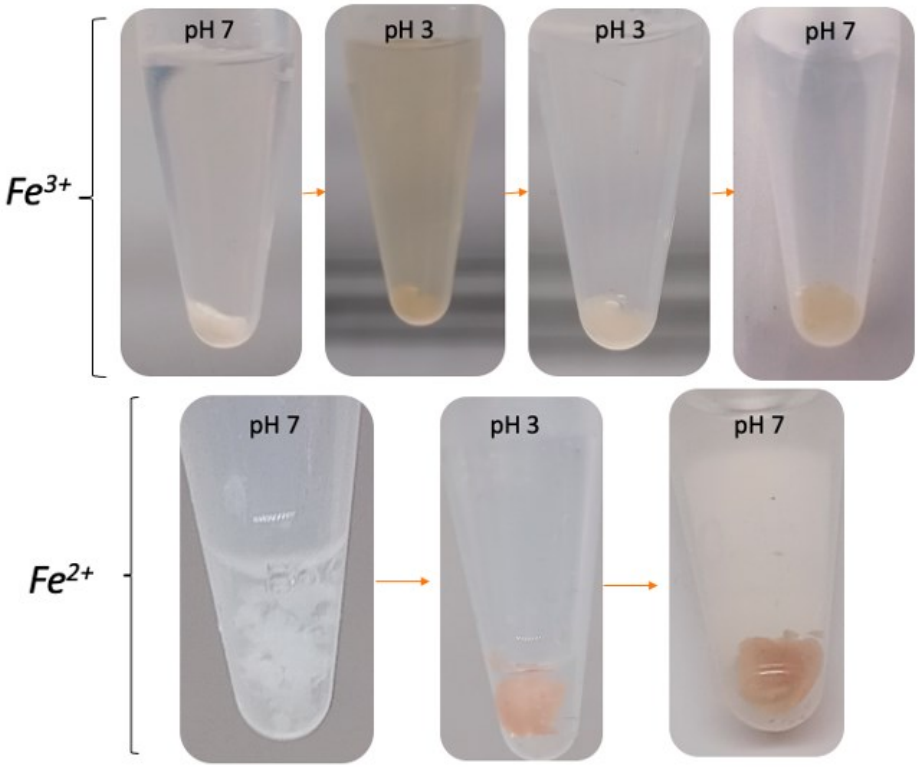

Figure 27. pH-triggered solidification of Mfp-17 enables binding to Fe^{2+} and Fe^{3+} chloride salts under acidic pH which continues to mature upon increasing pH to neutral levels

The proteinaceous material was processed by washing away unbound iron and increasing pH to neutral, where maturation of the material was indicated by further strengthening in the colour change of the solid material. The colour change from white to orange in the solid material is a sign of iron-coordination due to the propensity of many iron compounds to display colours of a similar colouration, like iron oxides. This material was characterised further by XPS to investigate the elemental composition and chemical state of iron in the material.

5.5.1 X-ray Photoelectron Spectroscopy

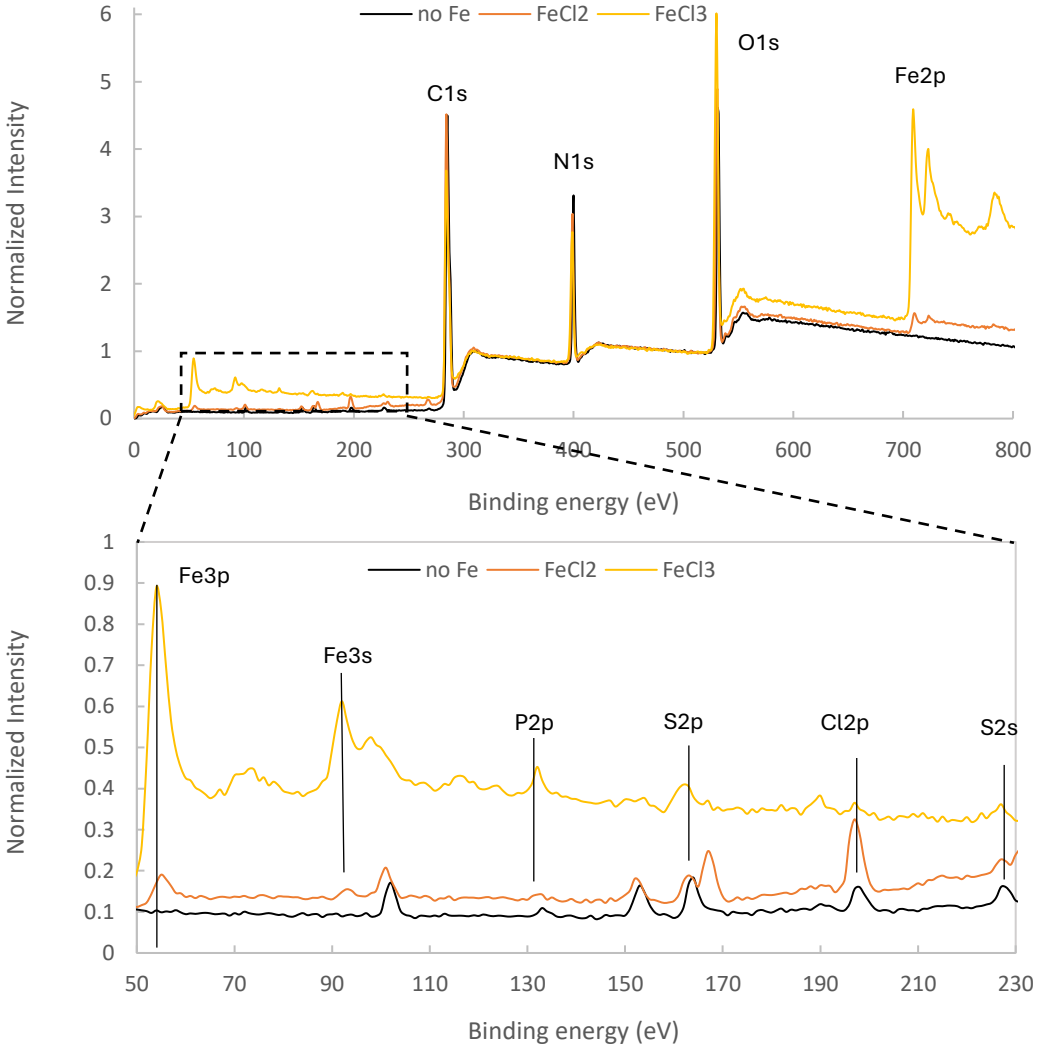

Figure 28. Solid-state Mfp-17 iron binding is compared between Fe^{2+} and Fe^{3+} chloride salts by normalized XPS spectra. The solid material demonstrates robust iron presence evident by the formation of Fe2p, Fe3p, and Fe3s orbital peaks, and potential modulation of cysteine residues due to differential peak splitting between iron oxidation states.

XPS was performed on the dried solid Mfp-17 material reacted with iron in different oxidation states (Fig. 28). The normalized spectra demonstrate the relative peak intensities of the iron signal between different iron ions. Ferric ions demonstrate a stronger signal than ferrous ions, but in both cases the iron peak signals are stronger compared to the previous XPS spectra from protein films in acidic conditions (Fig. 24 and 25). Unlike previous measurements, iron signals from additional orbitals including Fe3p and Fe3s are prominent. Together, the higher intensity and appearance of

additional orbitals in the iron XPS signal are evidence of increasing deposition of iron, suggesting solid Mfp-17 has greater binding affinity for iron atoms than in aqueous solution. Moreover, since equal concentrations of $FeCl_3$ and $FeCl_2$ (in excess) were reacted with Mfp-17, the greater intensity of iron signals with Fe^{3+} implies solid Mfp-17 may bind to it more efficiently than its ferrous counterpart. This is in agreeance with previous UV-Vis measurements. Sulfur signatures are also observable with measured S2s and S2p orbitals unlike in previous measurements, which provide information on what chemical state Mfp-17's cysteine could be in as possible iron-coordinating ligands.

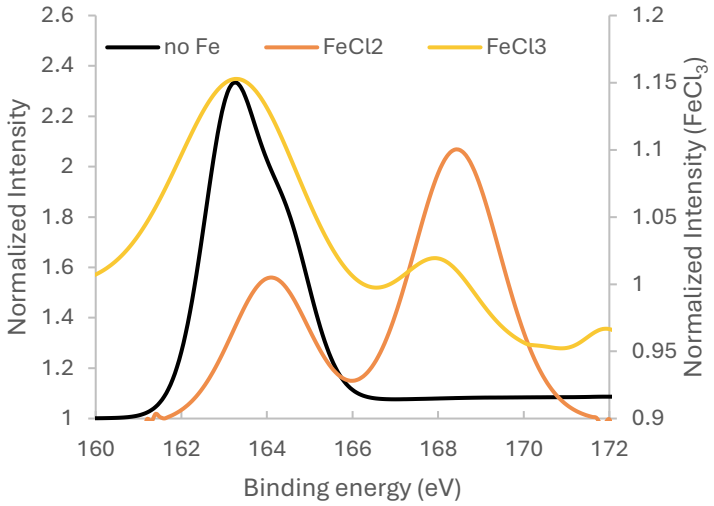

Figure 29. High-resolution scan of S2p orbital from Mfp-17 solid material reacted with different iron ions and unreacted without iron.

In the same manner as Fe2p, higher resolution scans of the S2p orbital were performed to compare the chemical state of cysteine between unreacted solid Mfp-17 and iron-coordinating Mfp-17 (Fig. 29). Cysteine's sulfur thiol and disulfide formation individually split into two peaks corresponding to $S2p_{3/2}$ and $S2p_{1/2}$ contributions in the 162-165 eV range [124]. For thiols, $S2p_{3/2}$ and $S2p_{1/2}$ are centered at ~163.3 eV and 164.5 eV respectively; for disulfides $S2p_{3/2}$ and $S2p_{1/2}$ are centered at ~164 eV and 165.3 eV respectively [124]. Although peak convolution does increase the difficulty in elucidating the chemical state of cysteine, generally cysteine in thiol form will be more closely centered around 163 eV, while under disulfide formation it will be instead more centered towards 164 eV[124]. However, cysteine-iron binding proteins also display S2p peaks within this range, often centred close to 163 eV or lower ~161.5 eV [125]. Examining the cysteine peak for solid

Mfp-17 without iron, a center peak at ~163.5 eV and a shoulder at ~164.5 eV are observed, which evidently convey that without reacting to iron, the bulk of majority of Mfp-17's cysteine is in a thiol chemical state, with possible small contributions from disulfide bonds because of the intensity between 165-166 eV. Dramatic changes in the S2p orbital occur when the protein material is expose to iron ions. For $FeCl_2$, Mfp-17's cysteine thiols become disturbed, evident by the positive shift of the $S2p_{3/2}$ peak from 163.5 eV to 164.5eV and increase in intensity between 165 and 166 eV, which are indicative of increasing cysteine disulfide bond formation, and potentially also due to iron coordination. Metal coordination of cysteine could decrease the electron density of the thiol, thus requiring greater energy to promote the ejection of the electron from the S2p orbital. Surprisingly, the $FeCl_3$ sample's S2p signal is noticeably different because a significant portion unexpectedly remains under a thiol chemical state compared to $FeCl_2$ since the $S2p_{3/2}$ peak is centered closer to 163 eV like Mfp-17 without iron. At the same time, $FeCl_3$ also shows signs of increasing disulfide bond formation from increase in $S2p_{1/2}$ signal between 165-166 eV, which could be expected given Fe^{3+} is more oxidized than Fe^{2+} and may further drive cysteine oxidation. Similarly, this increase in intensity at higher eV perhaps is attributed to iron-cysteine coordination. It remains elusive how Mfp-17's reaction with $FeCl_3$ shows higher levels of cysteine thiol and disulfide-bond formation simultaneously, which may likely be due to a convoluted signal with iron-coordinated cysteine. Furthermore, in both iron samples the formation of S2p peaks close to 168 eV is evident, which was previously associated with cysteine oxidation into a sulfonic acid [119, 126]. Cysteine oxidation into a sulfonate has been observed in the case of MTs exposed to hydrogen peroxide [126]. If this peak does indeed represent sulfonate formation, it is conceivable that cysteine oxidation occurs due to the excess of iron ions in the reaction process. It is possible that Mfp-17's iron binding may produce hydrogen peroxide or oxygen radicals in an unknown manner which could play a role in the protein's potential ability to manage iron oxidation similar to Fenton's reaction [127].

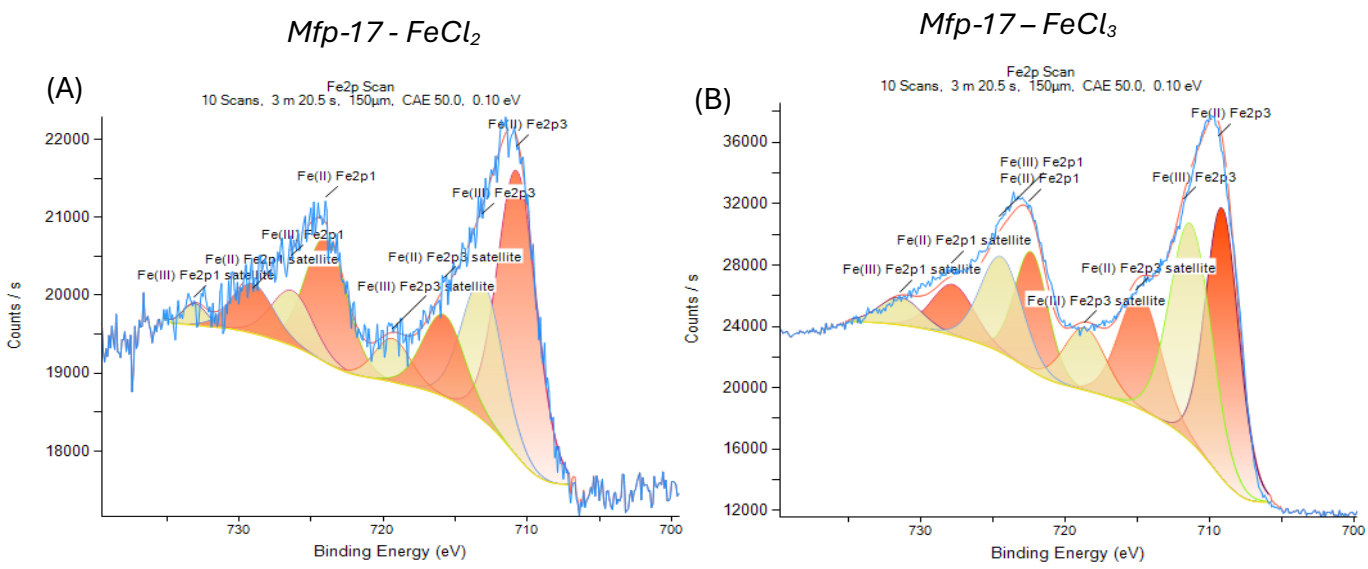

(C)

Mfp-17 – $FeCl_2$			Mfp-17 – $FeCl_3$		
Peak type	Peak BE	Signal%	Peak type	Peak BE	Signal%
Fe(II) Fe2p3	710.71	34.81	Fe(II) Fe2p3	709.34	30.2
Fe(III) Fe2p3	713.12	17.6	Fe(III) Fe2p3	711.83	20.35
Fe(II) Fe2p3 satellite	715.8	10.74	Fe(II) Fe2p3 satellite	715.09	12.05
Fe(III) Fe2p3 satellite	719.34	4.94	Fe(III) Fe2p3 satellite	718.7	6.64
Fe(II) Fe2p1	723.96	16.44	Fe(II) Fe2p1	722.54	13.42
Fe(III) Fe2p1	726.31	7.27	Fe(III) Fe2p1	724.63	9.04
Fe(II) Fe2p1 satellite	729.05	6.58	Fe(II) Fe2p1 satellite	727.89	5.35
Fe(III) Fe2p1 satellite	733.06	1.63	Fe(III) Fe2p1 satellite	731.5	2.95
	Total Fe^{2+} signal	**68.57**		*Total Fe^{2+} signal*	**61.02**
	Total Fe^{3+} signal	**31.44**		*Total Fe^{3+} signal*	**38.98**

Figure 30. Iron binding contribution differences between solid Mfp-17 reacted with $FeCl_2$ and FeCl3. A) XPS spectra of Fe2p region between Mfp-17 and $FeCl_2$ with fitted peak contributions from iron in different oxidation states. B) XPS spectra of Fe2p region between Mfp-17 and $FeCl_3$ with fitted peak contributions from iron in different oxidation states. C) Summary table of fitted beaks from A) and B) with overall contributions from iron in high and low oxidation states

Like previous results, solid-state Mfp-17 iron binding from low and high oxidation state iron was scrutinized by scanning the XPS spectra for the Fe2p orbital at greater resolution and fitting peaks to deconvolute the contributions of iron in different oxidation states (Fig. 30, A and B). Interestingly, the total contribution between Fe^{2+} and Fe^{3+} were very close to previous Fe2p scans of Mfp-17-iron films in liquid acidic conditions (Fig. 26) demonstrating similar fitted peaks despite

reacting with iron ions at different oxidation levels. This further reinforces that Mfp-17 can bind to iron ions at both oxidation levels in both liquid and solid states. The final contributions between the two iron oxidation states are also similar with a Fe^{2+} contribution at ~61-69% and 31-39% for Fe^{3+} (Fig. 30C). These contribution levels are similar to the levels seen in liquid acidic conditions (Fig. 26), suggesting that the iron binding arrangement between liquid and solid states of Mfp-17 are very similar with an overall greater presence of Fe^{2+} irrespective to the oxidation state of iron reacted with Mfp-17.

5.5.2 Raman Spectroscopy

To further explore the molecular structure of Mfp-17 and its coordination with iron, we utilized vibrational spectroscopy. Specifically, samples prepared the same way for XPS were examined by confocal Raman spectroscopy to probe for signatures of Fe-cysteine coordination, the suspected binding mechanism. Raman spectroscopy is a versatile technique in protein studies which can provide insight of secondary structure and state of amino acid side chains [128], but it also has significant promise in identifying relevant signatures of metal-cysteine coordination [129, 130]. The pH-triggered transition from liquid to solid was advantageous as it facilitated measurement on the iron-laden Mfp-17 solid material directly with good resolution. High quality Raman spectra were obtained for samples with and without iron in different oxidation states (Fig. 31). The intention was to identify the presence of peaks associated with metal-coordinating bonds previously measured in metal-binding proteins, in particular those corresponding to Fe-cysteine interactions. By comparing spectra of samples with and without iron, it was possible to examine which peaks were native to Mfp-17 while the formation of new peaks in the iron-exposed material would be attributed to vibrational modes associated with sulfur-iron coordination (typically appearing at lower energies). Moreover, information about Mfp-17 as a solid-state material could also be gathered by analyzing the peaks corresponding to the amino acid side chains (mainly aromatic residues but also chemical state of cysteine) and monitoring protein secondary structure through the amide I and amide III bands.

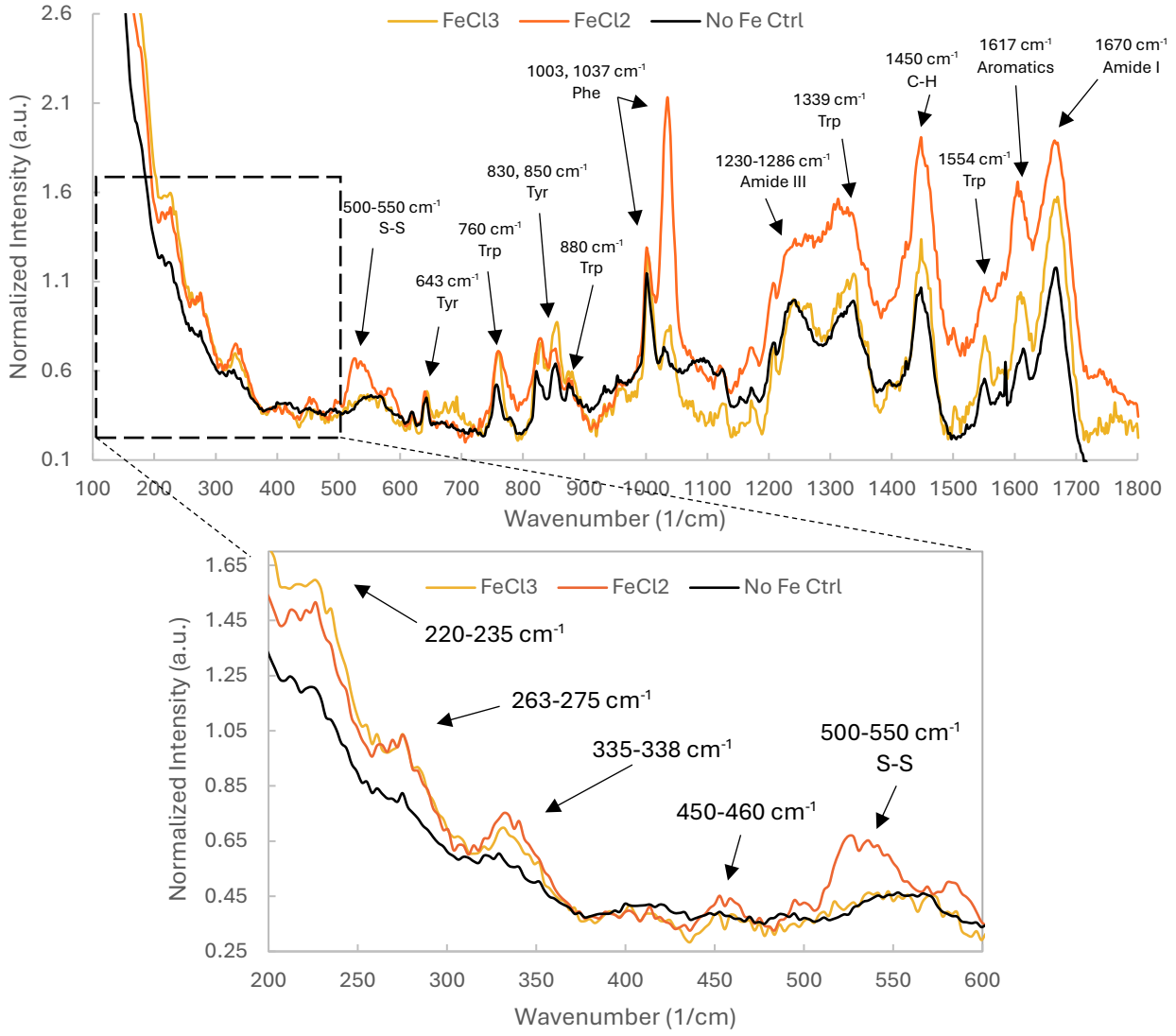

Figure 31. Raman spectra of Mfp-17 solid precipitates reacted with different iron chloride salts demonstrate probable signatures of iron-cysteine coordination in the 200-500 cm^{-1} range. Signatures of the protein backbone and aromatic residues were annotated according to literature [128]. Spectra were background subtracted and normalized to the phenylalanine peak (1003 cm^{1}).

Focusing first on examining the native signals from the protein, strong signals corresponding to the protein backbone and aromatic residues were evident as expected (Fig. 31). The Amide I and III regions demonstrate that the protein's secondary structure without iron is an extended conformation possibly a a β-sheet formation, evident by the peak centres at 1670 and 1240 cm^{-1} (Fig. 32) [128]. By the addition of iron, increase in regions associated with alpha-helices were noticed, primarily in the Amide III region where the formation of a peak at ~1320 cm^{-1} increased

above the peak are ~1240 cm^{-1} that would be consistent with increasing alpha-helical secondary in the protein. However, with alpha helical proteins, one would expect an associated shift of the Amide I peak to lower wavenumbers; yet, such a shift was not immediately obvious. In terms of side chains, I observed strong peaks for the aromatic side chains tyrosine, tryptophan, and phenylalanine, which was expected based on the protein sequence (Fig. 31) [128]. Surprisingly, despite Mfp-17's relatively lower phenylalanine deposition (4 residues, 2.2 mol%), its peaks are strikingly amplified in comparison to tyrosine which is significantly more abundant (15 residues, 8.2 mol%). Signatures of tryptophan also were evident, while histidine's was slightly noticeable at 1576 cm^{-1} [131] but convoluted with signals from other aromatic residues. It is not entirely clear why phenylaniline's peaks are magnified, perhaps it may have to do with Mfp-17's structural conformation as it transitions into a solid due to the important stabilizing activity that aromatic residues play in protein structure [132]. From the aromatic moiety, π-stacking phenomena is possible and is in fact known to play an essential role in protein self-assembly and molecular recognition, and even has been exploited to engineer self-assembling materials [133-135]. Studies of solidifying peptide fragments have further revealed that the presence of aromatic residues can dictate the aggregation process [136], which further depends on the type of residue as electron-donating aromatics like tyrosine may not be as effective in supporting this process like tryptophan or phenylalanine [137]; presumably due to the phenolic hydroxyl group altering the π-stacking mode [138]. Evidence of π-stacking in peptides is characterized in Raman spectra by examining the aromatic ring -C=C- stretch peak near 1600 cm^{-1}, which under π-stacking conditions it will display a downshift as observed in self-aggregating amyloid peptides [138]. Examining this region in solid Mfp-17 without iron, the peak appears split with a central peak at 1617 cm^{-1} with a shoulder at 1605 cm^{-1} (Fig. 33). This peak is often convoluted from multiple aromatic amino acid signals, but typically is centred between 1610-1620 cm^{-1} in proteins [128, 139, 140]. The downshifted shoulder to 1605 cm^{-1} from 1617 cm^{-1} may be indicative of aromatic residues under a π-stacking formation, that may be alongside non-π-stacking aromatics representing the peak at 1617 cm^{-1} [138]. This could explain why signatures for phenylalanine may be heightened despite its low content, as the residues are potentially interacting with other aromatic residues in π-stacked conformations after the pH-triggered solidification process, which has the potential to affect the polarizability of the aromatic ring and thus how intense the Raman effect would be.

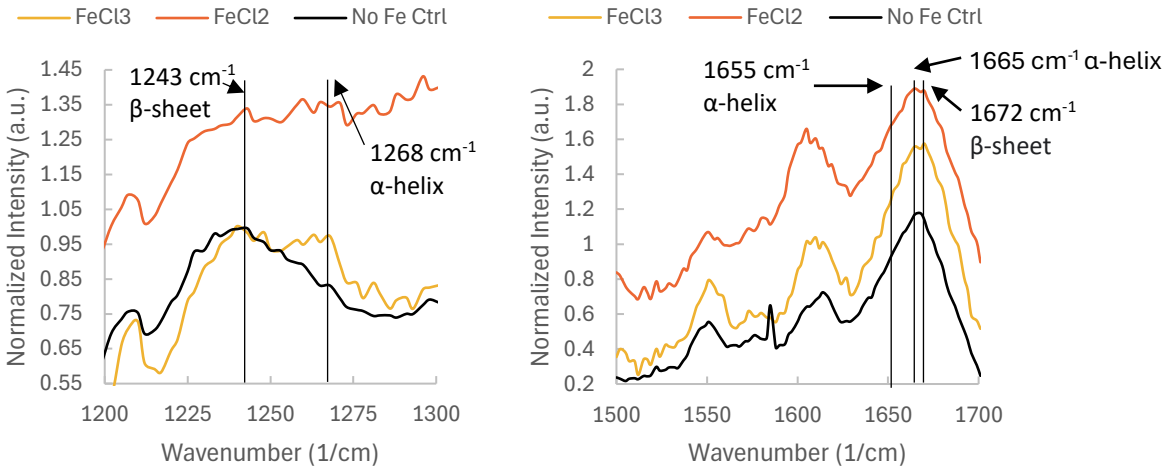

Figure 32. Closer examination of Amide I (right) and III (left) bands in Raman spectra of solid Mfp-17 shows potential change in protein secondary structure when exposed to iron ions, appearing to shift from a dominant beta-sheet conformation towards a more alpha-helical character.

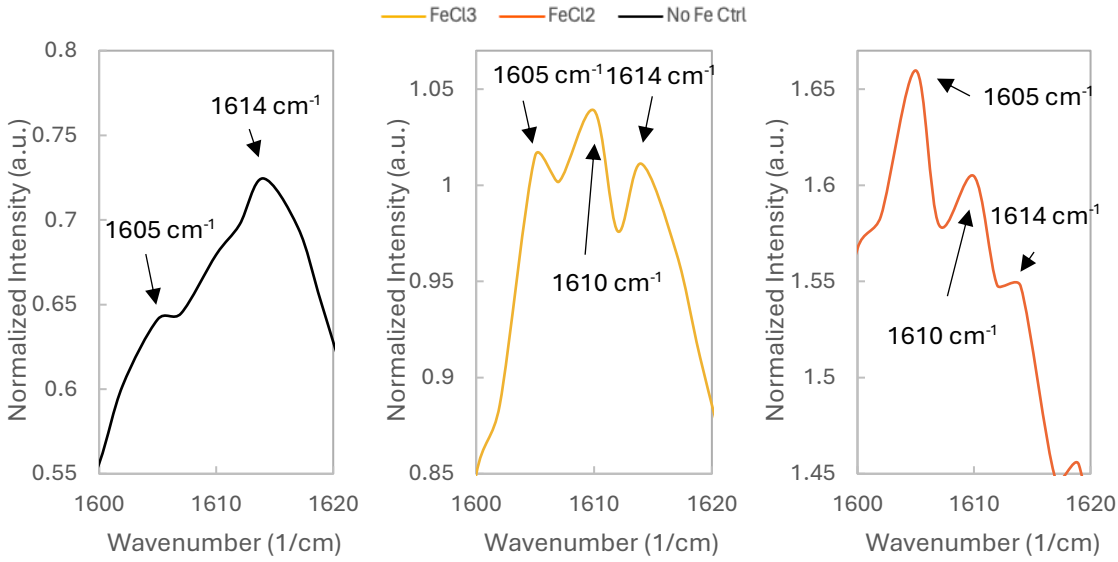

Figure 33. Closer examination of aromatic ring carbon stretch in Raman spectra of solid Mfp-17 demonstrates a downshift from 1614 cm^{-1} to 1605 cm^{-1} when exposed to iron, indicating enhanced π-stacking behaviour

Interestingly, the π-stacking effect is seemingly enhanced by the incorporation of iron in the material, indicated by the increased downshift of the peak at 1617 cm^{-1} towards 1605 cm^{-1} and 1610 cm^{-1} (Fig. 33). This is interesting because protein iron-coordination has been found to guide the interactions of aromatic residues that consequently manage the stability of the protein [87].

Complementarily, aromatic residues can influence and participate in the coordination of multiple metals, including iron, via ligand-aromatic interactions or direct cation-π binding [141, 142]. The proximity of aromatic residues to the metal-coordinating ligands too can improve binding affinity [143] or even control metal specificity entirely [144]. Mfp-17's aromatic residues may be working to form a protein structure that can coordinate iron ions in a solid state that is supported by π-stacking interactions, or even by cation-π interactions. To understand this effect in more detail, it would require more specialized investigation, likely via X-ray crystallography to resolve the protein structure which would be beyond the scope of this work [145]. Nonetheless, the idea that a significant deposition of aromatic residues in Mfp-17 is a mechanism with roles in pH-triggered solidification and iron-coordination is conceivable given that Mfp-1, a close cuticle protein counterpart, is already known to exploit cation-π and π-stacking effects for coacervation and adhesion [53, 146, 147]. In the case of Mfp-17, aromatic residues may be dominating how the protein folds as surrounding pH rises to drive self-aggregation and support iron-coordination. While it remains unclear how exactly this is happening, the intensity and shifts in the protein's aromatic Raman peaks do propose π-stacking interactions may be involved.

The different chemical states of cysteine can be tracked simultaneously by Raman spectroscopy as metal-coordinated, disulfide, and thiolate form Raman peaks at different wavenumbers due to their different bonding. Therefore, a snapshot of a protein's cysteines can be withdrawn from Raman spectra. The thiol stretch (-SH) forms a peak at 2500-2600 cm^{-1}, while disulfide bridges are between 500-550 cm^{-1} depending on gauche-trans conformations [148, 149]. These two modes are typical cysteine conformations in non-metal binding proteins, however, in cysteine-metal coordinating proteins the otherwise expected peaks in these regions vanish or become attenuated. For example, MTs with increasing zinc affinities display decreasing disulfide Raman peak formation, while displaying no -SH signatures at all [148, 150]. Therefore, the attenuation of disulfides and absence of thiol signatures in Raman spectra is a key feature of metal-coordinating cysteine-rich proteins, since the cysteines are instead bonding with the metal in alternate conformations, and so actually display weaker signatures of classical cysteine signatures despite a high cysteine deposition.

Like MTs, solid Mfp-17 displayed an absence of thiol -SH signatures at ~2500 cm^{-1} (data not shown) and differences in the disulfide peak formations ~500 cm^{-1} upon iron exposure (Fig. 31). Interestingly, Fe^{2+} appeared to increase and downshift the disulfide conformation of solid Mfp-17 compared to Fe^{3+} (Fig. 31). This suggests that there may be a differential cysteine-iron interaction between the two iron oxidation states, with Fe^{2+} apparently supporting further cysteine oxidation into disulfides that appear to be in a different conformation given that the peak is downshifted [151]. The effects of Fe^{3+} on disulfide formation are significantly more subdued with very small peak formations at 511 and 517 cm^{-1} that may correspond to slightly increased disulfide formation at different conformations [148], but nowhere near the same magnitude of Fe^{2+}. This supports Fe^{3+} as being a better coordinating ion given that the band formations at <500 cm^{-1} appear nearly the same as Fe^{2+} without the apparent oxidative toll, but there are conflicting details that make it hard to ascertain why this may be the case.

While ferric ions are more stable in oxygen-exposed environments due to natural oxidation and a greater positive charge that may be better suited for sensing negatively charged thiolates in cysteine coordination, previous XPS results suggest Mfp-17 coordinates iron in both oxidation states regardless of the source's oxidation state which implies it may possess a mechanism to manage iron ion oxidation. Based on speculation, a possible mechanism for Mfp-17's conversion from Fe^{2+} to Fe^{3+} that could cause the oxidation of cysteine may be derived from a Fenton reaction-like process involving oxygen. Such a process could be capable of interconverting between the two iron oxidation states while creating oxidative radicals that would be salvaged by the protein's cysteines in a controlled manner. The problem with this concept is that this process calls for the formation of oxidative reactive oxygen radicals, which would defeat the purpose of Mfp-17 acting as a reducing agent in the vicinity of the cuticle's matrix. Yet, a process like this could explain why there is a difference in UV-Vis measurements in oxygen-exposed and nitrogen-purged Mfp-17 reactions with iron (Fig. 20) and potentially why cysteine sulfonation may be observed in XPS spectra of solid Mfp-17 reacted with $FeCl_2$ and not $FeCl_3$ (Fig. 29). Another explanation could be natural oxidation of the material, however, both samples were processed in the same manner, and it would be expected that the level of cysteine oxidation would be more similar between both types of iron. Furthermore, evidence of disulfide bridge bonds in the material before and after iron-

exposure demonstrate that not all cysteine residues are involved in iron-coordination, potentially instead playing roles in protein folding structure.

By comparing the spectra between the iron-loaded material to the same material without iron, the more significant differences were noticeable in the lower wavenumber range (200-500 cm^{-1}), where broad peak formations centred close to 225, 275, 338, and 450 cm^{-1} formed upon the addition of iron (Fig. 31). What's more, a nearly identical response was produced regardless of the oxidation state of iron salt used, showing peaks at the same locations (Fig. 31). This was a promising result since the bond signatures attributed to cysteine-metal coordination in metallothioneins and Fe-S cluster proteins lie within this range [129, 130]. Therefore, it was very possible that the iron-induced peak formations were derived from cysteine-iron coordination in the material. The coordination of cysteine with metal ions is characterized by terminal and bridging modes of coordination, which correspond to the number of metal ions they coordinate to. Terminal cysteine only coordinate a single metal atom, while bridging cysteine coordinates more than one. These modes have been characterized separately via Raman spectroscopy, both with signatures at wavenumbers below 500 cm^{-1} which is advantageous since they could be used to decipher the different modes of metal coordination by a protein's cysteine residues [129, 130]. Generally, signals at higher wavenumber ranges between 395-430 cm^{-1} correspond to bridging cysteine metal coordination, while lower signals between 250-370 cm^{-1} instead are often assigned to terminal cysteine metal coordination [129], however, the assignment of these bands change depending on the metal and the protein, and vary in different cases [130, 150].

MT cysteine-metal coordination is often attributed to a broadband Raman band formation centred between 290-310 cm^{-1} with shoulders around 320 and 340 cm^{-1} due to the S-M stretch; the peak centre depends on the protein and type of metal [129, 148, 150, 152, 153]. A similar form of Fe-S coordination signal is also observed in alternative proteins like rubredoxin and rubrerythrin that similarly coordinate a single Fe atom tetrahedrally via cysteine ligands and produce an intense characteristic band near 314 cm^{-1} from the Fe-S bonds [154, 155]. Examining Mfp-17's Raman spectra at the range between 300-320 cm, there are relatively weak peaks at wavenumbers within this range that align at the expected band wavenumbers in literature, however, most likely are noise due to their weakness (Fig. 34A). Thus, we are cautious in assigning these smaller peaks. Indeed, these bands appear relatively faint in comparison to the more prominent peaks near 270 and 330

cm^{-1} that also display a multitude of smaller peaks and shoulders in-between most likely arising from noise as well. Nonetheless, further discussion of the peaks in this range is undertaken below in order to understand the Raman spectra signatures of more diverse Fe-S clusters in the 200-450 cm^{-1} range [130] and examine if their formation in Mfp-17 was plausible and characteristic of a specific geometry (Fig. 34).

Previous work on a novel MT identified a potential [2Zn-2S] metal-cysteine coordination cluster formation by identifying a Raman peak formation pattern in the spectra that was very close to the one observed before in [2Fe-2S] ferredoxins with bands at 282, 327, 340, 357 367, 395, and 426 cm^{-1} [150, 156]. The bands at 282, 295 340, and 357 cm^{-1} are assigned as terminal cysteine ligands, while the remaining bands at 327, 395, and 426 are assigned to bridging sulfides [150, 156, 157]. In Mfp-17's spectra, a similar peak pattern formation appears to correspond to [2Fe-2S] cluster formation (Fig. 34B) that appears to potentially suggest the presence of these clusters in the proteinaceous material. Due to the relative weakness of these bands, it is not yet possible to conclude from the spectra that indeed these clusters are being formed in the material and so must be attributed to noise. Nonetheless, it is intriguing that the strongest band expected for this cluster geometry at 284 cm^{-1} alongside other bands do align with peaks in the spectra for both samples reacted with different iron oxidation (Fig. 34B)

The signatures of [3Fe-4S] and [4Fe-4S] clusters were also examined (Fig. 34 C,D); they held increasing prospects since these clusters can demonstrate strong bands near 270 and 330 cm^{-1} respectively that could help explain the broad, strong peaks observed near these regions in Mfp-17's spectra [158, 159]. The Raman spectra of solid Mfp-17 were annotated with the expected bands for [3Fe-4S] and [4Fe-4S] clusters with the goal to identify peaks at the same wavenumbers that could be attributed to each type of cluster (Fig. 34 C,D) [157-163]. In particular, the A_1^b modes for bridging Fe-S are the most characteristic for both [3Fe-4S] and [4Fe-4S] due to their strongest Raman peak intensity, which are between 346-348 and 333-339 cm^{-1} respectively [161]. According to this assignment, [4Fe-4S] clusters perhaps could be a notable component of iron coordination in the material since the band at 332 cm^{-1} in the Raman spectra is the strongest peak visible between 200-450 cm^{-1} (Fig. 34). This band does align with the strongest Fe-S band in [4Fe-4S] geometries in ferredoxins [161]. This band also is significantly stronger than the bands at 283 and 343 cm^{-1}, the strongest bands attributed to [2Fe-2S] and [3Fe-4S] clusters. What's more, nearly

all the smaller peaks for potential Fe-S bridging and terminal bonds of the [4Fe-4S] cluster seemingly align with peaks or shoulders in the Raman spectra near the expected wavenumbers which is intriguing (Fig. 34D) but at this point, cannot be differentiated from noise due to their relative weakness as mentioned earlier. In contrast, [3Fe-4S] bands do not align well with the spectra in comparison to [4Fe-4S] (Fig. 34 C,D). Additionally, the macroscopic colour change from white to orange/red in the material could be a qualitative signature of Fe-S cluster formation given that these clusters absorb light in the UV-Vis range between 300-600 nm (Fig. 27) [157-159, 164]. This light absorbance is associated with the production of a yellow to red colour due to the absorption of blue and green light wavelengths. While UV-Vis light spectroscopy could not be measured in the solid material, the significant shift colour change after iron exposure is further evidence that Fe-S cluster coordination is occurring in the material.

It remains uncertain what strategy Mfp-17 is taking advantage of to bind iron. The comparison of the measured Raman spectra with other types of cysteine-iron binding proteins appears to suggest that Fe-S cluster-like formations may be involved. At this time, however, it is not possible to ascertain the mode of coordination between iron and cysteine, but peak alignments with the strongest bands from [2Fe-2S] and [4Fe-4S] in particular were notable. Mfp-17 may be incorporating Fe-S clusters as a mechanism to bind to iron, or at least a cluster-like system. It must also be considered that the measured interactions are occurring in a solid-state unlike the ferredoxin clusters being compared to. The mode of Mfp-17's iron-cysteine coordination in the solid-state may be similar to Fe-S clusters but is likely to differ since Mfp-17 is acting differently, not coordinating iron in a liquid state in this case.

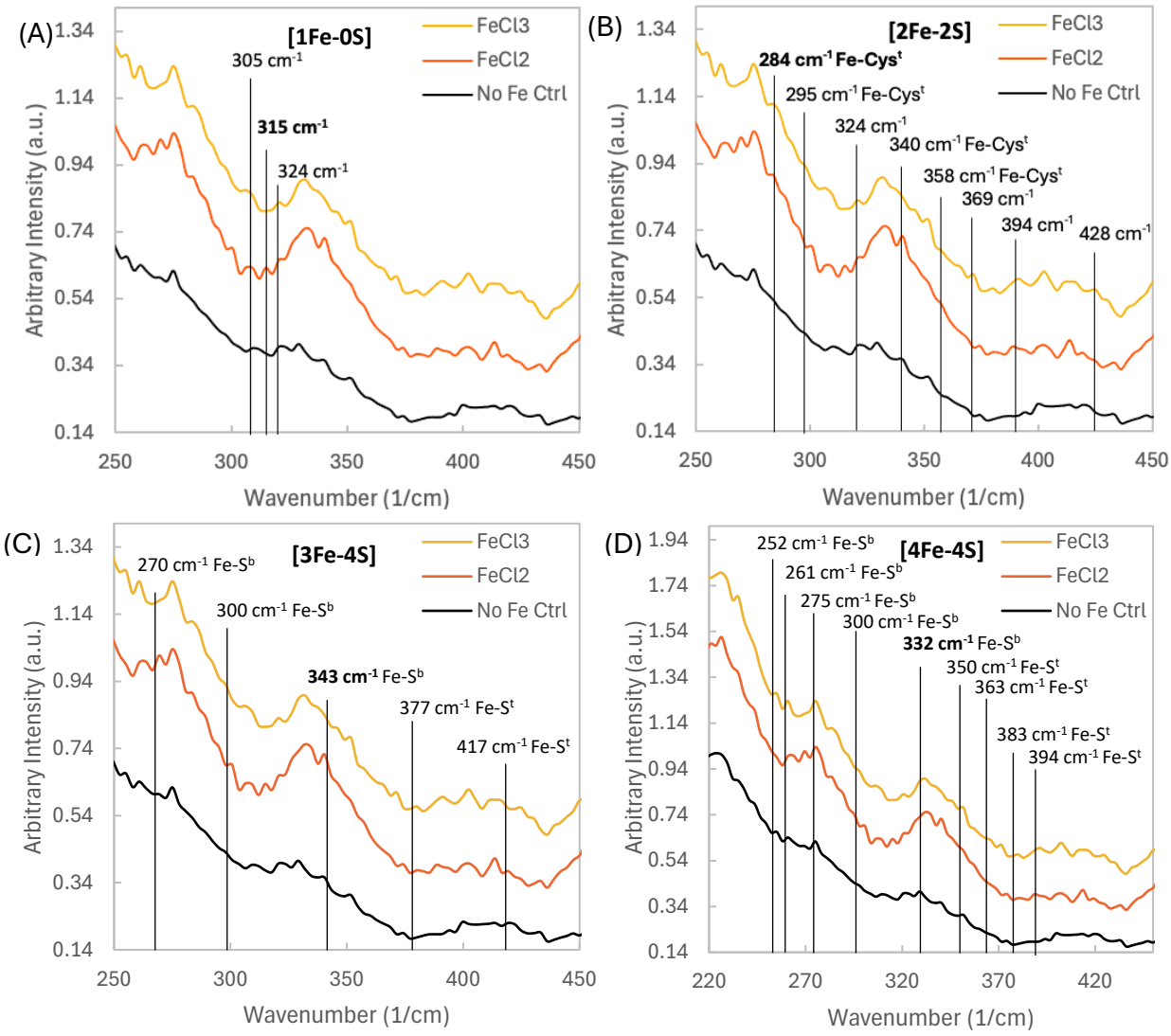

Figure 34. Spectra of solid Mfp-17 reacted with iron chloride salts are examined against known Fe-S cluster bands formations of diverse geometries. A) Analysis of Raman band formations attributed to Fe-S bonds in MTs and ruberythrin's Raman spectra [129, 130]. B) Analysis of band formations attributed to [2Fe-2S] ferredoxin-like coordinating clusters [150, 156, 157]. C,D) Analysis of band formations attributed to [3Fe-4S] and [4Fe-4S] ferredoxin-like coordinating [157-163]. Strongest expected bands are bolded.

The prescence of Fe-S clusters in Mfp-17 is unusual since in typical Fe-S cluster proteins, inorganic sulfide plays a role in coordinating iron as well as cysteine. If indeed Mfp-17 is forming Fe-S clusters in a solid-state, it is unknown if sulfide ions are involved. While the Fe-S^b bands do s a sulfur ligand is coordinating to more than one iron ions, perhaps this signal could also be

derived from cysteine ligands coordinating to multiple ions instead of sulfides. It is unlikely sulfide ligands that could be sourced from within the cell under recombinant protein production are maintained bound to the protein due to the use of denaturing conditions which would break the coordinating structure and likely release any bound sulfide. To assess this in the future, performing isotope shifts with a different sulfur or nitrogen isotopes in the reaction to modify the sulfide or cysteine ligands respectively, will produce a shift in the Raman spectra that will indicate if sulfide is playing a role [156, 163]. Furthermore, the idea that Fe-S clusters would be active in the cuticle is counterintuitive because they are sensitive to oxidation and traditionally are protected from oxygen exposure, both of which would be disturbed in seawater exposure. While oxidation will not necessarily remove bound iron in the cluster, it can affect conformation [164, 165]. That being said, Fe-S clusters are redox-active and do play efficient roles as electron-donors in many systems [166]. This system does support Mfp-17's hypothesized functions in the cuticle: strong reducing properties and iron-coordination. The distinction between reducing and coordinating cysteine's remains uncertain at this point, but the concept that Fe-S clusters could enhance or perform DOPA reduction perhaps is plausible since nearly all Fe-S clusters have a negative redox potential and thus an ability to create a reducing environment [166]. Indeed, even after iron coordination, solid Mfp-17 still continues to demonstrate reducing properties in Ellman's assay (data not shown).

Perhaps Mfp-17 does not use a single structure to coordinate iron, maybe taking advantage of multiple geometries at once. This is not an unknown case, as many Fe-S cluster proteins do in fact switch between different geometries depending on conditions like oxidation, and can even co-exist within the same protein or separately as mixed-species at the same time [159, 164-166]. This further suggests that the polymeric structure formed by Mfp-17 may be inherently complex with an evolved capability to sequester iron in multiple modes, and even under different conditions like different iron oxidation states. This would make sense given that Fe-S clusters are inherently sensitive to environmental oxygen exposure as well as oxidative stress, often inducing conformation transitions between different geometries [130]. Given that byssal threads are always exposed to such conditions in seawater, it stands to reason that Mfp-17 would have evolved a mechanism to counter these problems. Perhaps this mechanism is imbedded in the transformation process into a solid-state polymeric material, enhancing the protection of iron-coordination by escaping the vulnerabilities in an aqueous state. Solid-state Fe-S clusters are unlike virtually all

other known types of Fe-S cluster proteins as they are all known to function solely under aqueous conditions due to their role in the living cell. Moreover, their biogenesis is a complicated orchestrated process *in vivo* [157]. Yet, it appears that a solid state facilitates the interaction between Mfp-17 and iron, which may be due to structural changes as the protein aggregates and a pH that increasingly supports Fe-S interactions, effectively eliminating the requirement for an orchestrated assembly system since the protein could fold autonomously into a confirmation that supports the iron coordination. While this functional prospect is exciting, more experimentation is necessary to examine iron coordination with improved resolution in the material. After cross-examinations with protein Fe-S Raman spectroscopy experiments, it's clear a resonance effect is attributed to the production of the vibrational signals in iron-sulfur coordination [130]. As such, Raman spectra measurements of these systems are optimally enhanced with blue lasers between 400-490 nm by being closer to the S → Fe charge transfer transition range, and require high sample concentrations due to the low extinction coefficient of the Fe-S interactions [130]. The samples are also typically measured under very low temperature (14-77 K), a factor that is crucial to narrow the output signal bandwidth; this is a requirement since the bands for different Fe-S clusters are so close together [130]. Therefore, future experimentation of this material with a blue laser and low temperature is bound to produce spectra with significantly improved resolutions compared to the presented spectra in this work that were measured with a green 532 nm laser at room temperature. Despite this, it is significant that even without optimal measurement conditions, peak signatures for Fe-S coordination in solid Mfp-17 were captured due to the evident robust ability for Mfp-17 to coordinate and stabilize bonds with iron ions.

5.6 Coacervation Between Recombinant Cuticle Cysteine-Rich Mfps and rMfp-1

Coacervation plays an important role in facilitating the assembly of a byssal thread. In the cuticle, phase separation between granules and the matrix is observed already at the nascent vesicle stage, signifying that the inherent properties of the cuticle's protein building blocks like Mfp-1 and the cysteine-rich Mfps support coacervation [25]. Therefore, it was important to assess if the known process of Mfp-1 self-coacervation would be affected by Mfp-16 or -17 in the same vicinity, as it occurs in the thread's cuticle. Coacervation phenomena was expected to be possible between Mfp-1 and Mfp-16/17 since the Mfp-1 rich granule naturally phase separates from the cysteine-rich Mfps in the matrix in the byssal thread's cuticle. With the goal to assess if coacervation could be

simulated between the recombinantly-produced building blocks, highly concentrated solutions of recombinant Mfp-1 (rMfp-1, $[AKPSYPPTYK]_{12}$) and Mfp-16 or -17 were combined at different pH levels with increasing salt concentration. Recombinant Mfp-1 alone coacervates at an ionic strength close to that of seawater [53], but it was uncertain if the presence of the cysteine-rich Mfps around it would disrupt this effect via inter-molecular interactions. Initial reactions at pH 7.0 did not coacervate, instead leading to the formation of precipitate aggregates upon the addition of 500 mM NaCl to a 1:1 reaction of rMfp-1 and Mfp-16 (Appendix C) mimicking seawater ionic strength. At the same conditions, rMfp-1 alone was capable to form simple coacervates (Appendix C). The precipitation of Mfp-16 at neutral pH had been observed previously in metal-binding experiments, but it was necessary to assess if an interaction with rMfp-1 would modulate this process. To circumvent pH-triggered protein solidification, following experiments were instead performed in acidic conditions, where Mfp-16 and -17 are soluble. This change proved to be fruitful, leading to the successful formation of coacervates between rMfp-1 and both, Mfp-16 and -17 (Fig. 35). The coacervation process was macroscopically noticeable by the increased turbidity of the solution, which when examined under the microscope evidently demonstrated dense coacervate droplets of diverse sizes. After deposition onto a glass slide for imaging, the process was visibly active with coacervate droplets moving in different directions and coalescing together.

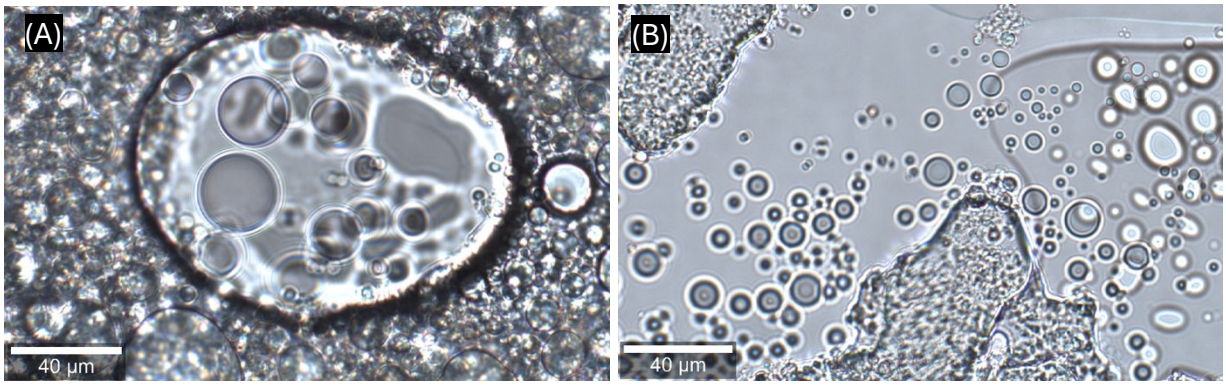

Figure 35. Coacervation morphology observed in the reaction between concentrated rMfp-1 and Mfp-16/17 at pH 3.0 and 300 mM NaCl. A) rMfp-1 coacervation with Mfp-16 at 1:1. B) rMfp-1 coacervation with Mfp-17 at 1:1. Images taken with a 50x objective; scale bar: 40 µm.

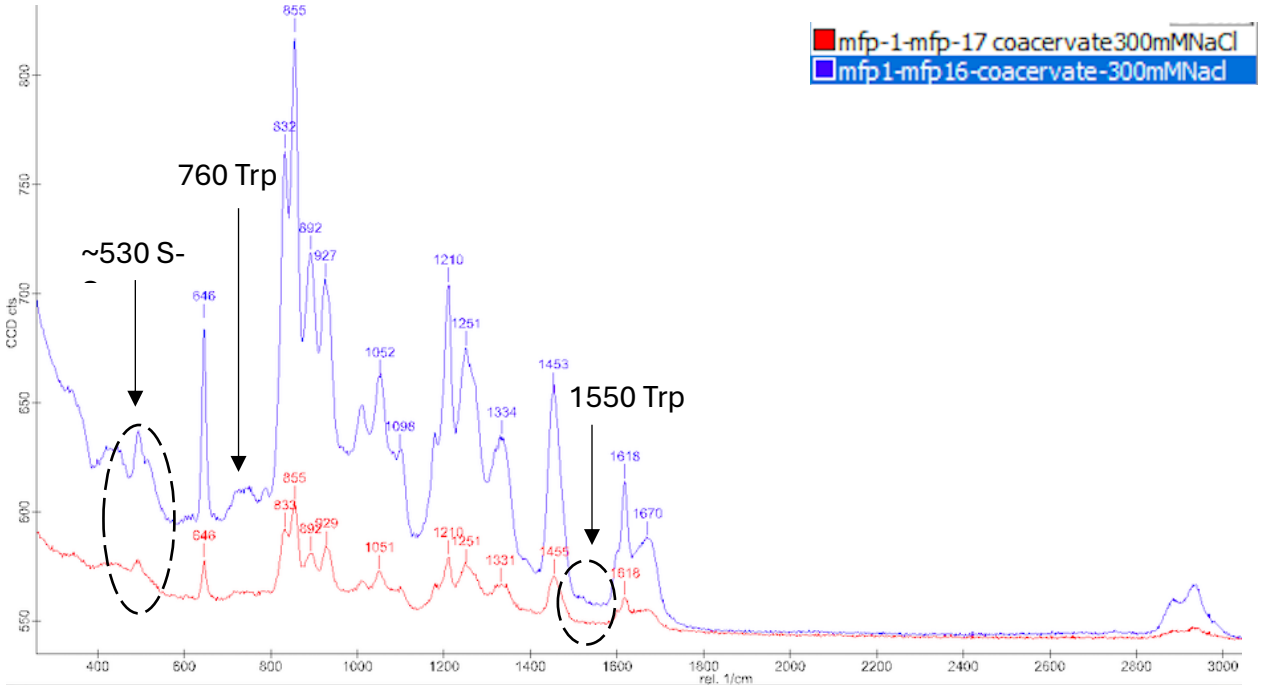

Figure 36. Raman spectra of dense coacervate phase comparison between reactions with Mfp-16 and Mfp-17. Annotated are peak signatures for amino acid side chains not expected for rMfp-1

To discern the composition of the coacervate phase, Raman spectra of the dense coacervate droplets were measured (Fig. 36) and compared between coacervates of Mfp-16 to Mfp-17. It was challenging to ascertain if the coacervate was entirely composed of rMfp-1, or if the cysteine-rich Mfps were included in the dense phase due to a similar pattern in amino acid composition. Cysteine and tryptophan side chain peaks were examined in the spectra since rMfp-1 does not include either of these, while Mfp-17 contains both and Mfp-16 contains only cysteine. The spectra reveals that the majority of the coacervate composition is from rMfp-1with potentially a minor composition of cysteine-rich Mfps, based on the presence of a disulfide peak that is associated with cysteine. The lack of tryptophan signatures in Mfp-17's coacervate Raman spectrum is likely due to the very low concentration of the protein in the coacervate. While the coacervate morphology did not resemble the granule in the cuticle's matrix, this is most likely because the recombinant Mfp-1 sequence does not include the more hydrophobic region from the full sequence that could be playing a role in the granule's coacervate morphology [25]. Also interesting, the coacervation process was achieved at an ionic strength that is ~50% lower than required for rMfp-1alone (300 mM NaCl) [53]. Apparently Mfp-16 and -17 enhance the propensity for its Mfp-1 counterpart to undergo coacervation. Together, these experiments are evidence that rMfp-1 coacervation can be achieved

and potentially enhanced when within the same vicinity as Mfp-16 and Mfp-17, supporting the role of cysteine-rich Mfps as significant cuticle matrix components. The present, but limited integration of Mfp-16/17 into the rMfp-1 coacervate system resembles the hypothesized organization of the granule and matrix, where cysteine-rich Mfps are thought to be primarily localized in the matrix but also limitedly integrated in the granule [25]. To better understand the protein deposition in the coacervate system, fluorescent tagging of the proteins and imaging will assist in discerning the localized protein composition of the dense coacervate phase in the future.

5.7 Mechanical Role of Cysteine-rich Mfps and Influence of Iron Coordination

The surface forces apparatus (SFA) technique was employed to probe the mechanical performance of Mfp-17 films and gauge if iron coordination in the material can enhance its cohesiveness. SFA is a specialized technique that involves examining the force profiles of two mica surfaces that are coated with chemical components (Mfp-17 in this case) through adsorption to understand if bond formation between the surfaces can produce adhesive force. This adhesive force provides information of chemical bonding occurring between the two surfaces, which is a necessary attribute to assess a material's cohesion. This technique has been applied effectively with Mfp-1 and its recombinant versions to better understand the protein's interactions as well as the mechanical role of catechol-metal coordination [40, 146, 147, 167, 168]. For this technique to work, the examined agent must adsorb to a mica surface. It was expected that Mfp-17 was going to be capable of adhering to mica like Mfp-1 due to the relative similarities in amino acid composition. The deposition of protein on a mica surface is indicated by a hardwall formation that is sensed during SFA measurements. Mfp-17 indeed formed a hardwall on the mica surface as exampled by the asymptote shift to >0 nm in the distance of the SFA force-distance profiles, having a thickness of ~ 11 nm (Fig. 37). The effect of metal-catechol coordination in Mfp-1 film adhesion on mica is drastic, strongly amplifying the adhesion force between the symmetric surfaces to magnitudes > 20 mN/m, while without metals, adhesion is starkly abolished [40, 167]. Moreover, three important factors that enhance Mfp-1's surface adhesion can be withdrawn from SFA measurements: 1) Exposure to metal (i.e., iron, vanadium), 2) shift in pH from acidic to basic conditions, and 3) longer contact times [40]. Therefore, it was intriguing whether a similar pattern to Mfp-1 would be displayed by Mfp-17.

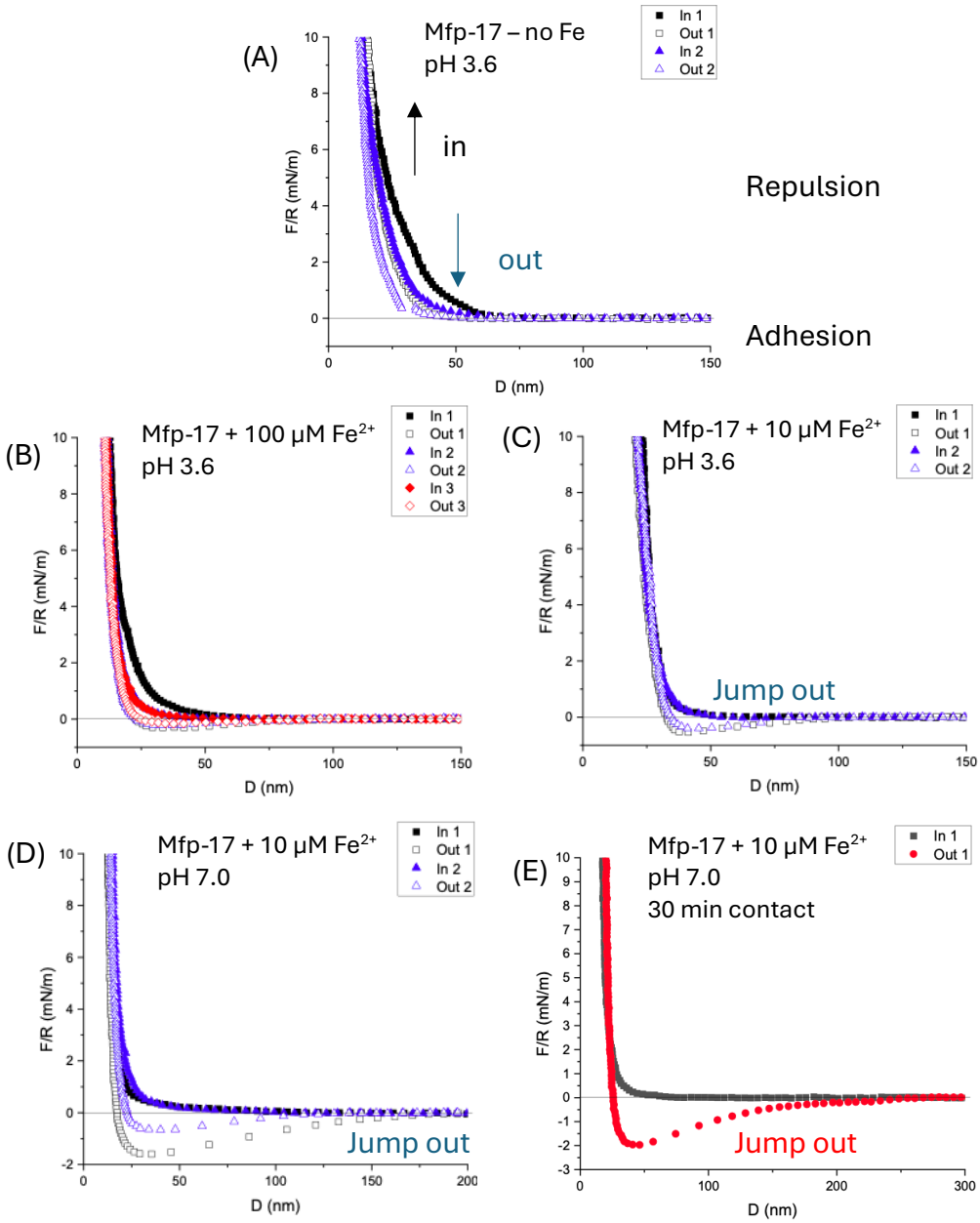

Figure 37. Mfp-17 demonstrates a strong ability to adsorb onto mica surfaces and form a hardwall with minimal adhesive bridging at acidic pH. Adhesive bridging is improved by the addition of iron ions, an increase to neutral pH, and longer contact times. Force-distance profiles of symmetric Mfp-17 films on mica tested in a SFA setup: A) short contact with Mfp-17 at pH 3.6, B) short contact with Mfp-17 incubated with 100 μM Fe^{3+} at pH 3.6, C) short contact on a new surface with Mfp-17 incubated with 10 μM Fe^{3+} at pH 3.6, D) short contact with Mfp-17 incubated with 10 μM Fe^{3+} at pH 3.7, D) longer contact (30 min) with Mfp-17 incubated with 10 μM Fe^{3+} at pH 3.7. Short contact is ~5-10 min. The y-axis (F/R) in mN/m depicts force/radius as a term for cohesive force between surfaces. The x-axis is associated to the surface hardwall distance.

Like Mfp-1, Mfp-17 did not display adhesion between itself in acidic conditions where solubility is optimal (Fig. 37A) [168]. However, the introduction of iron did increase adhesion between the surfaces (Fig. 37 B, C). That is evident by the increase in negative force as the surfaces are pulled apart leading to a jump out. It appeared that an iron overload was detrimental to this effect, as 100 μM Fe^{2+} concentration was not effective compared to a lower 10 μM Fe^{2+} concentration in causing this effect. This can be explained by the saturation of iron across the film's surface, eliminating the possible interactions between the two surfaces by occupying all the locations that could form bridging coordination bonds with iron ions. Adhesion increased as the pH in the solution between the surfaces was increased from 3.6 to 7.0 (Fig. 37D), and even further when the contact time was extended to 30 min (Fig. 37E). Relative to Mfp-1, the maximal adhesion force achieved is lower, with the strongest force measured at about 2 mN/m, but this could be expected by cross-examining to the byssal thread's cuticle performance. In this context, the Mfp-17-rich matrix is the component with the sacrificial bonds responsible for managing mechanical failure and thus, Mfp-17 would be expected to display adhesive forces lower than that of Mfp-1's catechol-metal coordination in the granules due to weaker bonds [26]. Notably, adhesive force increased 3-fold by shifting from an acidic pH towards neutral conditions, suggesting that a pH transition also plays a role in improving adhesive work like observed in rMfp-1, which only improved by about 30% in comparison [40]. Longer surface contact time also improved Mfp-17's adhesive force like Mfp-1 [40], which makes sense since it provides longer window for bond formation to proceed further. Comparing the adhesion force between rMfp-1 and Mfp-17 at the same contact time and iron concentration, Mfp-17's force is only about a quarter to that of rMfp-1 (1.97 mN/m vs 8.6 mN/m) [40].

Integrating this information, Mfp-17 displays a similar pattern to Mfp-1 where adhesion force is improved by the exposure to iron ions, increasing pH, and longer contact times (Fig. 38). This signifies that Mfp-17 can build chemical bonds capable of mechanical work that can create a cohesive material, which as expected are weaker than catechol-metal coordination by Mfp-1. Iron also appears to influence this effect, inducing increased adhesion between Mfp-17 surfaces at acidic pH where otherwise there is none. Additional Mfp-17 SFA experiments revealed that bridging disulfide bond formation between cysteine groups across the surfaces is not contributing to surface adhesion, and that native protein adhesion increases by an increase in pH even without exposure to iron ions (data not shown). While it remains unclear how adhesion in Mfp-17 is

enhanced by a shift in pH alone without iron, perhaps it is related to the solidification process inherent in the protein. In this perspective, by increasing pH the intermolecular affinity of the protein to itself must increase to drive the aggregation process that leads to a solid material. Interestingly, previous work on rMfp-1 did not examine if the shift in pH alone without metals increases adhesion [40], so it may be the case that this effect too could be observed in rMfp-1, although due to DOPA-oxidation at neutral pH it may be affected irreversibly due to covalent crosslinks. Interestingly, there is evidence that even in Mfp-1 there are inter/intra molecular interactions related to aromatics like cation-π and π-π stacking that are playing a role in improving its cohesion [146], and which may be playing a role in Mfp-17 as well as observed in the Raman spectra of solid Mfp-17. The significant deposition of aromatics in Mfp-17 perhaps also influences the solidification process and potentially enhance the material's cohesion as pH shifts from neutral to basic conditions

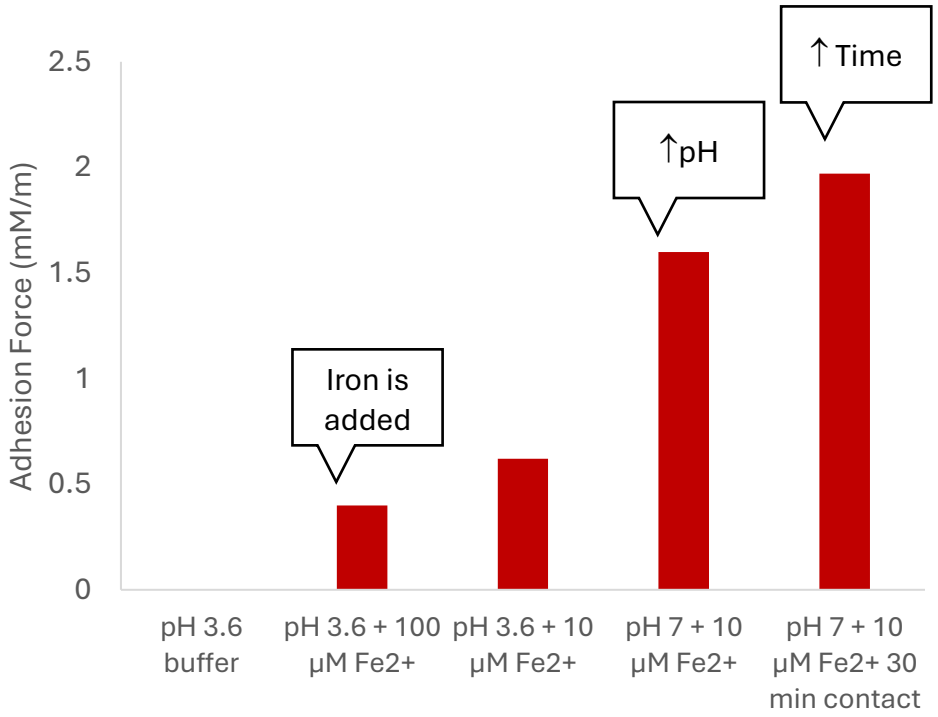

Figure 38. Mfp-17's surface adhesion force is demonstrated through the experimental progression showing an increase in adhesion as iron is introduced, pH is increased, and contact time is longer between the symmetric Mfp-17-coated mica surfaces.

6. Conclusion

In this thesis, it was sought to characterize the potential that cysteine-rich Mfps have as a building block of the cuticle's matrix within marine mussels' byssal threads. The heterologous production of putative cuticle-derived cysteine-rich proteins Mfp-16 and Mfp-17 was achieved in *E. coli* bacteria, which opened the path to characterize them. These proteins were hypothesized to be 1) strong reducing agents, 2) capable of iron-cysteine coordination, and 3) capable of supporting liquid-liquid phase separation with mussel-derived protein counterparts based on their purported roles in the byssus' cuticle. The results presented in this work are evidence that indeed these proteins are capable reducing agents at pH levels relevant to their natural context (acidic to neutral conditions), strongly suggesting that they are the building blocks that maintain the cuticle under a reducing poise that can keep DOPA's catechol functional groups reduced and active for metal-coordination. Furthermore, through various spectroscopic techniques, signatures supporting iron-cysteine coordination by Mfp-17 were measured. For the first time, evidence that begins to elucidate how cysteine and iron are interacting in the byssal thread's cuticle was acquired. Although the mechanisms of which are not yet fully understood, the results suggest the iron-coordination by Mfp-17 is promiscuous, which might be a sacrifice to enhance binding affinity. These bonds appear to influence the cohesiveness of the material, potentially playing a mechanical role in the cuticle. The cysteine-rich cuticle Mfps also demonstrated a pH-triggered solidification process when transitioning from acidic to neutral conditions, mimicking the thread's natural transition from liquid protein vesicles to a solid thread. The proteins also appear to support liquid-liquid phase separation in Mfp-1, which in the future may assist in explaining the phase separation observed in the mature thread's cuticle and its protein vesicles. The outcome of this work has significant implications for the future potential of Mfp-17 to be used as a material in applications where iron sequestration is desired given its ability to create a solid-state biopolymer capable of iron-coordination, or alternatively, as an antioxidant that is effective across a wide pH range. Mfp-17's amino acid sequence could also present valuable sequence patterns that could be extracted for engineering proteins with similar functions in the future.

7. Appendices

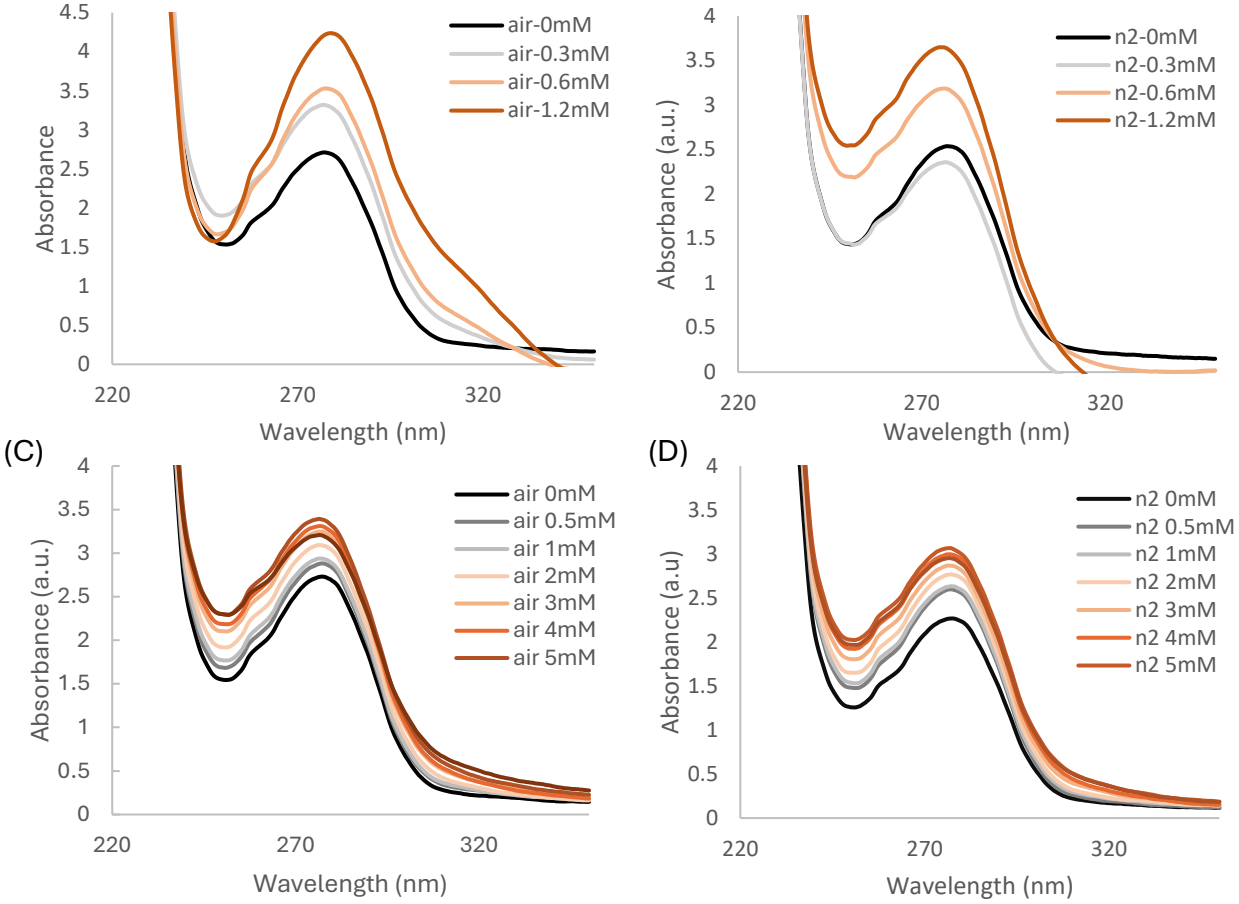

Appendix A – UV-Vis light absorbance spectra of Mfp-17 (30 µM) with increasing concentrations of $FeCl_2$ and $FeCl_3$ in 0.1M pH 3.6 buffer conditions with air and without air (nitrogen purged). A,B) Absorbance spectra of Mfp-17 with increasing iron (III) chloride concentration in buffer with air (A) and without air (B). C,D) Absorbance spectra of Mfp-17 with increasing iron (II) chloride concentration in buffer with air (A) and without air (B).

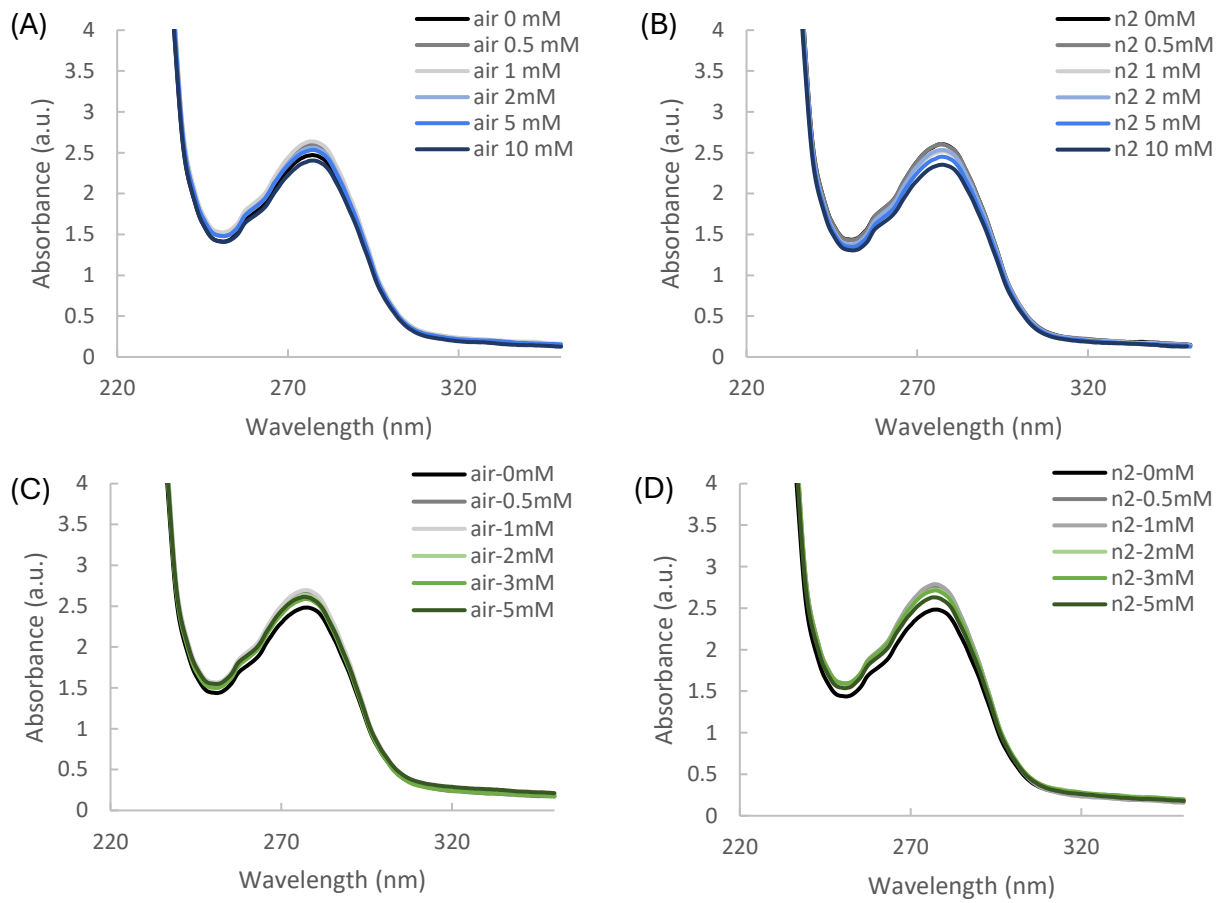

Appendix B – UV-Vis light absorbance spectra of Mfp-17 (30 µM) with increasing concentrations of ZnAc and $NiCl_2$ in 0.1M pH 3.6 buffer conditions with air and without air (nitrogen purged). A,B) Absorbance spectra of Mfp-17 with increasing zinc acetate concentration in buffer with air (A) and without air (B). C,D) Absorbance spectra of Mfp-17 with increasing nickel chloride concentration in buffer with air (A) and without air (B).

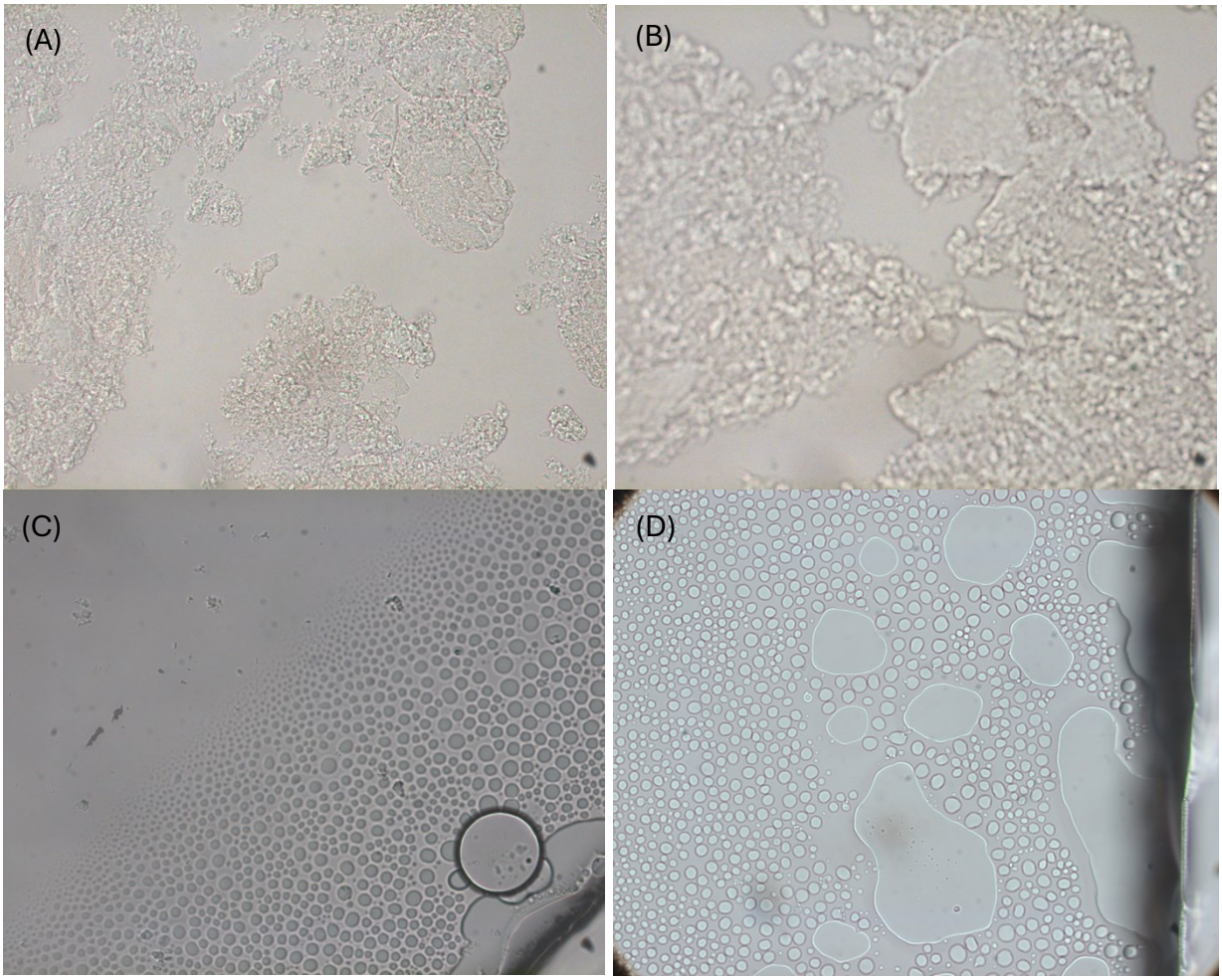

Appendix C - Light microscopy images of rfmp-1 and Mfp-16 coacervation attempt at a 1:1 ration at pH 7.0 and 500 mM NaCl. A,B) Protein precipitation at pH 7.0 upon the addition of salt. C, D) Simple coacervation of rMfp-1 in the same conditions (pH 7.0, 500 mM NaCl).

8. References

[1] N. Amzallag, "From metallurgy to Bronze Age civilizations: the synthetic theory," *American Journal of Archaeology,* vol. 113, no. 4, pp. 497-519, 2009.

[2] V. G. Childe, "The Bronze Age," *Past & Present,* no. 12, pp. 2-15, 1957.

[3] R. C. Thompson, S. H. Swan, C. J. Moore, and F. S. Vom Saal, "Our plastic age," vol. 364, ed: The Royal Society Publishing, 2009, pp. 1973-1976.

[4] A. B. Fowler, "A semicentury of semiconductors," *Physics Today,* vol. 46, no. 10, pp. 59-62, 1993.

[5] K. Y. Kamal, "The Silicon Age: Trends in Semiconductor Devices Industry," *Journal of Engineering Science & Technology Review,* vol. 15, no. 1, 2022.

[6] A. M. Anton, A. Heidebrecht, N. Mahmood, M. Beiner, T. Scheibel, and F. Kremer, "Foundation of the outstanding toughness in biomimetic and natural spider silk," *Biomacromolecules,* vol. 18, no. 12, pp. 3954-3962, 2017.

[7] M. Heim, D. Keerl, and T. Scheibel, "Spider silk: from soluble protein to extraordinary fiber," *Angewandte Chemie International Edition,* vol. 48, no. 20, pp. 3584-3596, 2009.

[8] M. J. Harrington and J. H. Waite, "Holdfast heroics: comparing the molecular and mechanical properties of Mytilus californianus byssal threads," *Journal of Experimental Biology,* vol. 210, no. 24, pp. 4307-4318, 2007.

[9] J. H. Waite and M. J. Harrington, "Following the thread: Mytilus mussel byssus as an inspired multi-functional biomaterial," *Canadian Journal of Chemistry,* vol. 100, no. 3, pp. 197-211, 2022.

[10] M. J. Harrington, F. Jehle, and T. Priemel, "Mussel byssus structure-function and fabrication as inspiration for biotechnological production of advanced materials," *Biotechnology Journal,* vol. 13, no. 12, p. 1800133, 2018.

[11] Y.-H. P. Zhang, J. Sun, and Y. Ma, "Biomanufacturing: history and perspective," *Journal of Industrial Microbiology and Biotechnology,* vol. 44, no. 4-5, pp. 773-784, 2017.

[12] J. M. Clomburg, A. M. Crumbley, and R. Gonzalez, "Industrial biomanufacturing: the future of chemical production," *Science,* vol. 355, no. 6320, p. aag0804, 2017.

[13] T. Priemel, E. Degtyar, M. N. Dean, and M. J. Harrington, "Rapid self-assembly of complex biomolecular architectures during mussel byssus biofabrication," *Nature Communications,* vol. 8, no. 1, pp. 1-12, 2017.

[14] B. P. Lee, P. B. Messersmith, J. N. Israelachvili, and J. H. Waite, "Mussel-inspired adhesives and coatings," *Annual review of materials research,* vol. 41, pp. 99-132, 2011.

[15] J. H. Waite, "Mussel adhesion–essential footwork," *Journal of Experimental Biology,* vol. 220, no. 4, pp. 517-530, 2017.

[16] M. J. Harrington, A. Masic, N. Holten-Andersen, J. H. Waite, and P. Fratzl, "Iron-clad fibers: a metal-based biological strategy for hard flexible coatings," *Science,* vol. 328, no. 5975, pp. 216-220, 2010.

[17] E. Khare, N. Holten-Andersen, and M. J. Buehler, "Transition-metal coordinate bonds for bioinspired macromolecules with tunable mechanical properties," *Nature Reviews Materials,* vol. 6, no. 5, pp. 421-436, 2021.

[18] A. Tamarin, P. Lewis, and J. Askey, "The structure and formation of the byssus attachment plaque in Mytilus," *Journal of morphology,* vol. 149, no. 2, pp. 199-221, 1976.

[19] L. V. Zuccarello, "The collagen gland of Mytilus galloprovincialis: an ultrastructural and cytochemical study on secretory granules," *Journal of ultrastructure research,* vol. 73, no. 2, pp. 135-147, 1980.
[20] L. V. Zuccarello, "Ultrastructural and cytochemical study on the enzyme gland of the foot of a mollusc," *Tissue and Cell,* vol. 13, no. 4, pp. 701-713, 1981.
[21] J. H. WAITE, "Adhesion in byssally attached bivalves," *Biological Reviews,* vol. 58, no. 2, pp. 209-231, 1983.
[22] T. Priemel *et al.*, "Microfluidic-like fabrication of metal ion–cured bioadhesives by mussels," *Science,* vol. 374, no. 6564, pp. 206-211, 2021.
[23] F. Jehle, T. Priemel, M. Strauss, P. Fratzl, L. Bertinetti, and M. J. Harrington, "Collagen pentablock copolymers form smectic liquid crystals as precursors for mussel byssus fabrication," *ACS nano,* vol. 15, no. 4, pp. 6829-6838, 2021. [Online]. Available: https://pubs.acs.org/doi/10.1021/acsnano.0c10457.
[24] M. Renner-Rao, M. Clark, and M. J. Harrington, "Fiber formation from liquid crystalline collagen vesicles isolated from mussels," *Langmuir,* vol. 35, no. 48, pp. 15992-16001, 2019.
[25] F. Jehle, E. Macías-Sánchez, S. Sviben, P. Fratzl, L. Bertinetti, and M. J. Harrington, "Hierarchically-structured metalloprotein composite coatings biofabricated from co-existing condensed liquid phases," *Nature communications,* vol. 11, no. 1, pp. 1-9, 2020.
[26] N. Holten-Andersen, G. E. Fantner, S. Hohlbauch, J. H. Waite, and F. W. Zok, "Protective coatings on extensible biofibres," *Nature materials,* vol. 6, no. 9, pp. 669-672, 2007.
[27] M. Renner-Rao *et al.*, "Mussels fabricate porous glues via multiphase liquid–liquid phase separation of multiprotein condensates," *ACS nano,* vol. 16, no. 12, pp. 20877-20890, 2022.
[28] A. Reinecke, G. Brezesinski, and M. J. Harrington, "pH-Responsive Self-Organization of Metal-Binding Protein Motifs from Biomolecular Junctions in Mussel Byssus," *Advanced Materials Interfaces,* vol. 4, no. 1, p. 1600416, 2017.
[29] N. R. Martinez Rodriguez, S. Das, Y. Kaufman, J. N. Israelachvili, and J. H. Waite, "Interfacial pH during mussel adhesive plaque formation," *Biofouling,* vol. 31, no. 2, pp. 221-227, 2015.
[30] H. Kim *et al.*, "Essential Role of Thiols in Maintaining Stable Catecholato-Iron Complexes in Condensed Materials," *Chemistry of Materials,* 2022.
[31] T. Priemel, R. Palia, M. Babych, C. J. Thibodeaux, S. Bourgault, and M. J. Harrington, "Compartmentalized processing of catechols during mussel byssus fabrication determines the destiny of DOPA," *Proceedings of the National Academy of Sciences,* vol. 117, no. 14, pp. 7613-7621, 2020.
[32] J. Yu, W. Wei, E. Danner, R. K. Ashley, J. N. Israelachvili, and J. H. Waite, "Mussel protein adhesion depends on interprotein thiol-mediated redox modulation," *Nature chemical biology,* vol. 7, no. 9, pp. 588-590, 2011.
[33] N. Holten-Andersen, T. E. Mates, M. S. Toprak, G. D. Stucky, F. W. Zok, and J. H. Waite, "Metals and the integrity of a biological coating: the cuticle of mussel byssus," *Langmuir,* vol. 25, no. 6, pp. 3323-3326, 2009.
[34] N. Holten-Andersen, H. Zhao, and J. H. Waite, "Stiff coatings on compliant biofibers: the cuticle of Mytilus californianus byssal threads," *Biochemistry,* vol. 48, no. 12, pp. 2752-2759, 2009.

[35] C. V. Benedict and J. H. Waite, "Location and analysis of byssal structural proteins of Mytilus edulis," *Journal of morphology,* vol. 189, no. 2, pp. 171-181, 1986.
[36] J. H. Waite, T. J. Housley, and M. L. Tanzer, "Peptide repeats in a mussel glue protein: theme and variations," *Biochemistry,* vol. 24, no. 19, pp. 5010-5014, 1985.
[37] C. Sun and J. H. Waite, "Mapping chemical gradients within and along a fibrous structural tissue, mussel byssal threads," *Journal of Biological Chemistry,* vol. 280, no. 47, pp. 39332-39336, 2005.
[38] S. W. Taylor, D. B. Chase, M. H. Emptage, M. J. Nelson, and J. H. Waite, "Ferric ion complexes of a DOPA-containing adhesive protein from Mytilus edulis," *Inorganic Chemistry,* vol. 35, no. 26, pp. 7572-7577, 1996.
[39] C. N. Schmitt, A. Winter, L. Bertinetti, A. Masic, P. Strauch, and M. J. Harrington, "Mechanical homeostasis of a DOPA-enriched biological coating from mussels in response to metal variation," *Journal of the Royal Society Interface,* vol. 12, no. 110, p. 20150466, 2015.
[40] M. Mesko, L. Xiang, S. Bohle, D. S. Hwang, H. Zeng, and M. J. Harrington, "Catechol-Vanadium Binding Enhances Cross-Linking and Mechanics of a Mussel Byssus Coating Protein," *Chemistry of Materials,* vol. 33, no. 16, pp. 6530-6540, 2021.
[41] M. J. Sever and J. J. Wilker, "Absorption spectroscopy and binding constants for first-row transition metal complexes of a DOPA-containing peptide," *Dalton Transactions,* no. 6, pp. 813-822, 2006.
[42] Z. Xu, "Mechanics of metal-catecholate complexes: The roles of coordination state and metal types," *Scientific reports,* vol. 3, no. 1, p. 2914, 2013.
[43] H. Xu *et al.*, "Competition between oxidation and coordination in cross-linking of polystyrene copolymer containing catechol groups," *ACS Macro Letters,* vol. 1, no. 4, pp. 457-460, 2012.
[44] N. Holten-Andersen *et al.*, "pH-induced metal-ligand cross-links inspired by mussel yield self-healing polymer networks with near-covalent elastic moduli," *Proceedings of the National Academy of Sciences,* vol. 108, no. 7, pp. 2651-2655, 2011.
[45] J. H. Waite, "The phylogeny and chemical diversity of quinone-tanned glues and varnishes," *Comparative Biochemistry and Physiology Part B: Comparative Biochemistry,* vol. 97, no. 1, pp. 19-29, 1990.
[46] N. Holten-Andersen *et al.*, "Metal-coordination: using one of nature's tricks to control soft material mechanics," *Journal of Materials Chemistry B,* vol. 2, no. 17, pp. 2467-2472, 2014.
[47] D. G. DeMartini, J. M. Errico, S. Sjoestroem, A. Fenster, and J. H. Waite, "A cohort of new adhesive proteins identified from transcriptomic analysis of mussel foot glands," *Journal of the Royal Society Interface,* vol. 14, no. 131, p. 20170151, 2017.
[48] E. Valois, C. Hoffman, D. G. Demartini, and J. H. Waite, "The thiol-rich interlayer in the shell/core architecture of mussel byssal threads," *Langmuir,* vol. 35, no. 48, pp. 15985-15991, 2019.
[49] Y. Jin, H. Kong, X. Zhou, G. Li, and J. Du, "Design and characterization of sheet-based gyroid porous structures with bioinspired functional gradients," *Materials,* vol. 13, no. 17, p. 3844, 2020.
[50] A. Yánez, A. Cuadrado, O. Martel, H. Afonso, and D. Monopoli, "Gyroid porous titanium structures: A versatile solution to be used as scaffolds in bone defect reconstruction," *Materials & Design,* vol. 140, pp. 21-29, 2018.

[51] J. Wang and T. Scheibel, "Recombinant production of mussel byssus inspired proteins," *Biotechnology Journal,* vol. 13, no. 12, p. 1800146, 2018.
[52] C. E. Sing and S. L. Perry, "Recent progress in the science of complex coacervation," *Soft Matter,* vol. 16, no. 12, pp. 2885-2914, 2020.
[53] S. Kim *et al.*, "Salt triggers the simple coacervation of an underwater adhesive when cations meet aromatic π electrons in seawater," *ACS nano,* vol. 11, no. 7, pp. 6764-6772, 2017.
[54] Y. Shin and C. P. Brangwynne, "Liquid phase condensation in cell physiology and disease," *Science,* vol. 357, no. 6357, p. eaaf4382, 2017.
[55] H. J. Kim, B. Yang, T. Y. Park, S. Lim, and H. J. Cha, "Complex coacervates based on recombinant mussel adhesive proteins: their characterization and applications," *Soft matter,* vol. 13, no. 42, pp. 7704-7716, 2017.
[56] S. Lim, Y. S. Choi, D. G. Kang, Y. H. Song, and H. J. Cha, "The adhesive properties of coacervated recombinant hybrid mussel adhesive proteins," *Biomaterials,* vol. 31, no. 13, pp. 3715-3722, 2010.
[57] Y. S. Choi, D. G. Kang, S. Lim, Y. J. Yang, C. S. Kim, and H. J. Cha, "Recombinant mussel adhesive protein fp-5 (MAP fp-5) as a bulk bioadhesive and surface coating material," *Biofouling,* vol. 27, no. 7, pp. 729-737, 2011.
[58] D. R. Miller, S. Das, K.-Y. Huang, S. Han, J. N. Israelachvili, and J. H. Waite, "Mussel coating protein-derived complex coacervates mitigate frictional surface damage," *ACS Biomaterials Science & Engineering,* vol. 1, no. 11, pp. 1121-1128, 2015.
[59] K.-Y. Huang, H. Y. Yoo, Y. Jho, S. Han, and D. S. Hwang, "Bicontinuous fluid structure with low cohesive energy: molecular basis for exceptionally low interfacial tension of complex coacervate fluids," *Acs Nano,* vol. 10, no. 5, pp. 5051-5062, 2016.
[60] D. A. Dougherty, "The cation− π interaction," *Accounts of chemical research,* vol. 46, no. 4, pp. 885-893, 2013.
[61] S. Kim *et al.*, "Complexation and coacervation of like-charged polyelectrolytes inspired by mussels," *Proceedings of the National Academy of Sciences,* vol. 113, no. 7, pp. E847-E853, 2016.
[62] E. Spruijt, J. Sprakel, M. A. C. Stuart, and J. van der Gucht, "Interfacial tension between a complex coacervate phase and its coexisting aqueous phase," *Soft Matter,* vol. 6, no. 1, pp. 172-178, 2010.
[63] J. Qin *et al.*, "Interfacial tension of polyelectrolyte complex coacervate phases," *ACS Macro Letters,* vol. 3, no. 6, pp. 565-568, 2014.
[64] Y. Jho, H. Y. Yoo, Y. Lin, S. Han, and D. S. Hwang, "Molecular and structural basis of low interfacial energy of complex coacervates in water," *Advances in Colloid and Interface Science,* vol. 239, pp. 61-73, 2017.
[65] S. Lim, D. Moon, H. J. Kim, J. H. Seo, I. S. Kang, and H. J. Cha, "Interfacial tension of complex coacervated mussel adhesive protein according to the Hofmeister series," *Langmuir,* vol. 30, no. 4, pp. 1108-1115, 2014.
[66] E. Valois, R. Mirshafian, and J. H. Waite, "Phase-dependent redox insulation in mussel adhesion," *Science advances,* vol. 6, no. 23, p. eaaz6486, 2020.
[67] S. C. Nicklisch and J. H. Waite, "Optimized DPPH assay in a detergent-based buffer system for measuring antioxidant activity of proteins," *MethodsX,* vol. 1, pp. 233-238, 2014.

[68] S. C. Nicklisch, S. Das, N. R. Martinez Rodriguez, J. H. Waite, and J. N. Israelachvili, "Antioxidant efficacy and adhesion rescue by a recombinant mussel foot protein-6," *Biotechnology progress,* vol. 29, no. 6, pp. 1587-1593, 2013.
[69] S. F. Jordan *et al.*, "Spontaneous assembly of redox-active iron-sulfur clusters at low concentrations of cysteine," *Nature communications,* vol. 12, no. 1, p. 5925, 2021.
[70] J. C. Crack and N. E. Le Brun, "Biological iron-sulfur clusters: Mechanistic insights from mass spectrometry," *Coordination Chemistry Reviews,* vol. 448, p. 214171, 2021.
[71] B. Srour, S. Gervason, B. Monfort, and B. D'Autréaux, "Mechanism of iron–sulfur cluster assembly: In the intimacy of iron and sulfur encounter," *Inorganics,* vol. 8, no. 10, p. 55, 2020.
[72] M. Capdevila, R. Bofill, O. Palacios, and S. Atrian, "State-of-the-art of metallothioneins at the beginning of the 21st century," *Coordination Chemistry Reviews,* vol. 256, no. 1-2, pp. 46-62, 2012.
[73] B. Ruttkay-Nedecky *et al.*, "The role of metallothionein in oxidative stress," *International journal of molecular sciences,* vol. 14, no. 3, pp. 6044-6066, 2013.
[74] S. G. Bell and B. L. Vallee, "The metallothionein/thionein system: an oxidoreductive metabolic zinc link," *Chembiochem,* vol. 10, no. 1, pp. 55-62, 2009.
[75] A. Krezel and W. Maret, "The bioinorganic chemistry of mammalian metallothioneins," *Chemical reviews,* vol. 121, no. 23, pp. 14594-14648, 2021.
[76] M. Good and M. Vasak, "Iron (II)-substituted metallothionein: evidence for the existence of iron-thiolate clusters," *Biochemistry,* vol. 25, no. 26, pp. 8353-8356, 1986.
[77] N. Kojima, C. R. Young, and G. W. Bates, "Failure of metallothionein to bind iron or act as an iron mobilizing agent," *Biochimica et Biophysica Acta (BBA)-General Subjects,* vol. 716, no. 2, pp. 273-275, 1982.
[78] M. T. Werth and M. K. Johnson, "Magnetic circular dichroism and electron paramagnetic resonance studies of iron (II)-metallothionein," *Biochemistry,* vol. 28, no. 9, pp. 3982-3988, 1989.
[79] X. Ding, E. Bill, M. Good, A. X. Trautwein, and M. Vašak, "Mössbauer studies on the metal-thiolate cluster formation in Fe (II)-metallothionein," *European journal of biochemistry,* vol. 171, no. 3, pp. 711-714, 1988.
[80] Y. Sano, A. Onoda, R. Sakurai, H. Kitagishi, and T. Hayashi, "Preparation and reactivity of a tetranuclear Fe (II) core in the metallothionein α-domain," *Journal of Inorganic Biochemistry,* vol. 105, no. 5, pp. 702-708, 2011.
[81] A. G. Dickson, "The measurement of sea water pH," *Marine chemistry,* vol. 44, no. 2-4, pp. 131-142, 1993.
[82] G. M. Marion, F. J. Millero, M. F. Camões, P. Spitzer, R. Feistel, and C.-T. Chen, "pH of seawater," *Marine Chemistry,* vol. 126, no. 1-4, pp. 89-96, 2011.
[83] K. M. Makwana and R. Mahalakshmi, "Implications of aromatic–aromatic interactions: From protein structures to peptide models," *Protein Science,* vol. 24, no. 12, pp. 1920-1933, 2015.
[84] K. Mandal, B. Chakrabarti, J. Thomson, and R. Siezen, "Structure and stability of gamma-crystallins. Denaturation and proteolysis behavior," *Journal of Biological Chemistry,* vol. 262, no. 17, pp. 8096-8102, 1987.
[85] K. Reid, P. Lindley, and J. Thornton, "Sulphur-aromatic interactions in proteins," *FEBS letters,* vol. 190, no. 2, pp. 209-213, 1985.

[86] D. Bagchi, A. Maity, S. K. De, and A. Chakraborty, "Effect of metal ions on the intrinsic blue fluorescence property and morphology of aromatic amino acid self-assembly," *The Journal of Physical Chemistry B,* vol. 125, no. 45, pp. 12436-12445, 2021.
[87] S. Prakash, M. Sundd, and P. Guptasarma, "The key to the extraordinary thermal stability of P. furiosus holo-rubredoxin: Iron binding-guided packing of a core aromatic cluster responsible for high kinetic stability of the native structure," *PloS one,* vol. 9, no. 3, p. e89703, 2014.
[88] C. K. Riener, G. Kada, and H. J. Gruber, "Quick measurement of protein sulfhydryls with Ellman's reagent and with 4, 4′-dithiodipyridine," *Analytical and bioanalytical chemistry,* vol. 373, pp. 266-276, 2002.
[89] T. McIlvaine, "A buffer solution for colorimetric comparison," *J. biol. Chem,* vol. 49, no. 1, pp. 183-186, 1921.
[90] M. Zhao, X. Y. Tao, F. Q. Wang, Y. H. Ren, and D. Z. Wei, "Establishment of a low-dosage-IPTG inducible expression system construction method in Escherichia coli," *Journal of basic microbiology,* vol. 58, no. 9, pp. 806-810, 2018.
[91] J. X. Yan, W. C. Kett, B. R. Herbert, A. A. Gooley, N. H. Packer, and K. L. Williams, "Identification and quantitation of cysteine in proteins separated by gel electrophoresis," *Journal of Chromatography A,* vol. 813, no. 1, pp. 187-200, 1998.
[92] L. C. Lane, "A simple method for stabilizing protein-sulfhydryl groups during SDS-gel electrophoresis," *Analytical biochemistry,* vol. 86, no. 2, pp. 655-664, 1978.
[93] H. Block *et al.*, "Immobilized-metal affinity chromatography (IMAC): a review," *Methods in enzymology,* vol. 463, pp. 439-473, 2009.
[94] S. C. Nicklisch, J. E. Spahn, H. Zhou, C. M. Gruian, and J. H. Waite, "Redox capacity of an extracellular matrix protein associated with adhesion in Mytilus californianus," *Biochemistry,* vol. 55, no. 13, pp. 2022-2030, 2016.
[95] P. W. Riddles, R. L. Blakeley, and B. Zerner, "[8] Reassessment of Ellman's reagent," in *Methods in enzymology*, vol. 91: Elsevier, 1983, pp. 49-60.
[96] C. R. Borges and N. D. Sherma, "Techniques for the analysis of cysteine sulfhydryls and oxidative protein folding," *Antioxidants & redox signaling,* vol. 21, no. 3, pp. 511-531, 2014.
[97] J. H. Waite and M. L. Tanzer, "Polyphenolic substance of Mytilus edulis: novel adhesive containing L-dopa and hydroxyproline," *Science,* vol. 212, no. 4498, pp. 1038-1040, 1981.
[98] L. B. Poole, "The basics of thiols and cysteines in redox biology and chemistry," *Free Radical Biology and Medicine,* vol. 80, pp. 148-157, 2015.
[99] B. Alvarez and G. Salinas, "Basic concepts of thiol chemistry and biology," in *Redox Chemistry and Biology of Thiols*: Elsevier, 2022, pp. 1-18.
[100] S. Portillo-Ledesma *et al.*, "Deconstructing the catalytic efficiency of peroxiredoxin-5 peroxidatic cysteine," *Biochemistry,* vol. 53, no. 38, pp. 6113-6125, 2014.
[101] G. Ferrer-Sueta, "Chemical basis of cysteine reactivity and specificity: Acidity and nucleophilicity," in *Redox Chemistry and Biology of Thiols*: Elsevier, 2022, pp. 19-58.
[102] S. M. Marino and V. N. Gladyshev, "Cysteine function governs its conservation and degeneration and restricts its utilization on protein surfaces," *Journal of molecular biology,* vol. 404, no. 5, pp. 902-916, 2010.

[103] S. M. Marino, G. Salinas, and V. N. Gladyshev, "Computational functional analysis of cysteine residues in proteins," in *Redox Chemistry and Biology of Thiols*: Elsevier, 2022, pp. 59-80.
[104] P. W. Riddles, R. L. Blakeley, and B. Zerner, "Ellman's reagent: 5, 5′-dithiobis (2-nitrobenzoic acid)—a reexamination," *Analytical biochemistry,* vol. 94, no. 1, pp. 75-81, 1979.
[105] D. B. Hunsaker Jr and G. H. Schenk, "The determination of thiols with diphenylpicrylhydrazyl as a spectrophotometric reagent," *Talanta,* vol. 30, no. 7, pp. 475-480, 1983.
[106] J. J. Warren, J. R. Winkler, and H. B. Gray, "Redox properties of tyrosine and related molecules," *FEBS letters,* vol. 586, no. 5, pp. 596-602, 2012.
[107] J. R. Winkler and H. B. Gray, "Could tyrosine and tryptophan serve multiple roles in biological redox processes?," *Philosophical Transactions of the Royal Society A: Mathematical, Physical and Engineering Sciences,* vol. 373, no. 2037, p. 20140178, 2015.
[108] A. Harriman, "Further comments on the redox potentials of tryptophan and tyrosine," *Journal of Physical Chemistry,* vol. 91, no. 24, pp. 6102-6104, 1987.
[109] S. Ye, L. Wei, D. Tang, P. Sun, M. Bartlam, and Z. Rao, "An insight into the mechanism of human cysteine dioxygenase: key roles of the thioether-bonded tyrosine-cysteine cofactor," *Journal of Biological Chemistry,* vol. 282, no. 5, pp. 3391-3402, 2007.
[110] L. C. Kühn, "Iron regulatory proteins and their role in controlling iron metabolism," *Metallomics,* vol. 7, no. 2, pp. 232-243, 2015.
[111] R. D. Palmiter, "The elusive function of metallothioneins," *Proceedings of the National Academy of Sciences,* vol. 95, no. 15, pp. 8428-8430, 1998.
[112] R. Dallinger, Y. Wang, B. Berger, E. A. Mackay, and J. H. Kägi, "Spectroscopic characterization of metallothionein from the terrestrial snail, Helix pomatia," *European Journal of Biochemistry,* vol. 268, no. 15, pp. 4126-4133, 2001.
[113] R. M. Nezhad, A. Shahpiri, and A. Mirlohi, "Heterologous expression and metal-binding characterization of a type 1 metallothionein isoform (OsMTI-1b) from rice (Oryza sativa)," *The Protein Journal,* vol. 32, pp. 131-137, 2013.
[114] L. Duan, J.-J. Kong, T.-Q. Wang, and Y. Sun, "Binding of Cd (II), Pb (II), and Zn (II) to a type 1 metallothionein from maize (Zea mays)," *Biometals,* vol. 31, pp. 539-550, 2018.
[115] B. Weber, R. Betz, W. Bauer, and S. Schlamp, "Crystal structure of iron (II) acetate," ed: Wiley Online Library, 2011.
[116] X. Wan and E. Freisinger, "The plant metallothionein 2 from Cicer arietinum forms a single metal–thiolate cluster," *Metallomics,* vol. 1, no. 6, pp. 489-500, 2009.
[117] A. M. Silva, X. Kong, M. C. Parkin, R. Cammack, and R. C. Hider, "Iron (III) citrate speciation in aqueous solution," *Dalton Transactions,* no. 40, pp. 8616-8625, 2009.
[118] M. Ilbert and V. Bonnefoy, "Insight into the evolution of the iron oxidation pathways," *Biochimica et Biophysica Acta (BBA)-Bioenergetics,* vol. 1827, no. 2, pp. 161-175, 2013.
[119] J. Chastain and R. C. King Jr, "Handbook of X-ray photoelectron spectroscopy," *Perkin-Elmer Corporation,* vol. 40, p. 221, 1992.
[120] T. Yamashita and P. Hayes, "Analysis of XPS spectra of Fe2+ and Fe3+ ions in oxide materials," *Applied surface science,* vol. 254, no. 8, pp. 2441-2449, 2008.

[121] M. Aronniemi, J. Sainio, and J. Lahtinen, "XPS study on the correlation between chemical state and oxygen-sensing properties of an iron oxide thin film," *Applied Surface Science,* vol. 253, no. 24, pp. 9476-9482, 2007.
[122] M. C. Biesinger, B. P. Payne, A. P. Grosvenor, L. W. Lau, A. R. Gerson, and R. S. C. Smart, "Resolving surface chemical states in XPS analysis of first row transition metals, oxides and hydroxides: Cr, Mn, Fe, Co and Ni," *Applied Surface Science,* vol. 257, no. 7, pp. 2717-2730, 2011.
[123] K. Doi, B. C. Antanaitis, and P. Aisen, "The binuclear iron centers of uteroferrin and the purple acid phosphatases," in *Bioinorganic Chemistry*: Springer, 2005, pp. 1-26.
[124] V. Secchi *et al.*, "Self-assembling behavior of cysteine-modified oligopeptides: an XPS and NEXAFS study," *The Journal of Physical Chemistry C,* vol. 122, no. 11, pp. 6236-6239, 2018.
[125] L. N. Kramer and M. P. Klein, "XPS OP NON-HEME IRON PROTEINS. INVESTIGATION OF THE IRON-SULFUR MOEITY IN NON-HEME IRON PROTEINS BY MEANS OF X-RAY PHOTOELECTRON SPECTROSCOPY," 1971.
[126] C. Gleitzer, J. Goodenough, B. Hyde, M. O'Keeffe, U. Weser, and U. Weser, "Redox reactions of sulphur-containing amino-acid residues in proteins and metalloproteins, an XPS study," *Cation Ordering and Electron Transfer,* pp. 145-160, 1985.
[127] M. Kremer, "Mechanism of the Fenton reaction. Evidence for a new intermediate," *Physical Chemistry Chemical Physics,* vol. 1, no. 15, pp. 3595-3605, 1999.
[128] A. Rygula, K. Majzner, K. M. Marzec, A. Kaczor, M. Pilarczyk, and M. Baranska, "Raman spectroscopy of proteins: a review," *Journal of Raman Spectroscopy,* vol. 44, no. 8, pp. 1061-1076, 2013.
[129] A. Torreggiani and A. Tinti, "Raman spectroscopy a promising technique for investigations of metallothioneins," *Metallomics,* vol. 2, no. 4, pp. 246-260, 2010.
[130] S. Todorovic and M. Teixeira, "Resonance Raman spectroscopy of Fe–S proteins and their redox properties," *JBIC Journal of Biological Inorganic Chemistry,* vol. 23, no. 4, pp. 647-661, 2018.
[131] F. Madzharova, Z. Heiner, and J. Kneipp, "Surface enhanced hyper-Raman scattering of the amino acids tryptophan, histidine, phenylalanine, and tyrosine," *The Journal of Physical Chemistry C,* vol. 121, no. 2, pp. 1235-1242, 2017.
[132] B. Hernández, F. Pflüger, S. G. Kruglik, and M. Ghomi, "Characteristic Raman lines of phenylalanine analyzed by a multiconformational approach," *Journal of Raman Spectroscopy,* vol. 44, no. 6, pp. 827-833, 2013.
[133] A. Ajayaghosh and S. J. George, "First phenylenevinylene based organogels: self-assembled nanostructures via cooperative hydrogen bonding and π-stacking," *Journal of the American Chemical Society,* vol. 123, no. 21, pp. 5148-5149, 2001.
[134] E. Gazit, "A possible role for π-stacking in the self-assembly of amyloid fibrils," *The FASEB Journal,* vol. 16, no. 1, pp. 77-83, 2002.
[135] M. L. Waters, "Aromatic interactions in peptides: impact on structure and function," *Peptide Science: Original Research on Biomolecules,* vol. 76, no. 5, pp. 435-445, 2004.
[136] R. Azriel and E. Gazit, "Analysis of the minimal amyloid-forming fragment of the islet amyloid polypeptide," *Journal of Biological Chemistry,* vol. 276, no. 36, pp. 34156-34161, 2001.

[137] Y. Porat, A. Stepensky, F. X. Ding, F. Naider, and E. Gazit, "Completely different amyloidogenic potential of nearly identical peptide fragments," *Biopolymers: Original Research on Biomolecules,* vol. 69, no. 2, pp. 161-164, 2003.
[138] A. A. Profit, V. Felsen, J. Chinwong, E. R. E. Mojica, and R. Z. Desamero, "Evidence of π-stacking interactions in the self-assembly of hIAPP22-29," *Proteins: Structure, Function, and Bioinformatics,* vol. 81, no. 4, pp. 690-703, 2013.
[139] R. P. Rava and T. G. Spiro, "Resonance enhancement in the ultraviolet Raman spectra of aromatic amino acids," *The Journal of Physical Chemistry,* vol. 89, no. 10, pp. 1856-1861, 1985.
[140] S. A. Asher, M. Ludwig, and C. R. Johnson, "UV resonance Raman excitation profiles of the aromatic amino acids," *Journal of the American Chemical Society,* vol. 108, no. 12, pp. 3186-3197, 1986.
[141] S. D. Zarić, D. M. Popović, and E. W. Knapp, "Metal ligand aromatic cation–π interactions in metalloproteins: ligands coordinated to metal interact with aromatic residues," *Chemistry–A European Journal,* vol. 6, no. 21, pp. 3935-3942, 2000.
[142] H. Peifeng, C. Sorensen, and M. L. Gross, "Influences of peptide side chains on the metal ion binding site in metal ion-cationized peptides: Participation of aromatic rings in metal chelation," *Journal of the American Society for Mass Spectrometry,* vol. 6, no. 11, pp. 1079-1085, 1995.
[143] J. A. Hunt and C. A. Fierke, "Selection of carbonic anhydrase variants displayed on phage: aromatic residues in zinc binding site enhance metal affinity and equilibration kinetics," *Journal of Biological Chemistry,* vol. 272, no. 33, pp. 20364-20372, 1997.
[144] J. A. Hunt, M. Ahmed, and C. A. Fierke, "Metal binding specificity in carbonic anhydrase is influenced by conserved hydrophobic core residues," *Biochemistry,* vol. 38, no. 28, pp. 9054-9062, 1999.
[145] T. Chen, M. Li, and J. Liu, "π–π stacking interaction: a nondestructive and facile means in material engineering for bioapplications," *Crystal Growth & Design,* vol. 18, no. 5, pp. 2765-2783, 2018.
[146] Q. Lu, D. S. Hwang, Y. Liu, and H. Zeng, "Molecular interactions of mussel protective coating protein, mcfp-1, from Mytilus californianus," *Biomaterials,* vol. 33, no. 6, pp. 1903-1911, 2012.
[147] Q. Lu, E. Danner, J. H. Waite, J. N. Israelachvili, H. Zeng, and D. S. Hwang, "Adhesion of mussel foot proteins to different substrate surfaces," *Journal of The Royal Society Interface,* vol. 10, no. 79, p. 20120759, 2013.
[148] A. Torreggiani, J. Domènech, S. Atrian, M. Capdevila, and A. Tinti, "Raman study of in vivo synthesized Zn (II)-metallothionein complexes: Structural insight into metal clusters and protein folding," *Biopolymers,* vol. 89, no. 12, pp. 1114-1124, 2008.
[149] R. Tuma, "Raman spectroscopy of proteins: from peptides to large assemblies," *Journal of Raman Spectroscopy: An International Journal for Original Work in all Aspects of Raman Spectroscopy, Including Higher Order Processes, and also Brillouin and Rayleigh Scattering,* vol. 36, no. 4, pp. 307-319, 2005.
[150] J. Domènech, A. Tinti, M. Capdevila, S. Atrian, and A. Torreggiani, "Structural study of the zinc and cadmium complexes of a type 2 plant (Quercus suber) metallothionein: insights by vibrational spectroscopy," *Biopolymers: Original Research on Biomolecules,* vol. 86, no. 3, pp. 240-248, 2007.

[151] K. Nakamura, S. Era, Y. Ozaki, M. Sogami, T. Hayashi, and M. Murakami, "Conformational changes in seventeen cystine disulfide bridges of bovine serum albumin proved by Raman spectroscopy," *Febs Letters,* vol. 417, no. 3, pp. 375-378, 1997.
[152] J. Domènech, R. Bofill, A. Tinti, A. Torreggiani, S. Atrian, and M. Capdevila, "Comparative insight into the Zn (II)-, Cd (II)-and Cu (I)-binding features of the protozoan Tetrahymena pyriformis MT1 metallothionein," *Biochimica et Biophysica Acta (BBA)-Proteins and Proteomics,* vol. 1784, no. 4, pp. 693-704, 2008.
[153] A. Torreggiani, C. Chatgilialoglu, C. Ferreri, M. Melchiorre, and S. Atrian, "Non-enzymatic modifications in metallothioneins connected to lipid membrane damages: structural and biomimetic studies under reductive radical stress," *Journal of proteomics,* vol. 92, pp. 204-215, 2013.
[154] R. S. Czernuszewicz, J. LeGall, I. Moura, and T. G. Spiro, "Resonance Raman spectra of rubredoxin: new assignments and vibrational coupling mechanism from iron-54/iron-56 isotope shifts and variable-wavelength excitation," *Inorganic chemistry,* vol. 25, no. 5, pp. 696-700, 1986.
[155] B. C. Dave, R. S. Czernuszewicz, B. C. Prickril, and D. M. J. Kurtz, "Resonance Raman spectroscopic evidence for the FeS4 and Fe-O-Fe sites in rubrerythrin from Desulfovibrio vulgaris," *Biochemistry,* vol. 33, no. 12, pp. 3572-3576, 1994.
[156] F. A. Rotsaert, J. D. Pikus, B. G. Fox, J. L. Markley, and J. Sanders-Loehr, "N-isotope effects on the Raman spectra of Fe 2 S 2 ferredoxin and Rieske ferredoxin: evidence for structural rigidity of metal sites," *JBIC Journal of Biological Inorganic Chemistry,* vol. 8, pp. 318-326, 2003.
[157] L. S. Nobre *et al.*, "Escherichia coli RIC is able to donate iron to iron-sulfur clusters," *PLoS One,* vol. 9, no. 4, p. e95222, 2014.
[158] J. B. Broderick *et al.*, "Pyruvate formate-lyase-activating enzyme: strictly anaerobic isolation yields active enzyme containing a [3Fe–4S]+ cluster," *Biochemical and biophysical research communications,* vol. 269, no. 2, pp. 451-456, 2000.
[159] C. Iannuzzi *et al.*, "The role of CyaY in iron sulfur cluster assembly on the E. coli IscU scaffold protein," *PloS one,* vol. 6, no. 7, p. e21992, 2011.
[160] C. M. Silveira *et al.*, "Molecular details on multiple cofactor containing redox metalloproteins revealed by infrared and resonance raman spectroscopies," *Molecules,* vol. 26, no. 16, p. 4852, 2021.
[161] G. Caserta *et al.*, "Unusual structures and unknown roles of FeS clusters in metalloenzymes seen from a resonance Raman spectroscopic perspective," *Coordination Chemistry Reviews,* vol. 452, p. 214287, 2022.
[162] R. S. Czernuszewicz, K. A. Macor, M. K. Johnson, A. Gewirth, and T. G. Spiro, "Vibrational mode structure and symmetry in proteins and analogs containing Fe4S4 clusters: resonance Raman evidence that HiPIP is tetrahedral while ferredoxin undergoes a D2d distortion," *Journal of the American Chemical Society,* vol. 109, no. 23, pp. 7178-7187, 1987.
[163] L. K. Kilpatrick, M. C. Kennedy, H. Beinert, R. S. Czernuszewicz, T. G. Spiro, and D. Qiu, "Cluster structure and H-bonding in native, substrate-bound, and 3Fe forms of aconitase as determined by resonance Raman spectroscopy," *Journal of the American Chemical Society,* vol. 116, no. 9, pp. 4053-4061, 1994.

[164] K. Chandramouli, M.-C. Unciuleac, S. Naik, D. R. Dean, B. H. Huynh, and M. K. Johnson, "Formation and properties of [4Fe-4S] clusters on the IscU scaffold protein," *Biochemistry,* vol. 46, no. 23, pp. 6804-6811, 2007.
[165] B. Zhang *et al.*, "Reversible cycling between cysteine persulfide-ligated [2Fe-2S] and cysteine-ligated [4Fe-4S] clusters in the FNR regulatory protein," *Proceedings of the National Academy of Sciences,* vol. 109, no. 39, pp. 15734-15739, 2012.
[166] J. Liu *et al.*, "Metalloproteins containing cytochrome, iron–sulfur, or copper redox centers," *Chemical reviews,* vol. 114, no. 8, pp. 4366-4469, 2014.
[167] H. Zeng, D. S. Hwang, J. N. Israelachvili, and J. H. Waite, "Strong reversible Fe3+-mediated bridging between dopa-containing protein films in water," *Proceedings of the National Academy of Sciences,* vol. 107, no. 29, pp. 12850-12853, 2010.
[168] Q. Lin *et al.*, "Adhesion mechanisms of the mussel foot proteins Mfp-1 and Mfp-3," *Proceedings of the National Academy of Sciences,* vol. 104, no. 10, pp. 3782-3786, 2007.